ALHAMBRA
K_s-band selected catalogue

Lorena Nieves Seoane

Tesis presentada para optar al título de
Doctora en Física

DIRECTOR DE TESIS
Alberto Fernández Soto

VNIVERSITAT DE VALÈNCIA

Observatori Astronòmic de la Universitat de València
Departament d'Astronomia i Astrofísica
Universitat de València
Valencia
Mayo de 2017

Diseño de la portada: Fernando J. Ballesteros Roselló.

Dr. Alberto Fernández Soto,
Científico titular del CSIC en el Instituto de Física de Cantabria,

CERTIFICA

Que la presente memoria, "ALHAMBRA K_s-band selected catalogue", ha sido realizada bajo su dirección por Doña Lorena Nieves Seoane, y que constituye su Tesis Doctoral para optar al Grado de Doctora en Física.
Y para que quede constancia y tenga los efectos oportunos, firmo el presente documento en Paterna, a 31 de Mayo de 2017.

Firmado: Alberto Fernández Soto

A meus pais,
a meu irmán, a Tere
e a Tono

Agradecimientos

En primer lugar me gustaría dar las gracias a mi director de tesis Alberto Fernández-Soto, que me ha dado la oportunidad de investigar a su lado en "esto de la Astronomía". Solo tengo palabras de agradecimiento hacia este gran investigador y sobretodo gran persona. Alberto me ha acogido en esta tierra haciéndome sentir como en mi propia casa. Los comienzos en otras ciudades lejos de la familia siempre son duros y el mío fue especialmente difícil, pero gracias a Alberto fue mucho más llevadero. Recordaré estos años como una época de crecimiento profesional y personal increíble. Es un gran mentor y una persona excepcional a la que quiero y admiro. Gracias con todo mi corazón.

A mi tutor en la Universidad de Valencia Vicent Martínez muchísimas gracias por todas sus instructivas charlas y anécdotas de las que tanto he aprendido. Agradecerle también sus clases magistrales en el máster que nos mantenían totalmente hipnotizados e hipnotizadas. Gracias por enseñarme la importancia del deber que tenemos los que nos dedicamos a la ciencia a divulgarla en un lenguaje claro y comprensible.

Quiero agradecer especialmente el esfuerzo realizado por las personas que componen el tribunal de evaluación de esta tesis doctoral: Rafael Guzmán, Paolo Saracco, Begoña Ascaso, Patricia Sánchez, Pablo Arnalte y Mauro Stefanon.

No podían faltar en estos agradecimientos tres personas que se han embarcado en todo lo que les he propuesto para este trabajo: Pablo Arnalte Mur, Carlos López Sanjuan y Alberto Molino Benito. Estos "tres mosqueteros" siempre han estado dispuestos a colaborar y ayudar en todo lo que les he pedido. Nunca he recibido un no por respuesta. Pablo, Alberto M. y Carlos me han convencido que todo el trabajo y esfuerzo hecho vale la pena. Trabajar a su lado ha sido

maravilloso y no tengo palabras suficientes para agradecerles todo el tiempo que me han dedicado.

A mis compañeros de ALHAMBRA David Cristóbal Hornillos, Begoña Ascaso, Mauro Stefanon, Luís Alberto Díaz y Alessandro Ederoclite, siempre dispuestos a escuchar y transmitir su experiencia en su campo de investigación para mejorar este trabajo. Muchísimas gracias por vuestros consejos y sugerencias.

A mis directores en las estancias internacionales en Italia y Reino Unido: Luigi Guzzo e Ignacio Ferreras, muchísimas gracias por permitirme investigar en los grupos de investigación que lideráis. Gracias por hacerme partícipe de vuestro trabajo y por todo lo que me habéis enseñado. Especialmente me gustaría agradecer a Ignacio su preocupación y su amabilidad.

A Fernando Ballesteros, autor de la portada de esta tesis doctoral, muchas gracias por enseñarme tanto sobre todo lo que se puede hacer en astronomía. Eres toda una inspiración para cualquier joven investigador o investigadora. Además de ser un gran compañero siempre dispuesto a ayudar eres un gran investigador, un gran divulgador, un gran profesor y sobretodo un gran amigo.

Un agradecimiento muy especial a mis compañeros y amigos del Observatori: Fernando Ballesteros, Julia Suso, Amelia Ortiz, José Carlos Guirado, Juan Fabregat, Sofía Fuentes, Esther Ibáñez, Miquel Gómez, Xusa Moya, Joan Climent, Rebecca Azulay, Vicent Peris, Oscar Brevià, Mónica Pallardó, Leo Gouvelis , Lluís Hurtado y Carlos Peña. Este grupo de gente, junto con Alberto Fernández y Vicent Martínez, son los responsables de que todos y cada uno de los días del año llegase al Observatori con una gran sonrisa dibujada en mi cara. Gracias por el *"Hard Rock Cafe"* y por todo el cariño que me habéis dado. No hay palabras para expresar lo importantes que habéis sido para mi estos años en Valencia. En especial me gustaría agradecer a Amelia Ortíz, Julia Suso y José Carlos Guirado todo el apoyo que me han dado estos año. Muchas gracias.

A los amigos y amigas que he conocido durante estos años y me han acompañado en esta aventura: millones de gracias a Mauro, a mi *cara* Elisa y a su pequeña Aurora que se convirtieron casi sin querer en mi familia y a los que hecho tanto de menos. A Bego por escucharme siempre con una sonrisa optimista. Gracias por tus e-mails y por tu cariño. A Raquel García, a la que conocí una noche de primavera en el antiguo cauce del Turia, tocando la gaita. Gracias por ayudarme tanto, por escucharme, por darme otra visión del mundo. Eres una

persona tan bonita que es imposible no quererte. A Nelo, Laura y la pequeña Marina mi familia en Valencia, mis amigos incondicionales que tanto me han ayudado: gracias por estar siempre a mi lado. A Javier y a Quique gracias por dejar que participe un poquito de vuestra vida. A mis queridos Maggie, Fernan y a las "pequeñas" Rebeca y Lara, gracias por ayudarme siempre, por vuestras sonrisas y por vuestro sentido del humor. Mari Ángeles y a Roberto, gracias por acogerme en vuestra familia cuando más necesitaba a la mía.

A Rebecca gracias por ser mi amiga. Es inevitable emocionarse cada vez que recuerdo todo lo que hemos pasado juntas: paseos en coche, las cenas, los helados en la terraza de la estación de metro de Godella, los paseos por la playa, el viaje a Galicia y a una montaña de más de 4.000 m de altura en plenos Alpes Suizos. Hemos vivido grandes momentos juntas y he aprendido mucho de ti. Gracias por compartir un pedacito de ti conmigo.

Os meus amigos que tanto boto en falta: Alberto, Bieito, María, Ricardo e Suso, tamén coñecidos como os Harmónicos esféricos. Grazas por apoiarme sempre, por seguir na miña vida, aínda que as circunstancias non me permitan veros tanto como eu quixera.

A toda a miña familia, os que están e os que non están, moitas grazas por todo o cariño que me dades. En especial quixera mencionar a miña madriña Helena, ás miñas tías María José e Marisa, ós meus tíos Margarita e Suso: grazas por quererme tanto , por estar conmigo durante toda a miña vida, por coidar de min dende que era pequena e por facerme medrar coma persoa. A miña *avoíña querida da alma* Carmen, gracias por coidar de min e por quererme tanto e porque sei que xunto con meus pais foi a persoa que máis me botou de menos os primeros meses que pasei aquí. A miña avoa María que tanto vou botar en falta. Graciñas por seguires queréndome na distancia. O máis duro para min é todo o tempo que non podo pasar con vós e perderme todos estes anos da vosa vida.

A mi familia política: Rosa y Toni, Ana Leticia y Josep, Rosa Pilar y Paco. Y sobretodo a mis dos pequeños sobrinos Elisa y Diego. Gracias por vuestro apoyo incondicional y por acogerme en vuestra casa como una más. Vosotros y vosotras hacéis que todo el vacío que tengo por tener a mi familia lejos, sea un poco más pequeño. En especial me gustaría dar las gracias a Rosa y a Toni, no tengo palabras para agradecerles todo lo que me han ayudado estos últimos meses de tesis.

A mi hermano Miguel agradecerle todo el apoyo que me ha dado estos años, por comprenderme, por escucharme y por ser el mejor hermano que podría tener. A mi tía Teresa gracias por inculcarme el hábito de la lectura, por despertarme la curiosidad científica, por educarme y por que es la responsable en gran medida de que haya llegado hasta aquí. ¡Tú y tus constantes charlas acerca de que esta vida hay que ser valiente!. Gracias Tere.

Os meus pais Paz e Roberto, mamá e papá, grazas por todo: polo voso sacrificio para que eu puidese seguir adiante, por facer de min *unha persoa de proveito*, por apoiarme en cada unha das miñas loucuras. Porque vos creedes en min máis do que creo eu en min mesma. E tamén porque sei sen ningunha dúbida que vós máis que ninguén padecíchedes coa miña marcha. Grazas papá e mamá.

Finalmente me gustaría darle las gracias a Tono, mi pareja. Él más que nadie ha sufrido con esta tesis, incluso a veces más que yo misma. Me has ayudado tanto que me faltarían páginas para agradecerle todo lo que has hecho por mi estos últimos meses. Gracias por consolarme cada vez que me desesperaba, por animarme cuando estaba triste, por cuidarme tanto cuando estaba enferma. Me has acompañado en cada palabra que he escrito, celebrando conmigo cualquier pequeño avance. Gracias Tono por estar a mi lado, por apoyarme en todo momento y por tu infinita paciencia. Parafraseando a un tal *Sagan*, en el espacio infinito y en la inmensidad del tiempo, es mi alegría compartir este planeta y esta época contigo.

Contents

List of Figures

List of Tables

"A tiny blue dot set in a sunbeam. There it is.
That's where we live. Thats home.
We humans are one species and is our world.
It is our responsibility to cherish it"
- Carl Sagan

Chapter 1

Introduction.

1.1 Historical context.

The formation and evolution of galaxies in the visible universe is one of the main topics in astronomy research. We have to look back to the year 1908 to find the bases of modern cosmology. That year, Henrietta Swan Leavitt published her manuscript "*1777 Variables in the Magellanic Cloud*" (Leavitt 1908). In this work she presented her studies of Cepheid stars and postulated the period-luminosity relationship, also known as "Leavitt law". At the time of the discovery, Henrietta didn't realise how important this relation would be for the estimation of the size of the Universe. The Period-Luminosity law would become the "Rosetta Stone" for the astronomers to unscramble distances in the Universe.

In the year 1920 a "Great Debate" took place in the Baird Auditorium of the Smithsonian Museum of Natural History, between two of the most influential astronomers of their time: Harlow Shapley and Heber Curtis. The main issue under discussion was "*The Scale of Universe*". Curtis argued that the objects identified as spiral nebulae were separate galaxies like the Milky Way. Shapley, however, contended that the size of the Milky Way was underestimated, and all the Universe was contained in our Galaxy, even those spiral nebulae were just nearby gas clouds within the Milky Way. This event was the first time in history that astronomers postulated such a leap in the universe size scale. In the year 1925, Edwin Hubble solved the discussion in his paper "*A spiral nebula as a stellar*

system: Messier 33" (Hubble 1926). Thanks to the observations and conclusions provided by Leavitt, together with the works on the calibration of Cepheid stars by Hertzsprung and Shapley, Hubble estimated the distance to the Cepheid stars inside Messier 33, and proved that Shapley was wrong in his conclusions.

Back in 1917 the observational astronomer Vesto M. Slipher had concluded a remarkable result in his spectroscopic measurements: the spectra of most of the *"nebulae"* showed redshifted lines, with the fainter ones having a stronger redshift. He interpreted this as a sign that the nebulae were moving away from our Galaxy. Based on Slipher's measurements and his own Hubble established the dependence between radial velocities and distances in the Universe (Hubble 1929), using his own distance estimations and the radial velocity data provided by Slipher (1917) and Humason (1929) (See Figure 1.1). Today this relation is known as "Hubble's Law":

$$cz = H_0 D \tag{1.1.1}$$

where c is the velocity of light, z is the redshift observed in each galaxy, D is the distance to it, and H_0 is a proportionality coefficient also known as Hubble's term.

In his manuscript Hubble named the constant "The K term" and according with his own calculation he assigned to it the value[1] $K = 500$ km s^{-1} Mpc^{-1}. In the following years of the publication of this result, many astronomers realised that Hubble's conclusions were not strictly correct: The redshift-distance relation works for nearby galaxies (i.e. with small values of redshift), but not for distant galaxies. The redshift-distance was based on the Fizeau-Doppler formula $V = cz$, but this identity is only an approximation.

Previously to Hubble's experimental conclusion, Robertson (Ph.D. 1928) had derived a theoretical linear law using the radial velocity and the distance:

$$V = H_0 D \tag{1.1.2}$$

which was also known as the *velocity-distance* law. This relation is a cornerstone of modern cosmology and is absolutely valid considering a homogeneous and isotropic universe.

[1]The Hubble term H changes with time, so we denote H_0 when we refer to the present value of this term. $H_0 = (67.8 \pm 0.9)$ km s^{-1} Mpc^{-1} (Planck Collaboration et al. 2016)

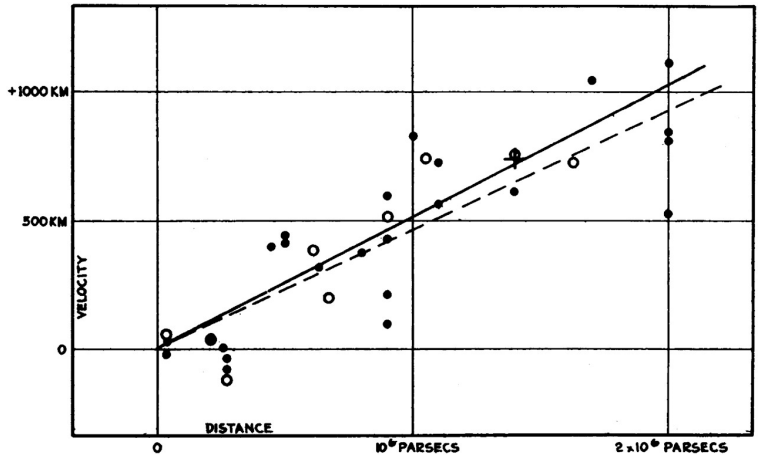

Figure 1.1: Hubble's original plot of the relation between the distance in parsecs (X axis) and redshift estimated as cz in km s^{-1}. In the original plot the units are accidentally written in km.

Behind the conclusions of Robertson and Hubble lies the most important implication of the experimental results obtained from Slipher's redshift measurements: the expansion of the Universe. The astronomers at that time interpreted that extragalactic systems were receding from our Galaxy and the further they were, the faster they moved away. Today we know that these other galaxies, as we call them now, are not moving away from us, but that it is the Universe who is expanding, and trails the galaxies within itself.

At the same period, in concordance with observational results, astronomers and cosmologists developed different theoretical models whose common goals were to explain the geometry of space-time. In 1915, Albert Einstein presented his Theory of General Relativity (Einstein 1915), which changed the traditional view of our surrounding universe. According to Albert Einstein's Theory the space-time structure of the Universe is determined by the matter distribution within it. Two years later Albert Einstein himself (Einstein 1917) and his contemporary Willem de Sitter proposed two different families of models of the Universe: The "steady-state" Einstein's cosmological model, which consider a temporally infinite but spatially finite universe, and the "static" cosmological model proposed by de Sitter.

In the late 1920s and 1930s the theoretical developments by Friedmann (1922), Lemaître (1927), Robertson (1933) and other cosmologists allowed them to change the previous vision of a static universe to several classes of homogeneous, isotropic, expanding universe models. They discovered a totally new interpretation of extragalactic redshift which was based on the expanding space paradigm.

As a consequence of the result that the Universe is expanding as Hubble's observations proved, the astronomer George Lemaître suggested (Lemaître 1931) that if the Universe is in expansion, at a given moment in the past, all the mass that today conforms the Universe should have been concentrated in a single point. It was Fred Hoyle in 1949 who named it as *"this big bang idea"*, trying to discredit Lemaître theory. George Gamow developed the idea of the Big Bang theory introducing *Big Bang nucleosynthesis* (Gamow 1946), and together with Ralph Alpher and Robert Herman in Alpher & Herman (1948) predicted the existence of the cosmic microwave background (CMB). In 1964 the astronomers Arno Penzias and Robert Wilson accidentally discovered the CMB with the Holmdel Horn Antenna (Penzias & Wilson 1965), a discovery which is considered a landmark test of the Big Bang Theory.

1.2 The cosmological model

The standard model of cosmology we apply today arises from the application of theoretical models together with the observations that were developed in the first third of the 20^{th} century. Modern Cosmology is based on the *Cosmological Principle* hypothesis, which states that on large scales (roughly > 100 Mpc) the Universe is homogeneous (there are no preferred locations) and isotropic (there are no preferred directions).

We can derive the geometry of the Universe using a function that defines the distance between two events in space-time, usually known as *metric*. In order to define this function we consider the location of two events as (t, r, θ, ϕ) and $(t + dt, r + dr, \theta + d\theta, \phi + d\phi)$ in an homogeneous and isotropic space[2]. Under this assumption, the metric which is obtained is known as *Minkowski metric* and is

[2] r, θ, ϕ are spherical coordinates.

expressed as

$$ds^2 = -c^2dt^2 + dr^2 + r^2d\theta^2 + r^2sin^2\theta d\phi^2 \tag{1.2.3}$$

where c is the speed of light in a vacuum. As we mentioned in Section 1.1, between the 1920s and 1930s the physicists Alexander Friedmann, Georges Lemaître, Howard Roberson, and Arthur Walker estimated independently the metric of the Universe using the Minkowski metric, but they included that the structure of space-time depends upon the mass distribution in the Universe, as was established in Einstein's General Relativity. This metric, generally known today as the Friedmann-Lemaître-Robertson-Walker (FLRW) metric, is generally written as

$$ds^2 = c^2dt^2 - a(t)^2\Big[\frac{dr^2}{1-Kr^2} + r^2(d\theta^2 + sin^2\theta d\phi^2)\Big]. \tag{1.2.4}$$

The space-time variables are called *co-moving coordinates*. The term $a(t)$ is the *scale factor* which describes how the scale of the Universe changes with time under the assumption of the Cosmological Principle. By convention, $a(t_0) = 1$ at the present time.

K is a dimensionless constant called *curvature parameter*. The value of this parameter can be $K = 0$, if we consider a flat universe; $K = 1$ if we consider positive spatial curvature in the Universe; $K = -1$ if we consider negative spatial curvature in Universe. Available evidence indicates that our Universe is nearly flat.

Using the FLRW metric we can describe the geometry of the Universe and it is possible to calculate the proper distance between two points. We define here the "geodesic" as the path of minimum distance between two events in space-time. The proper distance, denoted by d_p, is the length of the spatial geodesic between two points and with a given fixed value of $a(t)$. In the case of a purely spatial geodesic (i.e. (t, θ, ϕ)=constant) the FLRW metric expression for a flat universe ($K = 0$) is $ds = a(t)dr$. If we integrate the equation we obtain the expression of the proper distance:

$$d_p(t) = a(t)\int_0^r dr = a(t)r. \tag{1.2.5}$$

The first time derivative of the proper distance d_p gives us a relation between the proper distance and the proper velocity. We denote as $\dot{a}$ the time derivative of a, and we obtain

$$\dot{d_p} = \dot{a}(t)r = \frac{\dot{a}(t)}{a(t)}d_p. \tag{1.2.6}$$

In Section 1.1 we described how Hubble obtained the velocity-distance law (Equation 1.1.2) from observational results, and comparing this equation with equation 1.2.6, we can express the Hubble constant at the present time as:

$$H_0 = \left(\frac{\dot{a}}{a}\right)_{t=0}. \tag{1.2.7}$$

1.2.1 Measurement of distances in the Universe

Measuring directly the current proper distance to a distant galaxy is physically impossible. It would take a measuring tape that could be instantaneously deployed from one point to another, or to stop the expansion of the Universe. Thus astronomers had to seek how to estimate distances in the Universe using other measurable properties.

One of this measurable features is the *redshift*, which is defined as the fractional increase between the wavelength of a photon emitted by a distant source (λ_e) and its wavelength when it is observed (λ_0), due to the expansion of the Universe:

$$z = \left(\frac{\lambda_0 - \lambda_e}{\lambda_e}\right). \tag{1.2.8}$$

We can establish a relationship between the scale factor $a(t)$ and the redshift z. Considering that the scale factor has a value $a(t_e)$ in the instant t_e when the light was emitted by the galaxy, and taking into account the expansion and its present value $a(t_0)$, we obtain

$$\frac{\lambda_0}{\lambda_e} = \frac{a(t_0)}{a(t_e)} = \frac{1}{a(t)}. \tag{1.2.9}$$

Inserting this in Equation 1.2.8 we obtain the relation between the redshift z and the scale factor a:

$$z = \frac{\lambda_0}{\lambda_e} - 1 = \frac{1}{a(t)} - 1. \tag{1.2.10}$$

Other measurable properties of extragalactic objects include the intrinsic luminosity L and the flux f. If we consider that the Universe is static and verifies a Euclidean geometry, the flux f measured by an observer located at a distance r from a source is determined by a inverse square law relationship, which we can express as

$$f = \left(\frac{L}{4\pi r^2}\right). \tag{1.2.11}$$

From this consideration and under the assumption of $d_L = r^3$, we can define a function of redshift called *Luminosity distance* such that it fulfils:

$$d_L \equiv \Big(\frac{L}{4\pi f}\Big)^{\frac{1}{2}}. \tag{1.2.12}$$

Our goal now is to establish a relation between a non-measurable distance (the proper distance d_p) and a measurable distance given by the Luminosity distance function d_L, using the redshift z. From equation 1.2.5 it is possible to set the proper distance as a function of redshift, using equation 1.2.10

$$d_p(t) = a(t)r = \Big(\frac{1}{1+z}\Big)r. \tag{1.2.13}$$

From Equation 1.2.5 we can express the co-moving coordinate r as $r = (1+z)d_p$ which, combined with Equation 1.2.11, yields

$$f = \Big(\frac{L}{4\pi(1+z)^2 d_p^2}\Big). \tag{1.2.14}$$

As a result of comparing Equations 1.2.12 and 1.2.14, and under the assumptions previously described, the relation between the luminosity distance and the current proper distance that we were seeking is

$$d_L = d_p(t=0)(1+z). \tag{1.2.15}$$

1.2.2 The Friedmann equation

According to Einstein's General Relativity the space-time geometry of the Universe is determined by the distribution of matter and energy within it. For describing the gravitation interactions, Einstein sets his "Field Equation" as

$$R_{\mu\nu} - \frac{1}{2}Rg_{\mu\nu} + \Lambda g_{\mu\nu} = \frac{8\pi G}{c^2}T_{\mu\nu} \tag{1.2.16}$$

where the term $R_{\mu\nu}$ is Ricci's curvature tensor and describes the local curvature of space-time. The term $g_{\mu\nu}$ represents the metric as a 4×4 tensor. The parameter R is Ricci's curvature scalar, Λ is the cosmological constant introduced by Einstein to obtain a stationary universe, G is Newton's gravitational constant and c the

[3] The justification for this equality is not described here.

speed of light in a vacuum. Finally, the term $T_{\mu\nu}$ is the energy-momentum tensor of the matter content in the Universe.

If we assume that space-time is an ideal fluid with a given mass density ρ and pressure P and consider that, under the conditions of the Cosmological Principle, the metric term in Einstein's Field Equation ($g_{\mu\nu}$) is given by the FLRW metric, then the expression for the Field Equation can be rewritten as

$$H_0^2 \equiv \left(\frac{\dot{a}}{a}\right)^2 = \frac{8\pi G}{3}\rho - \frac{Kc^2}{a^2} + \frac{\Lambda c^2}{3} \tag{1.2.17}$$

where ρ is the energy density (usually denoted by ε) expressed in units of c^2. This is also known as the Friedmann equation, and is one of the most relevant tools in cosmology to determine the quantities of the different components of which the Universe is made up.

Considering a flat universe ($K = 0$) and taking the vacuum energy density term $\Lambda = 0$, we define the *critical density* today as:

$$\rho_c = \frac{3}{8\pi G}H_0^2. \tag{1.2.18}$$

Its value today is 5 atoms of hydrogen (H) per cubic meter. We define this parameter because cosmologists often measure the density of the different components of the Universe in terms of the critical density.

The Friedmann equation can not describe by itself the evolution in time of the scale factor $a(t)$, since we have another parameter $\rho(t)$ that varies with time. We need another equation that involves both terms, and we find it in the First Law of Thermodynamics, under the assumption that the content of the Universe behaves as a perfect fluid in adiabatic expansion. Under this hypothesis, the First Law can be expressed as

$$\dot{\rho} + \frac{3\dot{a}}{a}(\rho + P) = 0. \tag{1.2.19}$$

Equation 1.2.19 is the *fluid equation*. A very common way to use this equation is through the *acceleration equation*. If we isolate $\dot{a}$ in the Friedmann equation (1.2.17), apply the first time derivative and divide it by $2a\dot{a}$ we obtain

$$\frac{\ddot{a}}{a} = \frac{8\pi G}{3}\Big(\frac{1}{2}\frac{a}{\dot{a}}\dot{\rho} + \frac{3\Lambda c^2}{3}\Big). \tag{1.2.20}$$

Substituting the value of $\dot{\rho}$ obtained in equation 1.2.19, we obtain the acceleration equation in its most recurrent expression

$$\frac{\ddot{a}}{a} = -\frac{4\pi G}{3}\big(\rho + 3P\big) + \frac{3\Lambda c^2}{3} \tag{1.2.21}$$

where P is the pressure as a function of time $P = P(t)$. This equation describes how quickly or slowly our Universe is expanding.

We have two independent equations: the Friedmann equation (1.2.17) and the fluid equation (1.2.19). But we have introduced a new magnitude $P(t)$, so it is necessary to include another independent equation in order to describe the expansion of the Universe in terms of the quantities $a(t)$, $\rho(t)$ and $P(t)$.

According to the Cosmological Principle and considering that the content of the Universe behaves like a perfect fluid, we can describe the *equation of state* for each component of the Universe as

$$P_i = w_i \rho_i c^2 \tag{1.2.22}$$

where the sub-index i represent each of the components making up our Universe and w_i is a dimensionless parameter with different values for each component. Considering that the equation of state parameter w_i is constant, if we isolate the pressure in the fluid equation 1.2.19 and substitute it in the equation of state (1.2.22) we can rearrange it as

$$\rho_i = \rho_{i,0} a^{-3(1+w_i)}. \tag{1.2.23}$$

From the relation between the redshift z and the scalar factor a (equation 1.2.10), we can express the density in terms of the redshift and the density for each component today $\rho_{i,0}$:

$$\rho_i = \rho_{i,0}(1+z)^{3(1+w_i)}. \tag{1.2.24}$$

According with our observations of the Universe we distinguish three components and their corresponding value for the parameter w_i:

- **The non-relativistic matter component** (m), that includes baryonic matter (ordinary matter) and dark matter. For this component $w_m = 0$ and the density equation 1.2.24 becomes $\rho_m = \rho_{m,0} a^{-3}$.

- **The radiation component** (r), that includes photons or other massless particles. Here $w_r = \frac{1}{3}$ and the density equation 1.2.24 for this component is $\rho_r = \rho_{r,0} a^{-4}$.

- **The vacuum energy component** (Λ), also called dark energy component. It has $w_\Lambda = -1$ and a density equation 1.2.24 that becomes $\rho_\Lambda = \rho_{\Lambda,0}$. The Λ component—if we accept this condition—is constant in the expansion of Universe.

Assuming those are the components of our Universe we can express the Friedmann equation in terms of the density equation as

$$H(t)^2 = \left(\frac{\dot{a}}{a}\right)^2 = \frac{8\pi G}{3}\left[\rho_{m,0}\left(\frac{a_0}{a}\right)^3 + \rho_{r,0}\left(\frac{a_0}{a}\right)^4 + \rho_\Lambda\right] - \frac{Kc^2}{a^2}. \tag{1.2.25}$$

Densities in cosmology are often expressed as a function of the critical density (equation 1.2.18) as *density parameters*. These parameters give the ratio of the density for each cosmological component to the critical density ρ_c:

$$\Omega_i \equiv \frac{\rho_{i,0}}{\rho_c}. \tag{1.2.26}$$

For each component, we can calculate the value of the density parameter today using:

$$\Omega_m(t) \equiv \frac{\rho_{m,0}}{\rho_c}, \qquad \Omega_r(t) \equiv \frac{\rho_{r,0}}{\rho_c}. \tag{1.2.27}$$

We can also parametrise the cosmological constant Λ and the curvature K in terms of a similar density parameter as

$$\Omega_\Lambda \equiv \frac{\rho_\Lambda}{\rho_c} = \frac{\Lambda c^2}{3H_0^2}, \qquad \Omega_K \equiv \frac{Kc^2}{a^2 H_0^2}. \tag{1.2.28}$$

Using the relationship between the critical density ρ_c and the Hubble constant H_0 in equation 1.2.25 we can rewrite the Friedmann equation for the present time ($a_0 = 1$) as

$$1 = \frac{8\pi G}{3H_0^2}(\rho_{m,0} + \rho_{r,0} + \rho_\Lambda) - \frac{Kc^2}{H_0^2 a^2} \tag{1.2.29}$$

and thus

$$1 = \left(\frac{\rho_{m,0}}{\rho_c} + \frac{\rho_{r,0}}{\rho_c} + \frac{\rho_{\Lambda,0}}{\rho_c}\right) - \frac{Kc^2}{H_0^2 a^2}. \tag{1.2.30}$$

It then follows from the density parameter definition:

$$\frac{Kc^2}{H_0^2 a^2} = \Omega_{m,0} + \Omega_{r,0} + \Omega_{\Lambda,0} - 1 \tag{1.2.31}$$

and finally, using the curvature density parameter (equation 1.2.28):

$$\Omega_K = \Omega_{m,0} + \Omega_{r,0} + \Omega_{\Lambda,0} - 1 \tag{1.2.32}$$

from where we deduce that the curvature of space-time is determined by the total density of the Universe.

In the literature it is common to use redshift as a surrogate for time. We can find the Friedmann equation written as function of the redshift as

$$H(z) = \left(\frac{\dot{a}}{a}\right)(z) = H_0 E(z) \tag{1.2.33}$$

where

$$E(z) = [\Omega_{m,0}(1+z)^3 + \Omega_{r,0}(1+z)^4 + \Omega_{\Lambda,0} + \Omega_K(1+z)^2]^{1/2}. \tag{1.2.34}$$

Using these equations we can fully determine the geometry of the Universe described with the FLRW metric once that we know the values of the parameters H_0, Ω_Λ, $\Omega_{m,0}$,Ω_K and $\Omega_{r,0}$, taking into account that at the present time we consider $a = a_0 = 1$, and we can calculate their values at any given redshift.

1.2.3 Observed properties of the universe

Over the last decades, determining the present-time values of the cosmological parameters has been one of the hottest topics in Cosmology. The cosmological parameters can be deduced indirectly by observing the Universe, especially since cosmologists understand the physics behind the observable quantities. In order to provide an accurate value of the cosmological parameters, the final results are estimated combining data from at least four different sets of observations:

- Standard candles. The measurement of standard candles provides a estimation of the redshift-distance relation. As is mentioned in Section 1.1, Hubble used the Cepheid stars as a standard candle to obtain his results about the expansion of the Universe. But the Cepheid stars have limitations due to their low intrinsic luminosity and the absorption of light in the interstellar/intergalactic medium. Cosmologists use Type Ia supernovae (SNe Ia) as a standard candle insomuch as they are extraordinarily luminous (i.e. they can be observed at larger distances) and their spectra and light curves

are exceptionally uniform (i.e. they can be standardised). These events occur in binary star systems in which a white dwarf is accreting mass for a nearby companion. When the accreting component mass excedes the 1.44 $M_{\odot}$ threshold (i.e. the Chandrasekhar limit) its core collapses and causes a thermonuclear explosion, releasing a huge amount of energy to space. Observations of how the luminosity of these events changed with redshift can be used to measure the expansion history of the Universe. Observations from two different groups (Riess et al. 1998; Perlmutter et al. 1999) showed that the Universe is not only in expansion but it is expanding faster since $\sim$ 5 billion years ago. According to this it became necessary to introduce *dark energy* as an exotic component with negative pressure, responsible of the acceleration of the Universe.

- Observation of Large Scale Structures in the Universe. The rapid development of photodetectors in the last 50 years has provided a large enough amount of data for mapping the Universe in 3D. These maps have yielded an amount of information that allows for he analysis of large structures in the Universe. One of the most relevant results is the detection of Baryonic Acoustic Oscillations (BAOs) (Anderson et al. 2014; Eisenstein et al. 2005; Cole et al. 2005). Acoustic oscillations are fluctuations produced and imprinted in the primordial plasma, measured at very large scales in the structure of the baryonic matter power spectrum. The measurement of the wave amplitude and highest peak provides a useful data set that can help settle the nature of dark energy and also results useful for the determination of the consistence of the results obtained in the Cosmic Microwave Background. Other relevant results from the observation of the Large Scale Structure come from the analysis of the growth of the primordial over-dense regions due to the gravitational effects of the *dark matter*.

- Cosmic Microwave Background (CMB). Since Penzias & Wilson (1965) accidentally measured the CMB and Dicke and his collaborators (Dicke et al. 1965) correctly interpreted its nature, cosmologists have devoted their efforts to estimate from it the values of the different cosmological parameters. Over the last 25 years space missions like the Cosmic Background Explorer (COBE) (Smoot et al. 1992), Wilkinson Microwave Anisotropy Probe

(WMAP) (Bennett et al. 2003), and the most recent Planck Mission (Planck Collaboration et al. 2016) were designed to provide increasingly rich datasets to obtain more accurate values of the cosmological parameters. According to the observations, the CMB has a nearly thermal black body radiation and was emitted during the period called *recombination* (378,000 years after the Big Bang). Moreover, the CMB radiation is isotropic, as expected from the Cosmological principle. In addition, the Temperature fluctuation map (see Figure 1.2) shows a close agreement to isotropy at the largest scales, but has the right amount of inhomogeneities in the small scales to account for the gravitational growth of the structures we see today.

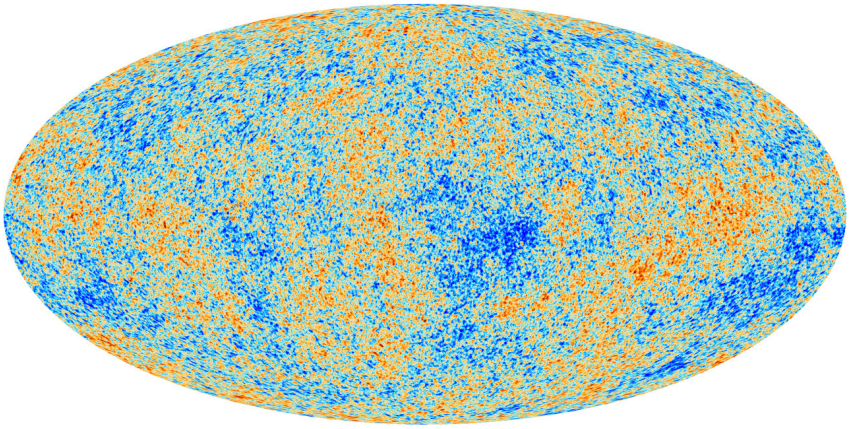

Figure 1.2: Temperature anisotropies of the CMB observed by Planck Collaboration et al. (2016). It shows temperature fluctuations ranged from -300 μK (blue regions) to the 300 μK (red regions) that correspond to regions of slightly different densities. Credit: ESA

- Big Bang Nucleosynthesis (BBN). Under the assumptions of the standard BBN (Gamow 1946), it is possible to predict the abundances of light ele-

ments in the Universe from the conditions of density and temperature at the earliest epochs and their evolution. The BBN model estimates that 75 % in mass of the primordial baryonic matter was ^{1}H, 25 % was Helium-4 (^{4}He), a small fraction (0.01%) was Deuterium (^{2}H) and $\sim 10^{-12}$% was lithium-7 (^{7}Li). Other, heavier elements were formed via stellar nucleosynthesis. The latest measurements of the abundance of light elements carried out by the Planck Collaboration et al. (2016) present a good agreement with the predicted values for ^{1}H and for (^{4}He) (See Figure 1.3), but the abundance of Lithium-7 (^{7}Li) present an evident discrepancy. In the literature it is possible to find several possible solutions for "the Lithium problem". Fields (2012) suggest that the nature of this mismatch relies in systematic errors in the observed abundances, or in the uncertainties in the stellar astrophysics[4], or in a major misunderstanding in our model and the need to consider possible new physics.

According to the combination of those sets of observations and the latter results obtained by the Planck Collaboration et al. (2016), in the present work we have adopted the following values for the cosmological parameters: $H_0 = 67.3$ km s^{-1} Mpc^{-1}, $\Omega_K \sim 0,\ \Omega_{\rm M} = 0.28,\ \Omega_\Lambda = 0.72$.

The mathematical structure described above, together with all the observations described and the parametrisation of the implied physical quantities, make up the so-called Λ-CDM model. This is the most widely used and accepted cosmological model, and provides a reasonable description of the properties observed in the Universe, including the effects due to dark energy and Cold Dark Matter. All the results from the latest observations are in good agreement with this Λ-CDM model.

1.3 Galaxy evolution

A galaxy is a *"gravitationally bound collection of stars whose properties cannot be explained by a combination of baryons and Newton's laws of gravity"* (Willman &

[4]The measurement of absorption lines in primitive low-metallicity stars (Population II) provides a measurement of the abundances of Lithium-7 (^{7}Li).

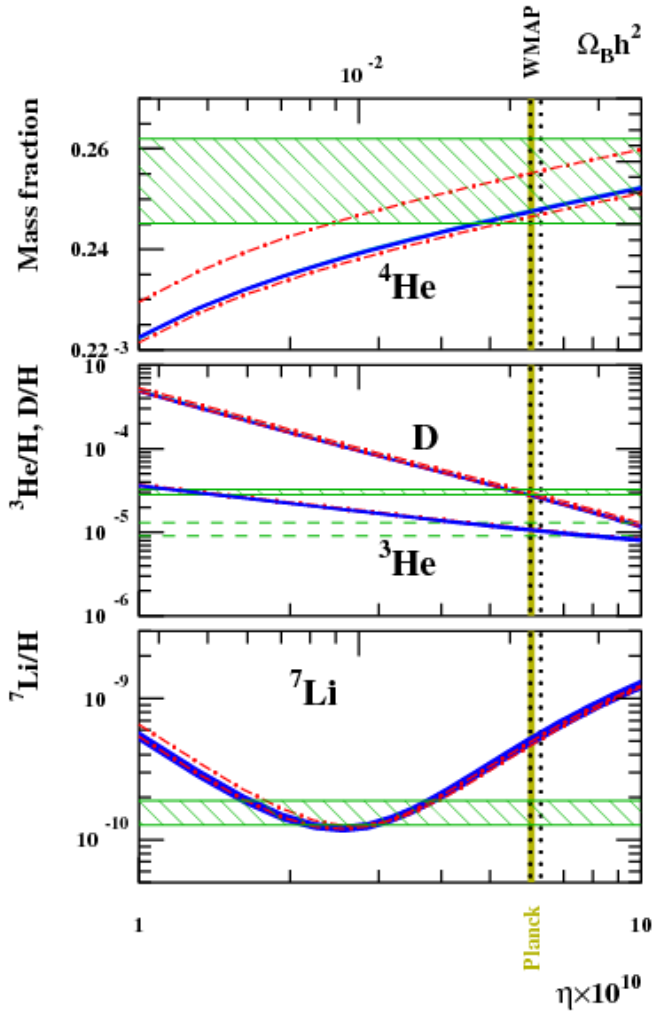

Figure 1.3: Abundances of lightest elements predicted and results of the WMAP and Planck measurements(Coc et al. 2013). Blue lines represent the abundances of ^{4}He, ^{2}H, ^{3}He and ^{7}Li. Green boxes corresponds to the adopted observational abundances. Finally vertical lines ares the baryonic densities for WMAP (dot, black) and Planck (yellow). The plot shows a good agreement with the data for ^{4}He and ^{2}H. However there are a discrepancy for the ^{7}Li abundances.

Strader 2012). How did galaxies form and how did they evolve, how can they be classified taking into account their aspect or their physical properties, and how can we understand the structures that they form in the Universe are all essential parts of astronomy and cosmology today.

The morphological classification of galaxies is based on their external appearance. This classification is simple, insomuch that today we still use the sequence described by Edwin Hubble in the 1930s. Hubble's scheme (Figure 1.4) encompasses most of the galaxy morphologies in the local Universe. Most galaxies can be broadly classified in two types: *Elliptical* and *Spiral* galaxies. Hubble believed (mistakenly) that his classification reflected a chronological evolutionary trend, through which the elliptical types flattened and evolved into spirals. Because of this erroneous idea, both classes are often referred to as *early-type* in the case of ellipticals and *late-type* in the case of spirals. A third class of galaxies (*Irregular*) was added to encompass those galaxies whose aspect does not match any of the spiral or elliptical types. Irregular galaxies are in fact the most common ones in the high-redshift Universe.

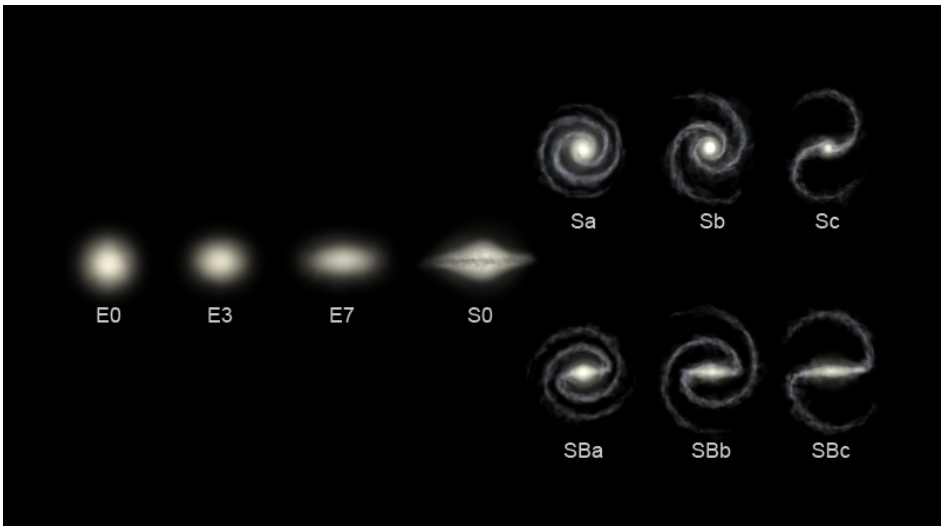

Figure 1.4: Hubble's morphological classification of galaxies. Because of the shape this scheme is usually referred to as *Hubble's tuning fork*.

Differences between galaxies are not only due to their shape. It is possible

to establish a bimodal classification taking into account some common physical properties of galaxies, that in fact overlaps with the two main galaxy types as described by Hubble: elliptical and spiral.

- Elliptical galaxies are characterised by their ellipsoidal isophotes. They do not rotate in a synchronised manner, with each star orbiting the common center along its own plane, and with large dispersion velocities directly related to the total galaxy mass. They are mostly devoid of gas and dust, which implies a low star formation rate. Old, red, low-mass and metal-rich stars dominate in these galaxies, which renders them brighter on the red passbands compared to the blue passbands (Madau & Dickinson 2014). They are generally more massive, and seem to prefer denser regions of the Universe (Kauffmann et al. 2004), particularly in extreme cases the centre of galaxy clusters.

- Spiral galaxies have a more complex morphology. Typically they are formed by a rotationally supported disk which may include spiral arms, and an elliptical-like bulge which occupies the centre of the galaxy. Often the area surrounding the bulge includes a bar. In the central regions the stellar population is older than in the arms. The richness of dust and gas and the dynamics of the spiral arms (Lin & Shu 1964) promote an active star formation and, with it, the presence of bright, massive ,short-lived stars, that render the arm structure visible. Unlike in the case of elliptical galaxies the stellar populations of spiral galaxies are younger, so their light is dominated by the short-lived massive, blue, young population. These galaxies are often located at the low-density regions in the Universe, and their numbers decrease significantly towards the central regions of galaxy clusters.

According to the passband in which each kind of galaxies are brighter, and as expected based on their stellar populations, spirals are often called *blue* galaxies, and ellipticals are called *red* galaxies. This bimodal classification is clearly present in colour-colour diagrams (Figure 1.5), where it is possible to distinguish two well separated regions: the red galaxies region and the blue galaxies region (Strateva et al. 2001). The same effect can be seen in colour-magnitude plots, where a narrow strip is occupied by red, elliptical galaxies (the red sequence), and a broader region is occupied by blue, spiral galaxies (the blue cloud).

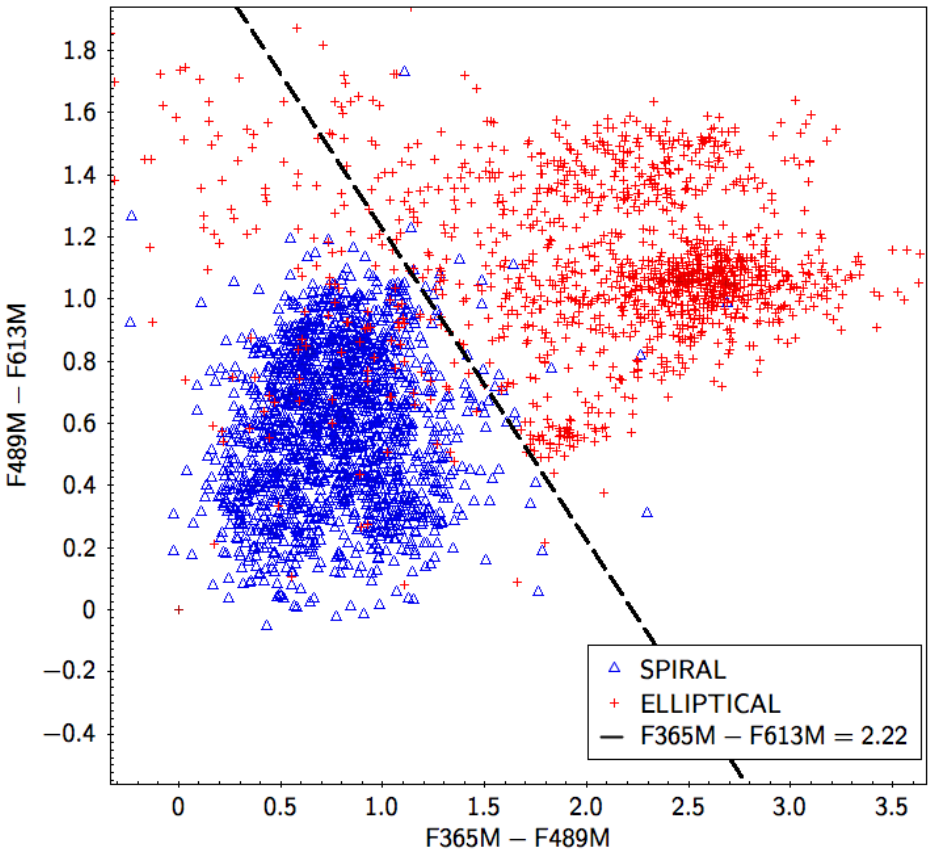

Figure 1.5: Example of a colour-colour diagram showing a clear separation of elliptical and spiral galaxies.

To better understand galaxy formation and evolution it is necessary to assess the physical processes in the observable universe at different epochs. Due to the limit imposed by the speed of light, photons from distant objects that we receive today give us information about how those objects were when the light set out from them. It is possible to obtain a frame of the universe at each redshift and therefore, at different times. This time-line of the Universe allows us to study how the properties of the galaxies have evolved in time until the present day. This analysis requires observations of large samples of galaxies covering a wide range of redshifts over a significant area of the sky, that is, it requires large *Astronomical*

Surveys.

1.4 Astronomical surveys

Astronomical surveys are one of the key elements in the advancement of our knowledge of celestial objects. From the earliest time astronomers have charted stars and observed their basic properties, namely their projected positions in the celestial sphere and their apparent brightnesses. Direct observation of astronomical objects only provides information about their projected position in the sky. In order to describe how those astronomical objects are distributed in the three-dimensional universe, astronomers have to map them adding a third coordinate to provide an accurate measurement of their distances from Earth. In the particular case of cosmology, and as we described earlier, the observed spectral redshift is used as a proxy for the distance, with all the caveats that need to be taken into account for such substitution.

The task increased exponentially in complexity over the last century with the successive arrivals of large and more sophisticated telescopes, the photographic plate, and electronic detectors. It became even more complex in the last decades, linked to the increasing capabilities of computers and digital detectors for amassing data. These technological advances enabled the process of huge quantities of astronomical data in a reasonable time, and led astronomers to the era of large astronomical surveys. They allow the pursuit of a wide range of scientific objectives, like i) mapping large numbers of objects in order to measure the structure and appearance of the observable universe, or ii) obtaining statistically significant samples at different redshifts able to characterise astrophysical processes and describe the large-scale structure of the baryonic matter and the manner in which it evolves (Djorgovski et al. 2013).

In our time some of the most successful astronomical surveys have aimed at covering ever larger fractions of the phase space that includes area in the sky, photometric depth and spectral information. For the moment being (and in any foreseeable future) no project will cover satisfactorily and simultaneously all of those dimensions. For example, the Sloan Digital Sky Survey (SDSS, York et al. 2000) and the Two Degree Field Galaxy Redshift Survey (2dFGRS, Colless et al. 2001) have obtained spectral information for $\sim 10^5$–10^6 objects each, by observing

large areas (approximately 1/4 of the whole sky) down to a relatively shallow limit (apparent magnitudes $AB \approx 19$). Their photometric counterparts cover areas in the sky of the same size, but reach ten times deeper, out to a typical magnitude $AB \approx 21$–22. At the other end of survey space, deep surveys like the Hubble Deep Fields (Ferguson et al. 2000) cover tiny areas of the sky (of the order of 10^{-3} square degrees or even less) but do include spectroscopy out to $AB \approx 25$–26 and multi-band photometry out to $AB \approx 28$ and even deeper.

A different "axis" defining cosmic surveys is that of spectral completeness. In the most basic end, early surveys like the Palomar Observatory Sky Survey (POSS, Minkowski & Abell 1963; Reid et al. 1991), included only photometric information in two different bands (*i.e.* one colour) for each object. In the opposite end, spectroscopic surveys include a full spectrum for each target, with all that implies in terms of information content regarding measurements of redshift, star formation history, mass, metallicity, etc. Since the advent of the Hubble Deep Fields (Ferguson et al. 2000) and other surveys at the end of the last century it has become commonplace to obtain images through multiple filters both in the optical and the near infrared in order to measure at least some spectral properties of the targets, which should allow for basic estimation of some of the physical quantities that would otherwise need a full spectral analysis. The use of photometric redshift techniques has grown and become standard based on this kind of studies (Fernández-Soto et al. 1999; Benítez 2000; Bolzonella et al. 2000). Over the last few years some surveys have been explicitly designed having these techniques in mind ("Classifying Objects by Medium-Band Observations in 17 Filters" (COMBO-17), Wolf et al. 2003; "the Advanced Large Homogeneous Area Medium-Band Redshift Astronomical" (ALHAMBRA), Moles et al. 2008) and have proved the case for even larger surveys with multiple medium-band filter images (J-PAS, Benitez et al. 2014).

1.5 Galaxy clustering

As we have mentioned in Section 1.2.2, one of the main goals of cosmology is that of measuring and understanding the Large Scale Structure (LSS) of the Universe. In the last decades it has become widely accepted that the LSS that we observe in the Universe today can be explained as the evolution of the initial fluctuations in

the matter density on the early Universe, that have grown through gravitational instabilities. These fluctuations in the matter-energy primordial fluid can be observed as temperature deviations in the CMB (See Figure 1.2).

The observable properties of the LSS extracted from sky surveys allow us to study the matter distribution and its evolution in cosmic time until the formation of the structures that we observe today. These properties enclose information about cosmological parameters such as the matter density or the abundance and properties of dark energy, and encompass significant information about the physics of galaxy formation and evolution. Large scale galaxy samples like the Two Degree Field Galaxy Redshift Survey (2dFGRS, Colless et al. 2001) or the Sloan Digital Sky Survey (SDSS, York et al. 2000) have yielded much information about the spatial distribution of galaxies over significant cosmological volumes, and they have provided maps of the galaxy distribution (see Figure 1.6) unveiling rich structures such as the filaments that form the largest systems of galaxies, or void regions of space containing few, if any, galaxies. One of the earliest discoveries in this field was precisely that these structures are not uniformly distributed in the Universe, and nowadays it is possible to build models that accurately reproduce the shapes that we observe in the LSS.

In order to measure the galaxy distribution and the cosmic structures observed in galaxy surveys it is common to use the galaxy two-point correlation function (denoted by $\xi(r)$, Peebles 1980; Martínez & Saar 2002), or its Fourier transform, the power spectrum[5]. Both functions are statistical tools that allow us to quantify the observed trend that galaxies have to form groups or patterns, by measuring the clustering excess compared with a Poisson distribution (Peebles 1980). Assuming an homogeneous and isotropic point process, the two-point correlation function $\xi(r)$ can be defined in terms of the probability dP of finding a galaxy in a volume element dV at a given distance r from another galaxy,

$$dP = n[1 + \xi(r)]dV, \tag{1.5.35}$$

where n represents the mean number density of the galaxy sample (Peebles 1980).

[5]The power spectrum and the two-point correlation function contain equivalent information, but the first one is often used preferentially to describe the initial fluctuations in the energy density.

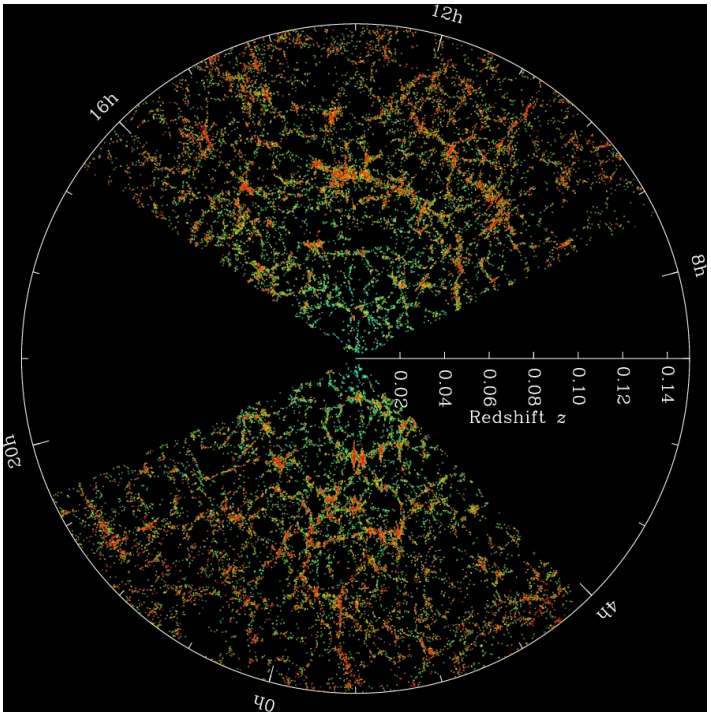

Figure 1.6: Large scale structure of the SDSS main galaxy redshift sample. The center of the figure is the relative position of the Earth. Each point in the plot represents a galaxy, and their colours are according to the age of their stars. The reddest galaxies are more strongly clustered and also show an older star population. Credit: M. Blanton and the Sloan Digital Sky Survey.

If there is an excess of clustering, the value is $\xi(r) > 0$, if there is a defect of clustering, the value is $\xi(r) < 0$ and in the case of a homogeneous distribution we get $\xi(r) = 0$. The two-point correlation function has dominated the study of the large scale galaxy distribution, and it has been recurrently estimated from almost every catalogue of galaxy positions, either using projected sky coordinates or in redshift space. In the following we briefly describe the estimation of the two-point correlation function from a redshift sky survey.

1.5.1 Measurement of the two-point correlation function

Besides the formal definition of the two-point correlation function, the common algorithm used to measure $\xi(r)$ for a particular galaxy sample consists in finding an efficient way to obtain the probability that at given distance r we have an excess or deficit of number counts of galaxies with respect to an homogeneous Poisson distribution. To achieve this estimate one must build an equivalent Poisson point catalogue in the same volume as the data and compare the number of pairs in the data sample having separation r with the number of pairs in the Poisson catalogue separated by the same r. The main problem in this kind of analysis is related to the underestimation of the counts in those regions which are close to the volume boundaries. In the literature we can find several formulae that provide appropriate estimators of the correlation function for any given data set, and take into account those border effects.

The first widely used estimator is from Davis & Peebles (1983):

$$\widehat{\xi}_{DP}(r) = \frac{N_R}{N_D}\frac{DD(r)}{DR(r)} - 1 \tag{1.5.36}$$

where N_R is the number of points in the Poisson catalogue, N_D is the number of galaxies in the real data catalogue, $DD(r)$ is the count of pairs of galaxies at a given r in the data catalogue, and $DR(r)$ is the count of cross pairs at a given r between the data and the random catalogues.

Other estimators proposed at a later stage include the one proposed by Hamilton (1993):

$$\widehat{\xi}_{HM}(r) = \frac{DD(r)\cdot RR(r)}{[DR(r)]^2} - 1, \tag{1.5.37}$$

and the estimator by Landy & Szalay (1993):

$$\widehat{\xi}_{LS}(r) = 1 + \left(\frac{N_R}{N_D}\right)^2 \frac{DD(r)}{RR(r)} - 2\frac{N_R}{N_D}\frac{DR(r)}{RR(r)}. \tag{1.5.38}$$

where $RR(r)$ is the count of pairs of galaxies at a given r in the random catalogue.

Several works like Pons-Bordería et al. (1999), Kerscher (1999) or Labatie et al. (2010) conclude that at short distances the results of these estimators are very similar but, however, at large scales the cosmic bias and variance induced by boundary effects is lower using the estimators proposed by Hamilton (1993) and Landy & Szalay (1993). In this thesis the correlation function estimated in Chapter 3 for the K_s-band catalogue was carried out using the estimator by Landy & Szalay (1993) .

1.5.2 Redshift distortions

Large spectroscopic of photo-spectroscopic galaxy surveys provide three-dimensional positions for each galaxy. The position can be split in two components considering the line of sight: a component perpendicular to the line of sight, given by the angular position of the object σ, and another component along the line of sight direction π, directly related to the redshift z. The line-of-sight component is in fact a combination of the cosmological redshift due to the expansion of the Universe and the peculiar velocity of the object.

Peculiar velocities introduce distortions in redshift space, interfering on the measurement of the correlation function $\xi(r)$. To recover the real space correlations it is useful to split the correlation function ξ as a function of its two different components $\xi(\sigma, \pi)$. Figure 1.7 shows the redshift space distortion for the 2dF-GRS (Peacock et al. 2001). Contours represent constant ξ values, with the yellow areas corresponding to large values of ξ and the green areas corresponding to the low values. It is obvious that at small scales the contours are elongated in the direction of the π component, while at large scales the contours are flattened. The former effect corresponds to the observation of "fingers of God" which are due to small-scale peculiar velocities in virialised over-densities. The large-scale flattening, on the other hand, is due to coherent infall of matter into large structures (Sargent & Turner 1977). In modern cosmology these features can be used to constrain the value of the Ω_m parameter by modelling of the redshift space

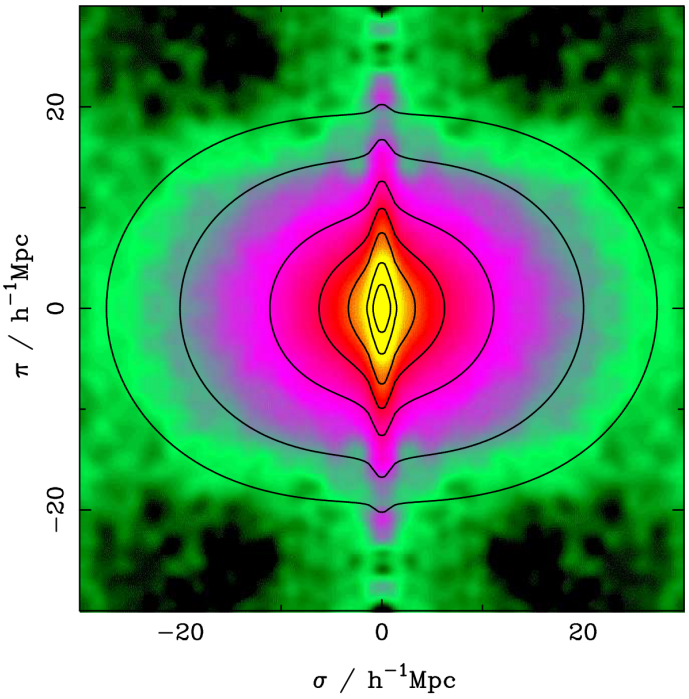

Figure 1.7: The two-dimensional redshift-space correlation function from the 2dFGRS survey $\xi(\sigma, \pi)$. The figure shows the effects of the redshift distortions. Contours lines represents constant ξ values, with yellow colours corresponding to large values of ξ and green areas corresponding to low values of ξ. Figure from Peacock et al. (2001).

distortions (Kaiser 1987; Hamilton 1998).

Measurements of the two-point correlation function using redshift surveys are strongly affected by "redshift distortions" due to the peculiar velocities and to the coherent infall of galaxies, but the effect is limited only to the longitudinal direction. That implies the loss of the isotropy that we have assumed to calculate the $\xi(r)$ using any of the estimators. Another issue is the photometric redshifts themselves: as we use a photometric catalogue, uncertainties in the photometric redshift determination will extend to uncertainties in the measured positions. To avoid these issues it is posible to recover the two point correlation function $\xi(r)$ using its projection along the perpendicular line of sight direction σ (Davis &

Peebles 1983).

We will describe in Chapter 3 the method followed in Arnalte-Mur et al. (2014), to recover the real-space correlation function from photometric redshift survey data with non-negligible redshift errors, and we will also show and discuss the results obtained for the clustering calculations performed with the ALHAMBRA K_s-band catalogue.

1.6 The luminosity function

The galaxies we find in the Universe encompass a large range of luminosities, from the dwarf galaxies with $L \sim 10^9 L_\odot$ and below (where $L_\odot$ is the solar luminosity) to ultraluminous galaxies with values as high as $L \sim 10^{12} L_\odot$ and beyond. This quantity, particularly if measured along several spectral bands, allows us to derive some basic physical information about each galaxy such as the type of stellar population that dominates or the dust content within.

In a survey we have a large sample of galaxies which gives us the opportunity to study the luminosity as a statistical property of the galaxy ensemble, helping us to better understand the processes related to galaxy evolution. The Luminosity function (LF) $\phi(L)$ is a powerful statistical tool which is defined such that the number density of galaxies in a given volume dV of the Universe with luminosities in the range $[L, L + dL]$ is given by $\phi(L)\, dL\, dV$ (Murdin 2001)[6].

The luminosity is measured in some particular photometric passband. Historically, the earliest works found in literature used the B-band or the R-band, because in those bands the spectral sensitivity of photographic plates was most efficient. Many present projects still use the same bands to allow a direct comparison of the results obtained. But with the improvement of NIR detectors used in wide-fields CCD cameras, it is now possible to find results obtained for the K_s-band luminosity function (Arnouts et al. 2005a; Cirasuolo et al. 2010; Mortlock et al. 2017). Studying the evolution of the LF in the NIR results particularly useful because observations of the galaxy emission in the rest-frame in this spectrum

[6]The LF is given indistinctly in terms of galaxy luminosity, as $\phi(L)dL$; or in terms of galaxy absolute magnitude, as $\phi(M)dM$.

range are less affected by dust absorption and recent star formation episodes, being an excellent stellar mass trace (see Lilly & Longair 1984; Dunlop et al. 1989; Cowie et al. 1996).

In the particular case of a photometric redshift survey, to calculate the LF we need to recover the number density of galaxies as a function of two quantities that are estimated from the photometric information: the absolute magnitude in the photometric band of choice (M_i) and the photometric redshift z, to yield $\Phi(M_i, z)$. In Chapter 2 we will describe the process of obtaining the photometric redshift by a SED-fitting process. From the apparent magnitudes included in the survey photometric catalogues, the absolute magnitude M_i in a given rest-frame passband i at given redshift z is calculated as

$$M_i = m_i - DM(z, \Omega_0, \Omega_\Lambda, h) - K_i(z) \tag{1.6.39}$$

where the term $DM(z, \Omega_0, \Omega_\lambda, h)$ is the distance modulus as determined from the redshift assuming a particular cosmology, and the K_i term is the K-correction term for the transformation from the observed-frame measurement passband to the rest-frame i-band (Oke & Sandage 1968).

Traditionally the LF is fitted to a Schechter function (Schechter 1976),

$$\phi(L)dL = \phi^\star \left(\frac{L}{L^\star}\right)^\alpha \exp\left(\frac{-L}{L^\star}\right)\frac{dL}{L^\star} \tag{1.6.40}$$

where $\phi^\star$ is a normalisation parameter, $L^\star$ is a characteristic luminosity and α defines the faint-galaxy end of the LF. The Schechter function will differ for i) each morphological type of galaxies (quiescent/star forming or red-type/blue-type) (Madgwick et al. 2002), ii) the enviroment properties (high density regions/low density regions) (Driver & De Propris 2003) iii) and the redshift range (Lilly et al. 1996).

In Chapter 4 we will determine the galaxy LF using a multi-filter K_s-selected cross-match catalogue that includes the ALHAMBRA Survey filters (Aparicio Villegas et al. 2010) plus the four bands at 3.6, 4.5, 5.8, and 8.0 μm from the *Spitzer Space Telescope* Infra-Red Array Camera (IRAC, Fazio et al. 2004), in the ALHAMBRA Survey area which has been covered with deep IRAC observations. There we will include a description of the process we followed to obtain the K_s-band LF $\Phi(M_{K_s}, z)$ using the full Bayesian probability distribution functions (PDFs) of the photometric redshift, based on the works already developed for the

ALHAMBRA optical catalogue, and the study of the LF obtained for the different galaxy types. We will compare our work with other similar, relevant works and discuss our results.

1.7 Motivation and aims of this thesis

Early-type galaxies dominate the bright end of the luminosity function at low and moderate redshifts (Lin et al. 1997), in particular they include the most massive galaxies that inhabit the largest overdensities in those epochs. They represent the most massive and evolved objects in the second half of the life of the Universe, and their study is basic to understand how star formation proceeded and its interrelations with many other cosmic processes: black hole formation and evolution, galaxy clustering and the formation of large-scale structures, galactic interactions and mergers, and the AGN phenomenon (Heckman & Best 2014, and references therein).

Due to their intrinsically red colours, early-type galaxies are selected against in magnitude-limited surveys selected at optical wavelengths at all those redshifts where the Balmer break and associated absorption features around $\lambda = 4000$ Å are redshifted into the detection band and rewards of it. Over the last years the development of several surveys that detect objects in near infrared (NIR) bands (see Table 1.1) has significantly helped in the analysis of the evolution of early-type galaxies at moderate and high redshift, e.g. the Newfirm Medium Band Survey (NMBS, Whitaker et al. 2011), UKIDSS-Ultra Deep Survey (Lawrence et al. 2007), WIRCam Deep Survey (WIRCDS, Bielby et al. 2012), and Ultra VISTA (McCracken et al. 2012; Muzzin et al. 2013) (see Figure 1.8).

In the particular case of the ALHAMBRA survey, where detection is performed over a synthetic image that emulates the Hubble Space Telescope F814W filter, this selection effect that creates a bias against red galaxies begins to be noticeable at $z \approx 0.8$, and is dominant at $z \geq 1.1$, as has already been noticed by Arnalte-Mur et al. (2014). A typical early-type spectral energy distribution at $z \approx 0.8$ has a colour $(I - K_s) \approx 1.8$, whereas the same galaxy at $z \approx 1.4$ shows $(I - K_s) \approx 3.1$, and reaches $(I - K_s) \geq 4.5$ at redshift $z = 2$. This means that, even if the optical detection image is, as is the case in ALHAMBRA, deeper than the corresponding K_s band, at least some of the incompleteness produced by the selection effects

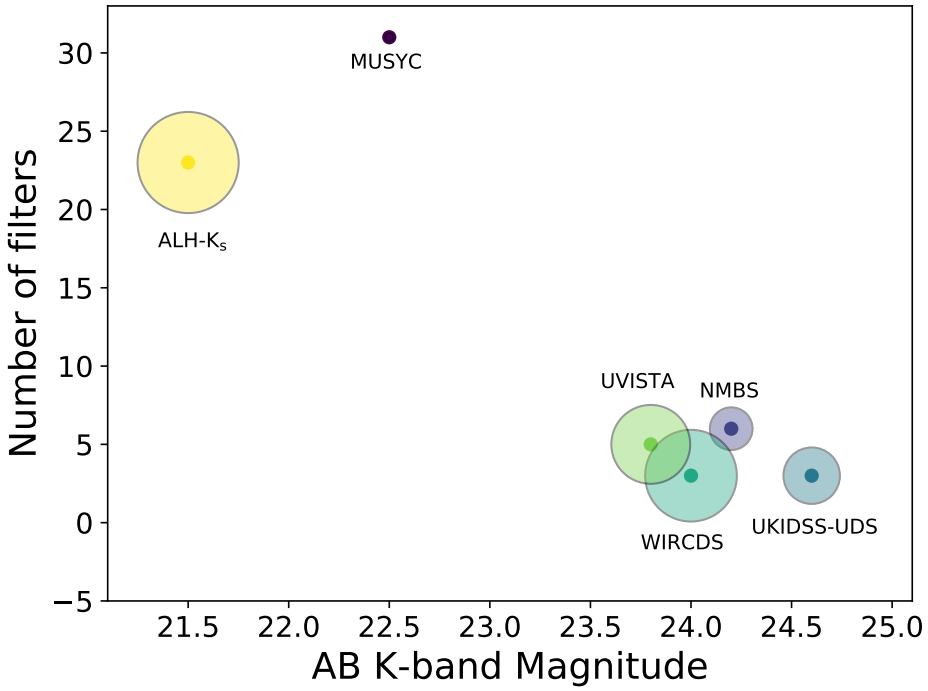

Figure 1.8: Comparison of the area (shadow regions), the number of photometric bands and the magnitude deepness of the ALHAMBRA K_s-band catalogue with other K-band selected surveys.

Survey	Area	AB Magnitude (5σ Limit)
MUSYC	0.015 deg^2	$K_s \approx 22.5$
NMBS	0.44 deg^2	$K \approx 24.2$
UKIDSS-UDS	0.77 deg^2	$K \approx 24.6$
WIRCDS	2.03 deg^2	$K_s \approx 24.0$
UVISTA	1.50 deg^2	$K_s \approx 23.8$
ALHAMBRA K_s-band	2.47 deg^2	$K_s \approx 21.5$

Table 1.1: Comparison with other photometric K-band selected surveys.

can be avoided by using the K_s band to provide the detection image.

In this Thesis we present the K_s-band selected catalogue of galaxies in the ALHAMBRA survey that has been compiled in order to partially overcome the selection bias described above. With this catalogue we will be able to extend some of the works that have already been performed with the ALHAMBRA data to higher redshifts $z > 1$. We perform a cross-match catalogue with the public data from the *Spitzer Space Telescope* Infra-Red Array Camera (IRAC, Fazio et al. 2004), in order to extend the photometry further into infrared range and to observe a much wider rest-frame spectral window.

The organization of the Thesis is as follows:

- In Chapter 2 we introduce the ALHAMBRA survey and describe in detail the construction of the K_s-band catalogue.
- In Chapter 3 we present the catalogue and its properties. We also include a brief discussion of some immediate applications of the catalogue, with particular attention to how its use will be important in order to complete (either in terms of redshift or in terms of galaxy types) some of the analyses that have already been published based on the optical ALHAMBRA catalogue. We describe in this chapter the method followed in Arnalte-Mur et al. (2014) to recover the real-space correlation function, apply it to our sample, and discuss the results obtained for the ALHAMBRA K_s-band catalogue.
- In Chapter 4 we present the results obtained from the analysis of the cross-match data between the K_s band catalogue and Spitzer/IRAC data, where available. We present the K_s-band luminosity function for the overlapping area and discuss the results by comparing with other similar works.
- We close in Chapter 5 with our Thesis conclusions and a brief description of the future work.

1.8 Acknowledgements

This Thesis is based on observations collected at the Centro Astronómico Hispano-Alemán de Calar Alto (Almería), jointly operated by the Max-Planck-Institut für Astronomie (MPIA) and the Instituto de Astrofísica de Andalucía (CSIC). This

study makes use of data from AEGIS, a multiwavelength sky survey conducted with the Chandra, GALEX, Hubble, Keck, CFHT, MMT, Subaru, Palomar, Spitzer, VLA, and other telescopes and supported in part by the NSF, NASA, and the STFC. In Chapter 3 of this Thesis have made used of data products from observations made with ESO Telescopes at the La Silla Paranal Observatories under ESO programme ID 179.A-2005 and on data products produced by TERAPIX and the Cambridge Astronomy survey Unit on behalf of the UltraVISTA consortium.This research has made extensive use of NASA's Astrophysics Data System. In Chapter 4 of this Thesis we have made use of the NASA/ IPAC Infrared Science Archive, which is operated by the Jet Propulsion Laboratory, California Institute of Technology, under contract with the National Aeronautics and Space Administration. In Chapter 4 of this Thesis we have made use of the HST-COSMOS database, operated at CeSAM/LAM, Marseille, France.

This work was mainly supported by the Spanish Ministry for Economy and Competitiveness and FEDER funds through grants AYA2010-22111-C03-02, AYA2013-48623-C2-2, and AYA2016-81065-C2-2; and by the Generalitat Valenciana through projects PROMETEO/2009/064 and PROMETEOII/2014/060. The author enjoyed a FPI Doctoral grant under project BES-2011-050936.

Chapter 2

The dataset

To understand the evolution of the Universe and its content, a representative picture would be required at each cosmic time. As we introduced in Section 1.4, astronomical surveys represent a fundamental basis to the study of astrophysical processes and of the distribution and evolution of the baryonic matter in the observable Universe. Surveys contain large samples of different sources at different times, suitable to perform many detailed analyses in order to tackle the main goals of astronomy. A particularly efficient design in this sense is that of multi-band photometric surveys. Surveys of this kind gather and measure the flux from a given object in different wave-bands and compare the distribution of flux that is observed with the one expected from a series of template spectra in the same wave-bands. It is thereby possible to determine the best-fit redshift and the best-fit spectral type of each galaxy (or whichever other property is searched for in different kinds of targets). As we have explained in Chapter 1, the great advantage of this method lies in the speed at which photometric surveys can obtain data for multiple sources in comparison with their spectroscopic survey counterparts.

The filter system adopted by the photometric survey will determine the resolution of the spectral energy distributions (SEDs) of the objects observed, so both the width and the effective wavelength of each filter needs to be taken in account. Photometric surveys usually obtain photometry using broad-band filters like those in the Sloan or the Johnson system. The new generation of photometric surveys use purpose-designed medium or narrow band filters in order to obtain

a better resolution in the recovering of the SED of the detected sources and to determine the redshifts with more precision.

Historically, during the first half of the 20^{th} century, imaging was obtained in optical wavelengths. But in the second half of the last century, with the progress in the digital detectors and optical technology, astronomers began to explore the sky in every wavelength range, from the ultra-violet to radio. The opening of these new windows in the spectral domain led to the discovery of new objects and to a better characterization of already discovered sources. In the year 1988 the astronomers Richard Elston and George and Marcia Rieke published the results of their research about a new galaxy population that had remained unseen until then (Elston et al. 1988). These objects were bright in the K-band and they were at the same time hardly detected (if at all) in the optical bands, because of their very red colours (for example, and depending on the chosen threshold, as much as $R - K > 5$). It was the rapid development of more sensitive and larger format NIR detectors that led astronomers to use K-band images to observe large samples of galaxies, and to the discovery of this kind of objects. Deeper NIR Surveys confirmed that this spectral range has important advantages for the selection and analysis of evolved galaxies, particularly over the redshift $z \gtrsim 1$, and also in the study of the reddening of star-forming galaxies because the effects due to the dust extinction render such objects more luminous in the NIR bands (Daddi et al. 2002).

In this context, we present in this chapter the Advanced, Large, Homogeneous Area, Medium-Band Redshift Astronomical (ALHAMBRA) Survey[1]. The ALHAMBRA Survey design makes it possible to select objects characterised by their red colours by using the K_s band as a detection image. The construction of such a new ALHAMBRA catalogue, based on the use of the K_s band image as reference, is the main objective of this Thesis.

In this chapter we introduce the imaging data and the previously published F814W-based ALHAMBRA galaxy catalogue, which will be used as anchor and comparison for our work in the (wide) sample where both catalogues overlap. We describe in detail the process leading to the construction of the K_s-band catalogue,

[1] `http://www.alhambrasurvey.com`

including image detection, photometry in the reference K_s band and in the rest of the ALHAMBRA filters, angular selection mask, calculation of the completeness functions, star-galaxy separation, and photometric redshift estimation. We have tried to keep the process used to generate the K_s-band catalogue as close as possible to the one that was performed by Molino et al. (2014) over the I_{814} images both to improve our ability to compare the results and also to keep some degree of consistency between them. In this chapter all magnitudes are given in the AB system (Oke & Gunn 1983).

Part of the content of this chapter has been published in Nieves-Seoane et al. (2017).

2.1 The ALHAMBRA survey.

The Advanced, Large, Homogeneous Area, Medium-Band Redshift Astronomical (ALHAMBRA) Survey has used a purpose-built set of twenty 310-Å wide, top-hat, contiguous and non-overlapping filters that cover the whole visible range from ∼3500Å to ∼9700Å, plus the standard near-infrared $JHK_{\rm S}$ filters (Figure 2.1, Aparicio Villegas et al. 2010) to map eight separate fields in the Northern hemisphere sky (Figure 2.2), down to magnitude $I_{814} \approx 25$. The survey is fully described in Moles et al. (2008), and the final catalogue can be found in Molino et al. (2014), hereafter M14. The regions observed were selected because of their low interstellar extinction and for being outside the galactic plane. The main reason for these selection criteria is to avoid contamination from galactic objects. Five of the eight observed fields correspond to well-known survey areas: they overlap, respectively, with the DEEP2 (Simard et al. 2002), COSMOS (Scoville et al. 2007), HDF-N (Williams et al. 1996), EGS (Davis et al. 2007) and ELAIS-N1 (Rowan-Robinson et al. 2004) fields.

The main driver behind the ALHAMBRA Survey was to create a relatively large, deep, and homogeneous catalogue of galaxies with multi-band photometry and high-quality photometric redshifts, that could be used to analyse the processes of galaxy evolution over approximately 50% of the history of the Universe. The observations were carried out with the 3.5 m telescope of the Centro Astronómico

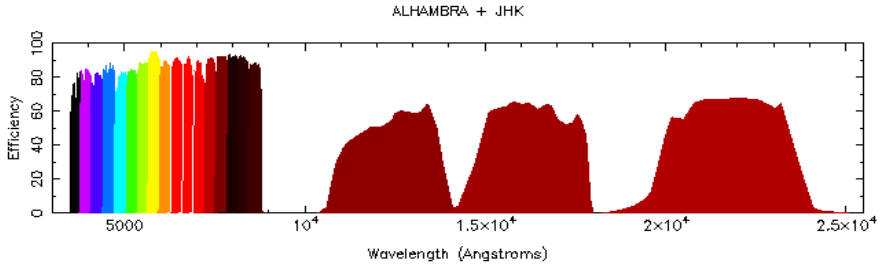

Figure 2.1: The ALHAMBRA 20 optical equal-width filters, covering from ∼3500Å to ∼9700Å plus the three standard near-infrared JHK_S filters.

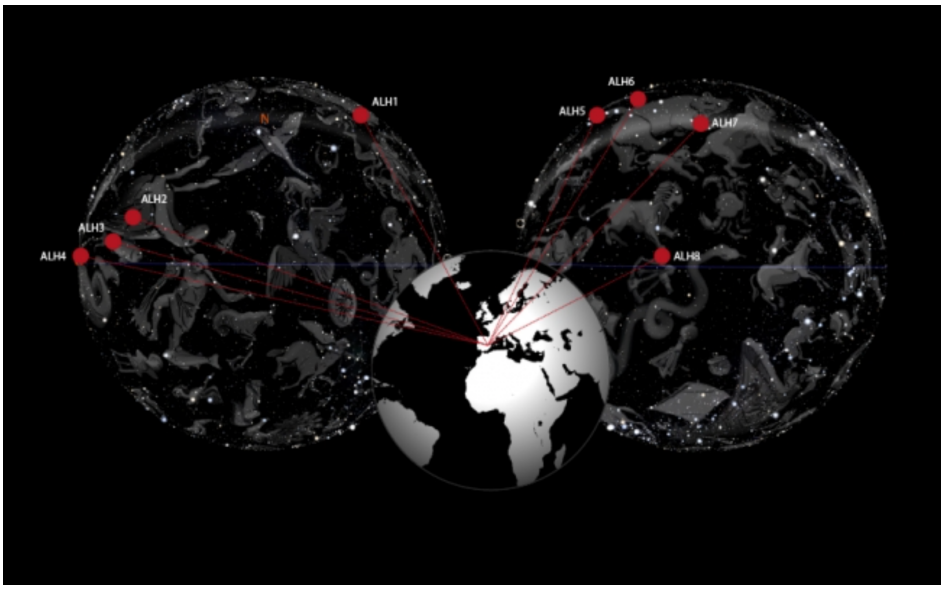

Figure 2.2: Distribution of the 8 ALHAMBRA fields projected over the celestial sphere (http://alhambrasurvey.com/survey-details.php).

Hispano-Alemán (CAHA[2]) in Calar Alto, Almería (Spain), where two different cameras were used: the Large Area Imager for Calar Alto (LAICA[3]) in the optical and OMEGA2000[4] in the NIR. The images were collected between the years 2005 and 2010 and a grand total of $\sim$ 700 hours of on-target observing time was compiled, for a total effective survey area of $\sim$ 2.8 square degrees. The final catalogue presented in M14 includes $\sim 438,000$ galaxies with $\langle z \rangle = 0.86$ and rms photometric redshift accuracy $\delta z/(1+z) = 0.014$.

In order to produce a sample that could be comparable to other surveys, a synthetic detection image was created for every field using the medium-band ALHAMBRA images. This image corresponds very accurately to the one that would be obtained using the HST filter F814W, and we will refer to it over this work as I_{814} for simplicity, even though it does not exactly correspond to the usual Johnson I band. This synthetic image was used for object detection, thus producing object lists and photometric catalogues that are magnitude-limited in the I_{814} band. These catalogues were carefully compared to the ones obtained by Ilbert et al. (2009) in the COSMOS field, proving the validity of the approach.

The original catalogue as presented in M14 has already been exploited to produce a series of basic results for the main scientific aims that led its development: study of high-redshift galaxies (Viironen et al. 2015; Troncoso Iribarren et al. 2016), selection of AGNs and quasars (Matute et al. 2012, 2013), clustering analyses (Arnalte-Mur et al. 2014; Ascaso et al. 2015; Hurtado-Gil et al. 2016), galaxy morphology (Pović et al. 2013), and analyses of the luminosity function of galaxies (López-Sanjuan et al. 2017). The work presented in this Thesis aims at building on some of those previous analyses and to extend them to higher redshift and to different populations.

2.1.1 ALHAMBRA K_s-band images

In order to add information in the NIR range of the spectral energy distributions, the three broad-band standard JHK_s filters were included in the survey. Having these three filters in the infrared range helps in breaking the well-known degener-

[2] `http://www.caha.es`
[3] `http://www.caha.es/CAHA/Instruments/LAICA`
[4] `http://www.caha.es/CAHA/Instruments/O2000`

acy between the 4000 Å break at low redshift and the Lyman break in more distant galaxies. Furthermore the extra information provided significantly increases the scientific value of the data, particularly for elliptical galaxies, strongly reddened AGN, or moderate-redshift starburst galaxies.

The NIR images also provide a set of sources that are not included in the ALHAMBRA main catalogue because of their very red colours, thus in this work we present a new K_s-band selected catalogue. From the very early phases of the ALHAMBRA NIR data reduction (Cristóbal-Hornillos et al. 2009) we noticed that this subset of our data was interesting by itself. Visual inspection and comparison of the K_s-band data with the images in the visible range showed that the former, although obviously shallower than the average of the latter, contained a sizeable sample of objects whose red $(I_{814} - K_s)$ colours made them more noticeable in the NIR images.

Figure 2.3 shows a theoretical colour-magnitude diagram designed to show the expected reach of the regular ALHAMBRA catalogue and that of a K_s-band selected one, in order to offer the reader a visual intuition of the main objective of this work. There is an obvious gain for intrinsically red objects when the near-infrared images are taken as reference (vertical dotted line) compared to a I_{814}-selected sample (diagonal line), particularly in the case of luminous red objects at redshift $z > 1$.

The conditions under which the NIR observations of the different ALHAMBRA fields and pointings were observed were varying, which leads to a clear and significant non-uniformity in the magnitude detection limits for each of them. The median limit[5] of the K_s-band images is magnitude K_s=21.5, with 68% of the images having a 5σ limiting magnitude value between 21.1 and 21.7, as seen in Figure 2.4.

[5]Magnitude limits quoted here are nominal 5σ limits measured in circular, 3-arcsec diameter apertures.

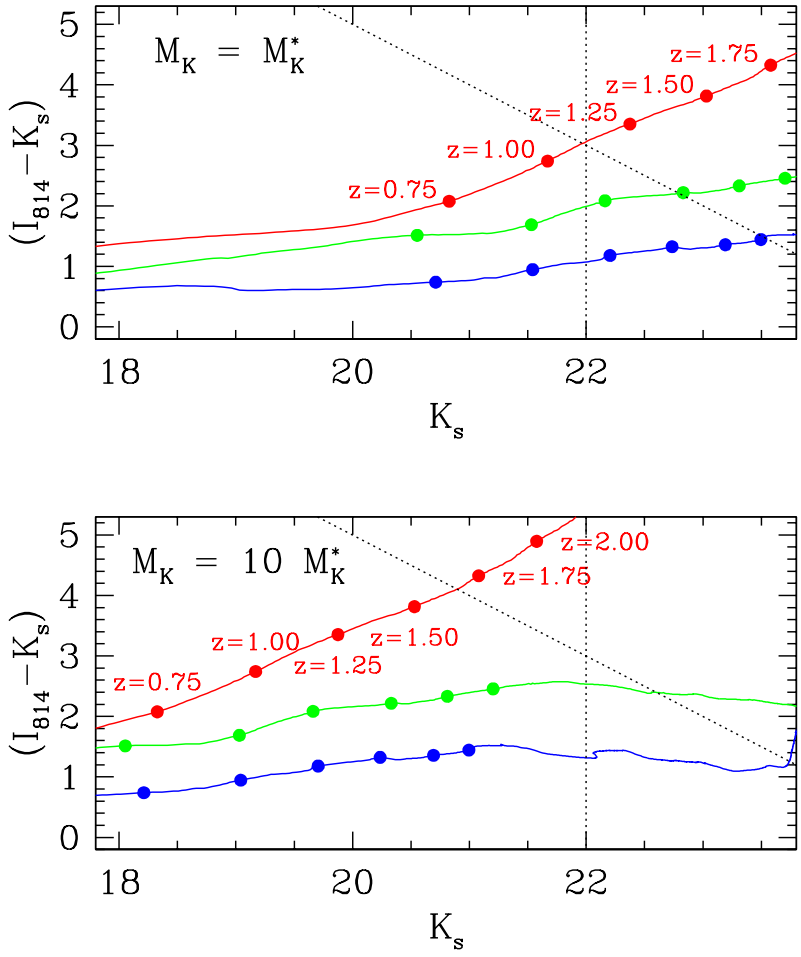

Figure 2.3: Redshift tracks of different M_K^* (top) and $10M_K^*$ (bottom) galaxy templates on a $(I_{814} - K_s)$ vs. K_s colour-magnitude diagram. In each plot the (red, green, blue) (also top, medium, bottom) track corresponds to an (elliptical, spiral, starburst) galaxy template. Some redshift values are marked on the elliptical template track as a reference. The value of $M_K^* = -22.2 - 0.5(1 + z)$ is an approximation derived from the luminosity function analyses by Arnouts et al. (2007) and Saracco et al. (2006), and references therein. The limit magnitude values plotted correspond to $K_s = 22.0$, $I_{814} = 25$.

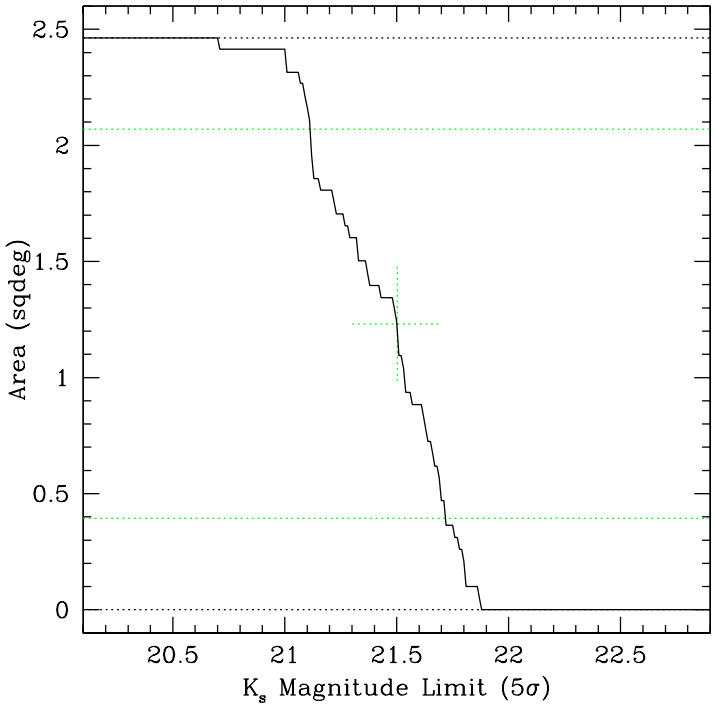

Figure 2.4: Cumulative area covered by the ALHAMBRA K_s-band images as a function of the magnitude limit reached in each one. This calculation uses the nominal 5σ limit in each pointing, and has been corrected using the image masks described in Section 2.3. The horizontal dotted lines mark the area values corresponding to 0, 16, 84 and 100% of the total survey area.

2.1.2 Data reduction

The ALHAMBRA images, as mentioned, have been taken in eight different fields[6]. Given the particular structure of the LAICA focal plane, consisting of four detectors, each one covering approximately 15x15 arcmin^2, whose centers are situated at the corners of a (virtual) 30x30 arcmin^2, one pointing includes four such images. Two neighbouring LAICA pointings produce two horizontal strips in the sky, each of them measuring 60x15 arcmin and separated by 15 arcmin in the vertical direction (Figure 2.5). This is the shape of each of the ALHAMBRA fields[7]. The basic unit in the ALHAMBRA reduction and analysis is a LAICA CCD, which we identify, for example, as F04P01C01 for CCD#1 in the first pointing of the ALHAMBRA-4 field. A full illustration can be seen in Appendix A of M14.

The NIR images provided by the camera OMEGA2000 cover the same area of a single LAICA CCD. The instrument uses a Rockwell HAWAI2 chip detector (Kovács et al. 2004) with 2048x2048 pixels, and an original pixel scale of ~ 0.45 arcsec pixel^{-1}. In order to supply an homogeneous dataset, the NIR images were re-sampled to the LAICA pixel scale (~ 0.225 arcsec pixel^{-1}), which represented an interpolation over a 2×2 grid per pixel. The individual images were dark-corrected, flat-fielded, and sky-subtracted using the iraf package XDIMSUM (Stanford et al. 1995). In order to avoid spurious detections, individual masks were created to account for bad pixels, cosmic rays, linear patterns, blemishes, and ghost images coming from bright stars (Cristóbal-Hornillos et al. 2009). The SWarp Software (Bertin et al. 2002) was used to combine the processed images correcting geometrical distortions in the individual images, using the astrometric calibrations stored in their World Coordinate System (WCS) headers. Once the images were combined, a preliminary source catalogue for each pointing was created and cross-matched with the Two Micron All Sky Survey (2MASS, Cutri et al. 2003) in order to select common objects with high S/N, to be used for calibration purposes. In this work, we present the results obtained using the re-sampled, corrected, combined images.

[6]Only seven have been completely observed and reduced, with ALHAMBRA-1 being unfinished at this stage.

[7]Except for fields ALHAMBRA-4 and ALHAMBRA-5 for which we have only covered in full one LAICA ponting.

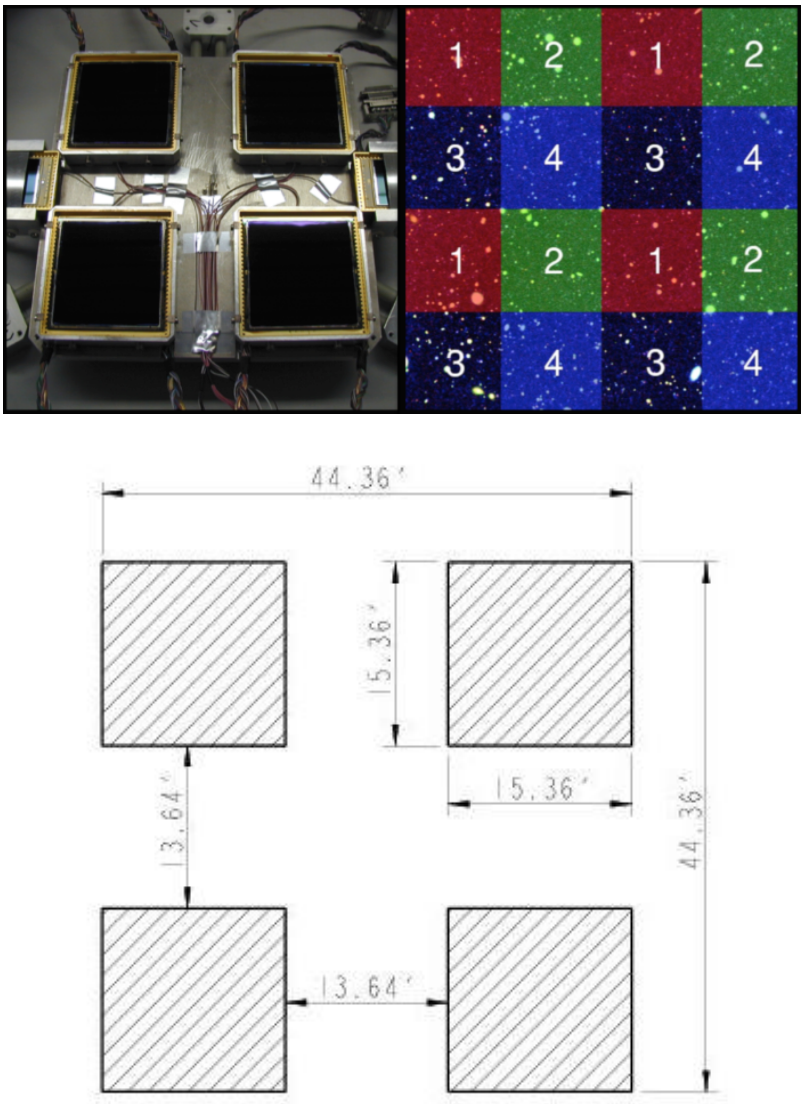

Figure 2.5: Top panel: The LAICA instrument. The left panel shows the geometry of the instrument focal plane. The right panel shows the distribution of the four pointings (differently coloured) and the position of each CCD in each pointing, that are necessary to cover a full square degree. Bottom panel: Dimensions of the CCDs in arc minutes (https://www.caha.es).

For each combined and fully calibrated NIR image we have used the same method presented in Arnalte-Mur et al. (2014) to calculate an associated pixel mask that accounts for possible remnant cosmetic problems, not homogeneously covered image borders, and saturated stars. As is explained in Section 2.3, after masking, the total area covered by our catalogue amounts to 2.463 square degrees.

Flux calibration of the 20 medium-band optical filter images was achieved using relatively bright stars in each of the CCDs as secondary standards (Aparicio Villegas et al. 2010), and anchoring them to their Sloan Digital Sky Survey photometry (York et al. 2000). Flux calibration of the JHK_s images was based directly on the Two Micron All Sky Survey (2MASS) (Cutri et al. 2003). After the corrections and corresponding combinations of the NIR images, the zero-point offsets were computed using the common ALHAMBRA sources with higher S/N (Cristóbal-Hornillos et al. 2009, Cristobal-Hornillos et al. in preparation).

2.2 Source detection and photometry

Source detection was performed using SExtractor (Bertin & Arnouts 1996) over each of the K_s-band images. Before the detection process, SExtractor applies a filter to detect faint, extended objects. Among the different filters offered we choose a 5-pixel FWHM Gaussian kernel (`gauss_5.0_5x5.conv`). We previously measured the FWHM of a sample of non-saturated stars in each image, using the IRAF package `imexam`. We obtain a FWHM$\sim$ 5 pixels (*i.e.* approximately 1.1 arc seconds), which leads us to the selection of that kernel.

As it is usual in this kind of work, in order to optimise the number of real sources we performed detection both on the original images and their negatives, using different sets of parameters, exploring parameter space to maximise the number of real detections while securing the least possible spurious ones. Some example results of this analyses are plotted in Figure 2.6, from where we finally opted for a minimum area of 5 connected pixels with signal greater than 1.2 times that of the background noise[8]. At first order this would imply a minimum S/N $\gtrsim 3$ for the detected sources. As already mentioned in Section 2.1.1 the median

[8] That is, `DETECT_THRESHOLD` = 1.2 and `DETECT_MINAREA` = 5

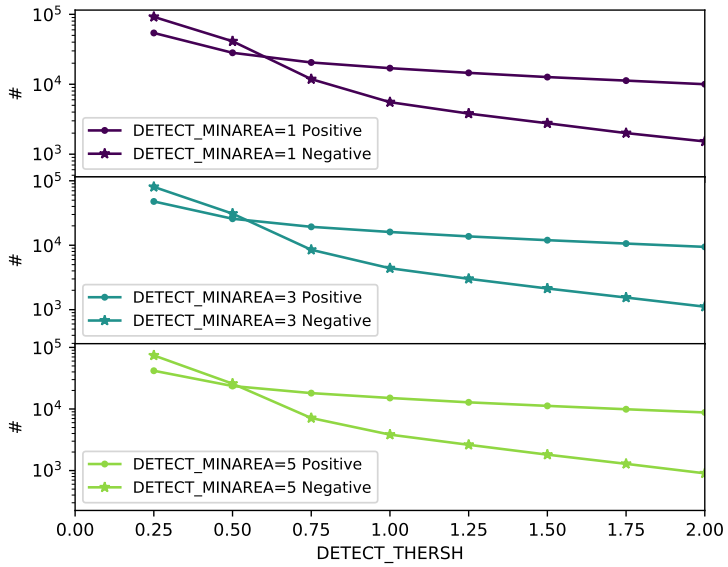

Figure 2.6: Detected source counts in the positive (circles) and negative (stars) K_s-band images for different values of SExtractor's input parameters as a function of both `DETECT_THRESHOLD` and `DETECT_MINAREA`.

5σ limiting magnitude of our images is $K_s \simeq 21.5$. A more detailed and realistic analysis of the photometric depth will be presented in a next section.

Photometry was carried out over the 20+3 ALHAMBRA images plus the synthetic F814W one using SExtractor in dual image mode, using the K_s-band images for detection in every case. We introduced as input to SExtractor the values of the zero points for each image, as calibrated during the reduction process. We changed the values of the parameters `DETECT_THRESHOLD` and `DETECT_MINAREA` in the photometry mode in order to define the photometric apertures in the same way as was done in the case of the ALHAMBRA optical catalogue. Obviously the individual apertures themselves will be different, as (i) the brightest part of each galaxy, that defines the aperture, will be intrinsically different in the K_s and the F814W bands, and (ii) the seeing in the NIR images is generally and significantly

better than that in the optical ones[9]. One of the most important checks that we will perform on the final catalogue will be devoted to check the compatibility between the general-purpose ALHAMBRA catalogue photometry and our own in those objects they have in common.

2.2.1 Photometric errors

A proper estimation of the photometric errors represents an important task for photometric redshift estimation, since the techniques used to compute them rely heavily on the photometric uncertainties. When SExtractor estimates the photometric uncertainties, it assumes that the noise properties are characterised by a Poisson distribution. This is correct only if there are no correlations between pixels.

The reduction and re-sampling processes executed on the NIR images cause significant correlations between pixels, and the assumption of a standard Poisson estimation of the background noise leads to a significant underestimation of the real photometric errors. This underestimation is aggravated in the case of faint sources (Cristóbal-Hornillos et al. 2009).

Here we describe the procedure that we followed for the estimation of the final error flux of each catalogue source. In a first step, we generated a file with random coordinates and using the astronomical software Sextractor, we thrown ~ 3150 apertures over the ALHAMBRA images. The Sextractor output file includes the parameter `FLUX_APER` that provides the flux measurement. We repeated the process for different aperture diameters, ranging from 2 to 15 pixels.

In order to measure the background error it was necessary to exclude those measurements that may be contaminated by flux due to weak sources or nearby bright sources (Fernández-Soto et al. 1999). To avoid that effect and to be able to obtain a valid estimate of the Gaussian distribution parameters we performed a maximum likelihood fit only over the negative part of the flux distribution in the empty apertures. In the top panel of Figure 2.7 we show the background

[9]As shown in M14, the median seeing is $\sim 0.9''$ for the NIR images, $\sim 1.1''$ for the visible images, and $\sim 1.0''$ for the F814W synthetic images—which are generated selecting preferentially those with good seeing within the adequate wavelength range.

distribution and the best-fit Gaussian curve obtained for each aperture size.

Following the method presented by Labbé et al. (2003), we estimated the background error using the relation:

$$\sigma_F^2 = \left[\sigma_0 \cdot K \cdot \sqrt{N} \cdot \left(a + b\sqrt{N}\right)\right]^2 \tag{2.2.1}$$

with K being the value of the weight map[10] in the region where the source is measured, σ_0 the background RMS, and N the area of the aperture in each case, as given by the `ISOAREA_IMAGE` SExtractor output value.The term that includes the a parameter encloses the errors due to correlation between neighbouring pixels, while the b parameter term includes the large-scale correlated variations in the background. Both the a and b parameters were obtained in the fitting process described in Figure 2.7. We first obtain the best Gaussian fits of the distribution of the counts contained in randomly positioned apertures of different sizes in our image (top panel of Figure 2.7. At next stage we fit the values of the same Gaussian values to the aperture size (bottom panel of Figure 2.7).

Two more terms were added to the final flux error equation: a second term was added in order to estimate the shot noise error related to the source flux F and the gain G, and a third term due to the calibration uncertainty $\Sigma_{\mathrm{PhotCalib}}$.

The final flux error for each source was calculated as:

$$\sigma_F^2 = \left[\sigma_0 \cdot K \cdot \sqrt{N} \cdot \left(a + b\sqrt{N}\right)\right]^2 + \left(\frac{K^2 \cdot F}{G}\right) + \Sigma^2_{\mathrm{PhotCalib}}. \tag{2.2.2}$$

Finally, the AB magnitude uncertainties were calculated applying the equation:

$$\sigma_{\mathrm{M}} = 1.0857 \cdot \frac{\sigma_{\mathrm{F}}}{\mathrm{F}}. \tag{2.2.3}$$

2.3 Angular selection mask

In order to take into account possible position-dependent selection effects, we built an updated version (v2) of the ALHAMBRA survey angular selection mask presented in Arnalte-Mur et al. (2014). These masks were built to define the sky

[10]The weight map measures the relative exposure time per pixel within the same pointing for a given filter.

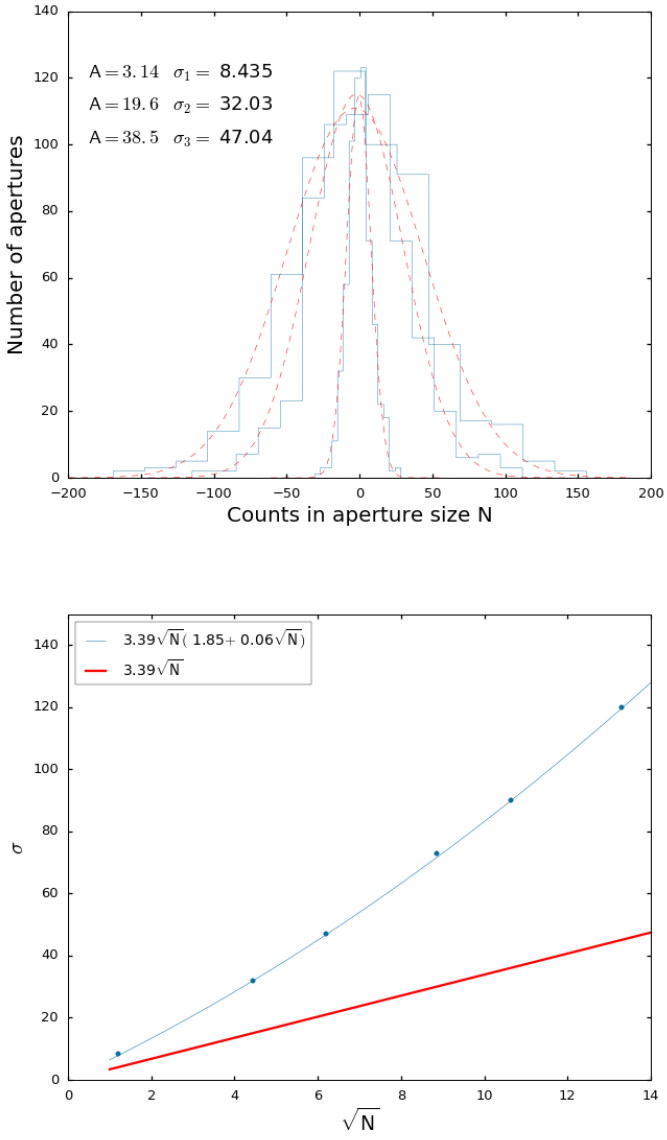

Figure 2.7: Top: Example distributions of the counts contained in randomly positioned apertures of different sizes (A is the apertures area), together with their best-fit Gaussian models. Bottom: Fit to the values of the same Gaussian values to the aperture size $\sqrt{N}$.

area which has been reliably observed, excluding regions with potential problems. The latter include regions with low exposure time next to the borders of the CCDs, regions next to bright stars or saturated objects and regions where obvious defects in the images are found (for details, see Arnalte-Mur et al. 2014).

In this new version we built two different masks following this approach, one based on the synthetic F814W images, and the other based on the K_s images. The optical-based angular mask is very similar to the one presented in Arnalte-Mur et al. (2014), with two small differences. First, we have used an updated version of the *flag* images that describe the regions with appropriate effective exposure times. These now include some small areas (mainly in the ALHAMBRA-2 field) that were previously incorrectly excluded. Second, we now mask out regions around bright and saturated stars using a shape that properly matches the diffraction spikes (see Figure 2.8 for an example). The NIR-based angular mask was created following the same approach, but based on the map of effective exposure times and saturated objects in the K_s images. We take into account the fact that, due to the different disposition of the LAICA and OMEGA2000 cameras, the orientation of the diffraction spikes is rotated 45° between the optical and NIR images.

We combined the optical- and NIR-based masks into a final mask that therefore describes the sky region that has been reliably observed both in the optical and in the NIR. From this final mask we excluded some small regions to avoid overlap between neighbouring CCDs. Figure 2.8 is an illustration of the resulting ALHAMBRA survey mask (v2) for one of the fields (ALHAMBRA-3). The total effective area of the survey according to this angular selection mask is $A_{\rm eff} = 2.463\,{\rm deg}^2$, and the effective areas for each of the fields are listed in Table 2.1. The small increase ($\sim 3\%$) in area with respect to version v1 of the masks (Arnalte-Mur et al. 2014) is due to the aforementioned differences in the optical-based masks.

Even after the masks were applied over the images we observed small residual, periodic electronic ghost patterns over detector rows and columns around some very bright, saturated stars in the K_s-band images. We individually checked and removed a total of 59 sources in these problematic areas from the catalogue.

The angular masks were generated using the MANGLE software (Swanson et al. 2008), and we have made them publicly available (in MANGLE's *Polygon* format) together with the data catalogue. We list in the data catalogue all objects de-

Field name	RA (J2000)	DEC (J2000)	Area (full) deg^2	Area (masked) deg^2
ALHAMBRA-2	02 28 32.0	+00 47 00	0.441	0.402
ALHAMBRA-3	09 16 20.0	+46 02 20	0.500	0.415
ALHAMBRA-4	10 00 28.6	+02 12 21	0.250	0.209
ALHAMBRA-5	12 35 00.0	+61 57 00	0.250	0.218
ALHAMBRA-6	14 16 38.0	+52 25 05	0.500	0.415
ALHAMBRA-7	16 12 10.0	+54 30 00	0.500	0.414
ALHAMBRA-8	23 45 50.0	+15 34 50	0.500	0.390
		TOTAL	2.941	2.463

Table 2.1: ALHAMBRA K_s-band catalogue areas for each fieldk.

tected in the full K_s-band images, and column `MASK_SELECTION` in the catalogue indicates whether a given object is inside the angular selection mask or not. All the analyses performed in this paper consider only the objects inside the mask (with `MASK_SELECTION = 1` in the catalogue), and this is the approach we recommend for any further statistical analysis based on this catalogue. We include, however, all objects in the catalogue files irrespective of their MASK value, as potentially some particular object could be of interest to other researchers.

2.4 K_s-band completeness

A key ingredient for any analysis to be performed with the catalogue is the measurement of its completeness. As was described above, our survey includes 48 independent images, distributed over seven different fields. Each one of them was observed and analysed using the same parameters, exposure times and instruments. However, the observing conditions in each case were very different: the period of time over which the observations took place covered several years during which the instruments passed successive cycles. Obviously the atmospheric conditions were also widely different between the observing runs.

Therefore the limiting magnitudes that define the depth of our catalogue vary

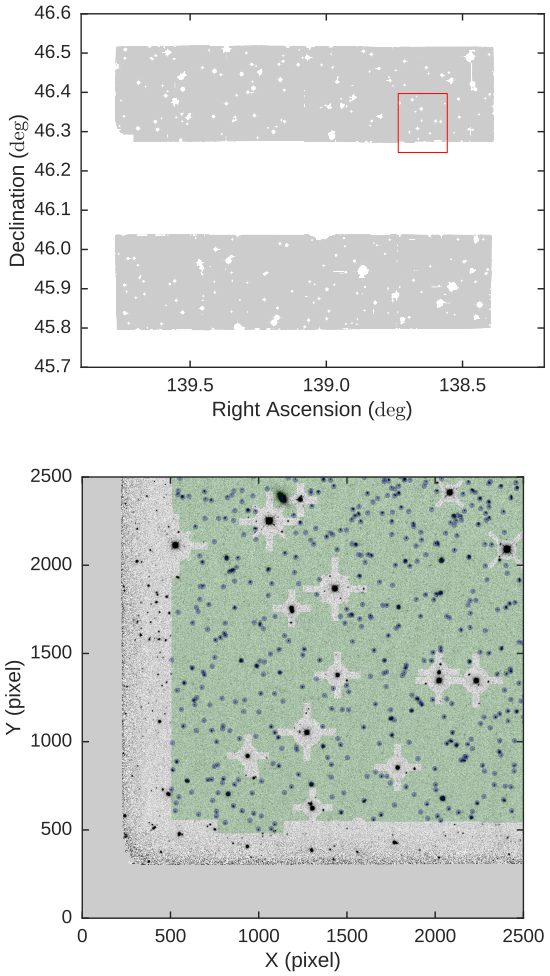

Figure 2.8: Illustration of the ALHAMBRA survey angular mask (v2) for the ALHAMBRA-3 field. Top: angular mask for the complete field. The shaded area corresponds to the region included in the selection. This shows the peculiar ALHAMBRA field geometry described in Sect. 2.1.2 and in M14. The red rectangle marks the area shown in the bottom image. Bottom: Detail of one typical ALHAMBRA K_s image, showing the corresponding angular selection mask (shaded in green). The blue points correspond to detected objects included in our catalogue. This image corresponds to an area of $\sim 8 \times 8$ arcmin^2. We see how regions near the border of the CCD image are excluded from the mask. We also exclude a cross-shaped region around each saturated object, with the vertical/horizontal crosses corresponding to diffraction spikes in the optical F814W image, and those at 45° corresponding to spikes in the K_s image.

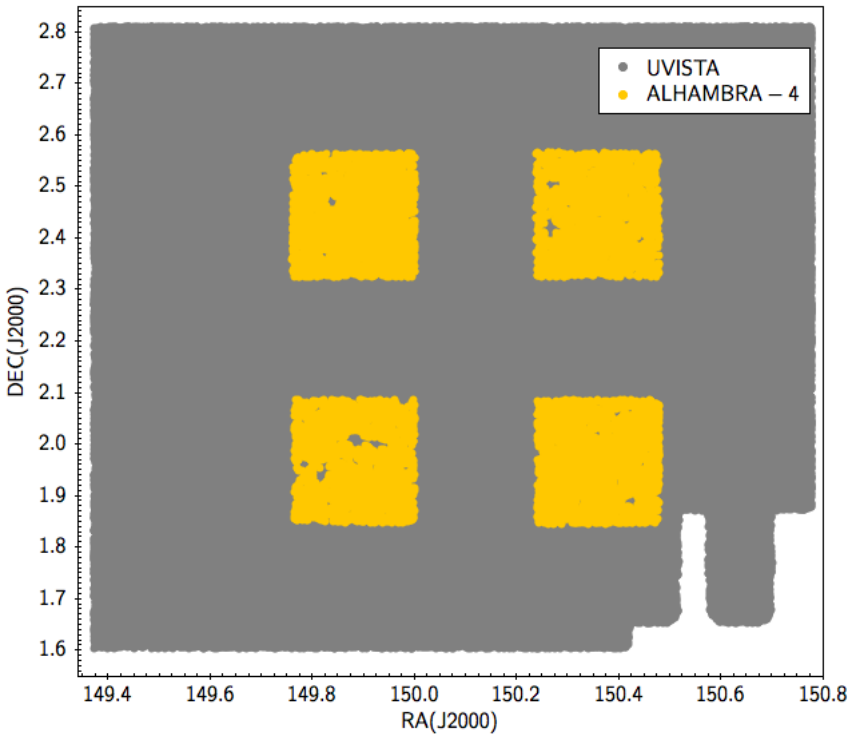

Figure 2.9: ~ 0.21 deg^2 overlapping area between the UltraVISTA COSMOS field (in grey) (McCracken et al. 2012) and the ALHAMBRA-4 field (in yellow).

widely from one field to another, and also within the different CCDs in the same field. In order to minimise this effect we need to estimate a completeness function that will allow us to compute the corrections at the faint end of the galaxy number counts.

We have already mentioned that the ALHAMBRA pointings were chosen to overlap with well-known fields. In particular, an area of ~ 0.21 deg^2 of the ALHAMBRA-4 field overlaps with the UltraVISTA COSMOS field (McCracken et al. 2012) (See Figure 2.9). Since the magnitude limit in the UltraVISTA K_s-band selected catalogue for this field is $K_s \sim 24$ (Muzzin et al. 2013), and the ALHAMBRA magnitude limit is $K_s \sim 22$, we can estimate our K_s-band completeness function using the UltraVISTA COSMOS data as reference.

We will estimate the completeness fraction of our survey as a function of the

K_s-band magnitude using the UltraVISTA data as reference. Only one of our fields (ALHAMBRA-4) overlaps with this survey, so we will calculate an accurate completeness function using the four pointings of this field and then scale the results to the rest of the survey.

The basic idea is to compare the number of sources detected in the common area by UltraVISTA and ALHAMBRA in each magnitude interval. We have fitted the usual Fermi function

$$F(m) = [1 + \exp((m - m_c)/\Delta m)]^{-1} \tag{2.4.4}$$

to the data in each of the four CCDs where we have observations from both surveys. The parameters m_c and Δm correspond respectively to the 50% completeness magnitude and to a measurement of the width of the decreasing part of the Fermi function. We remark that the fits were adjusted to the data themselves, with no binning of the data involved.

In a first run we fitted each of the four CCDs separately, and obtained the values of m_c and Δm in all four cases. We checked that the widths were compatible with each other–in all cases the value was close to $\Delta m = 0.3$. We also checked that the value of the completeness limit indicator m_c was strongly correlated to the nominal 5σ limit of each field, which allows us to use the latter as a proxy for the former. In particular, this will be crucial to extend our analysis to the fields which cannot be directly compared to UltraVISTA or other deeper surveys.

We repeated the fit a second time, in this case to the whole ALHAMBRA-4 field and substituting the parameter m_c for $(m_c - m_{5\sigma}^{(i)})$ $(i = 1, \ldots, 4)$, so that we obtain a single completeness function which can be applied to all four CCDs by plugging the value of the nominal 5σ detection limit in each CCD, thus "sliding" the global Fermi function to its adequate position. We plot in Figure 2.10 the completeness function thus derived.

Our analysis also includes the correction by the completeness function of the UltraVISTA survey itself as presented by the authors, although at these magnitudes (which are bright compared to its limit) the correction is very small: the completeness fraction of the UltraVISTA catalogue is $> 90\%$ for magnitudes brighter than K_s=23.4 (Muzzin et al. 2013).

We then use the full completeness function estimate to correct the ALHAMBRA K_s band number counts. In order to obtain an accurate estimate of the

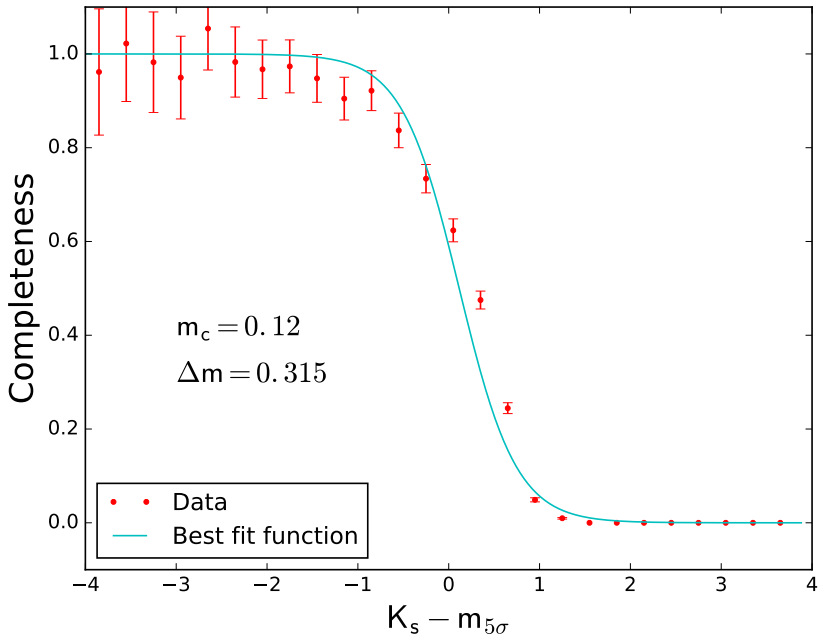

Figure 2.10: Global completeness fraction for the ALHAMBRA-4 field as a function of the K_s magnitude. The completeness has been calculated comparing our counts with those in Muzzin et al. (2013), taking into account the UltraVISTA completeness function correction.

number counts we have summed the number of objects in each magnitude interval, weighing each individual object both with the value of the completeness correction corresponding to its magnitude and with the accessible masked area in the particular CCD where it is observed. We have extended the number counts out to the 60% completeness limit of each pointing, which allows us to reach the global completeness limit $K_s \approx 21.9$, as can be seen in Figure 2.11. The global data are well fit with a power-law, and as expected we observe a reasonable behaviour of the number counts down to the catalogue limit.

Finally, we have also checked that the results presented in this work are compatible with the NIR galaxy counts that were presented in Cristóbal-Hornillos et al. (2009) for the ALHAMBRA-8 field.

We show here the results obtained when the (CCD-dependent) completeness correction is applied to each pointing and the final result is compiled. Figure 2.11 shows the result of such procedure with the total counts in our catalogue compared to those in the deeper UltraVISTA sample.

2.5 Star-galaxy separation

SExtractor outputs for each object in the catalogue a value for the `CLASS_STAR` parameter. This parameter estimates the stellarity of each source according to morphological criteria. However, given the average seeing of the ALHAMBRA images, this value is not trustworthy for most of the objects in the catalogue. Moreover, even if the average seeing in our images were much better, we may still face cases of compact galaxies which could be morphologically misidentified as stars. We must thus apply an additional classifying method to improve our star-galaxy separation.

As described in Huang et al. (1997), a colour-colour diagram combining near-infrared and visible colours can provide a simple albeit accurate criterion to discriminate between stars and galaxies. We will use the colour (F489M-I_{814}) in the optical range and the $(J - K_s)$ colour in the NIR. Figure 2.12 (top) shows such a colour-colour plot where we have applied a magnitude selection limit $K_s < 18$ in order to avoid any dispersion due to large photometric uncertainties and see the stellar locus as a well-defined area.

The line that separates the loci corresponding to galaxies and stars is marked

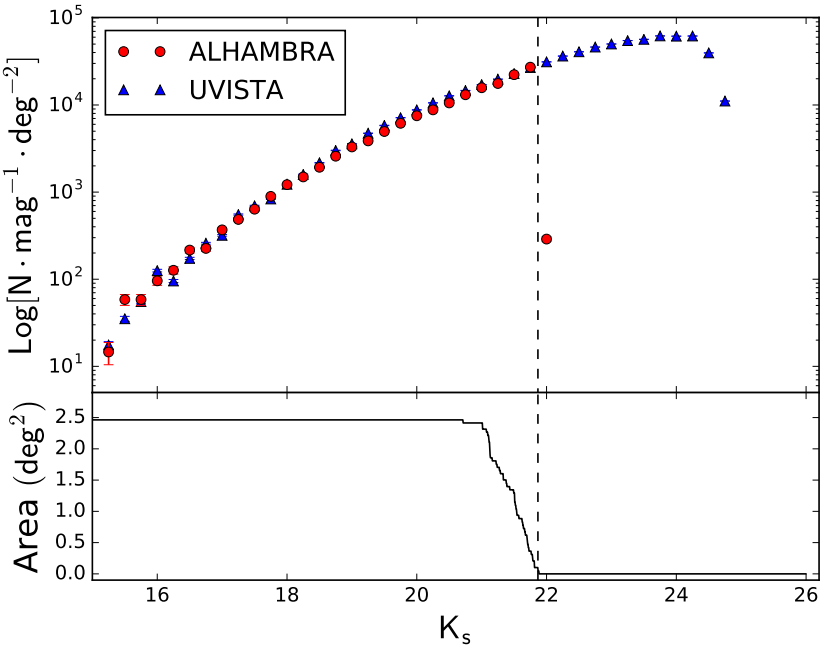

Figure 2.11: Corrected galaxy number counts in the K_s-band ALHAMBRA catalogue (red points) and UVISTA (blue points). The vertical dashed line marks the magnitude at which the completeness falls to 60% for the deepest images. The lower panel shows the available survey area at each magnitude, using as limit for each CCD the value $(m_{5\sigma} + m_c)$ of the half-completeness point in the Fermi function.

on the plot and given by:

$$\mathrm{F489M} - I_{814} = 3.61 * [(J - K_s) + 0.275] \quad [(J - K_s) < 0.17] \tag{2.5.5}$$

$$\mathrm{F489M} - I_{814} = 6.25 * [(J - K_s) + 0.087] \quad [(J - K_s) \geq 0.17]. \tag{2.5.6}$$

Black stars mark the objects that SExtractor classifies as stellar (`CLASS_STAR` > 0.95) in the range where such classification is accurate ($K_s < 18$). In the bottom panel on Figure 2.12 we show the same colour-colour diagram applied to our whole sample. As a further check, we have also included amber markers at the positions where stars in the Next Generation Spectral Library (HST/STIS NGSL, Gregg et al. 2004) would fall.

We have included in our catalogue a column called `COLOR_CLASS_STAR`, which takes the value 0 for objects classified as galaxies using this diagram and 1 for those classified as stars. We have also defined in the colour-colour diagram an area where classification is not clean, within which we have assigned the value 0.5 to all objects—they are marked in green and they fill the grey area in Figure 2.12 (bottom). In addition, we have compared the stellarity of the sources in this work and M14, finding that less than 0.1% of the common sources present inconsistencies.

2.6 Photometric redshifts

Photometric redshifts for all galaxies in the catalogue have been calculated using the Bayesian Photometric Redshift code (BPZ2.0, Benítez 2000, Benítez in preparation). BPZ uses a Spectral Energy Distribution (SED)-fitting method (Koo 1985; Lanzetta et al. 1996) to approach the photometric redshift estimation. The method fits the observed colours of a galaxy to theoretical SED templates of different galaxy types displaced in redshift space, applying the adequate intergalactic extinction/absorption correction in each case. The handicap of this method is the possibility of different templates sharing similar colours at different redshifts, and the main difficulty lies in trying to avoid this colour-redshift degeneracies. BPZ computes photometric redshift and galaxy type for each object using a Bayesian probability using as input the measured colours of each galaxy and the apparent magnitude on a reference band. It includes a prior probability that provides information on the magnitude-redshift-type space that allows to

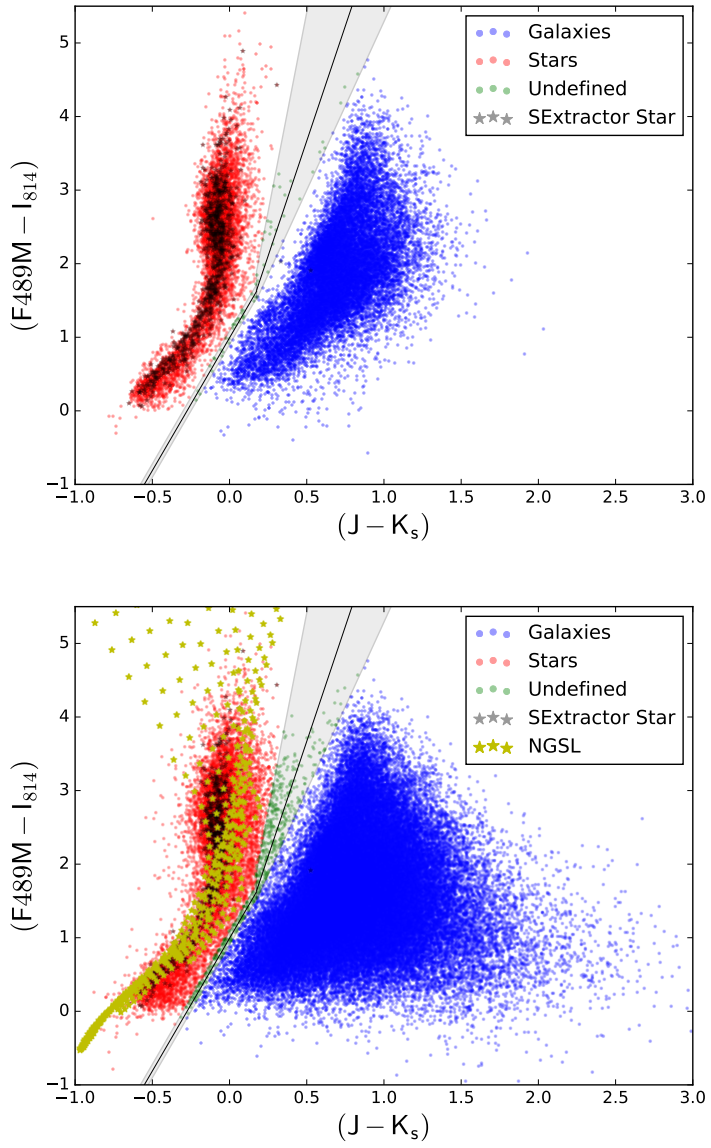

Figure 2.12: Colour-colour diagram used to perform the photometry-based star-galaxy separation. In the top panel we restrict the plot to $K_s < 18$ in order to show clearly the different loci occupied by stars (red) and galaxies (blue), as well as the objects classified as stellar by SExtractor (black). The bottom panel shows the same diagram for the whole catalogue. The grey area encloses the objects that are not securely identified either as galaxies or stars, and the amber markers correspond to the positions of stars included in the NGSL.

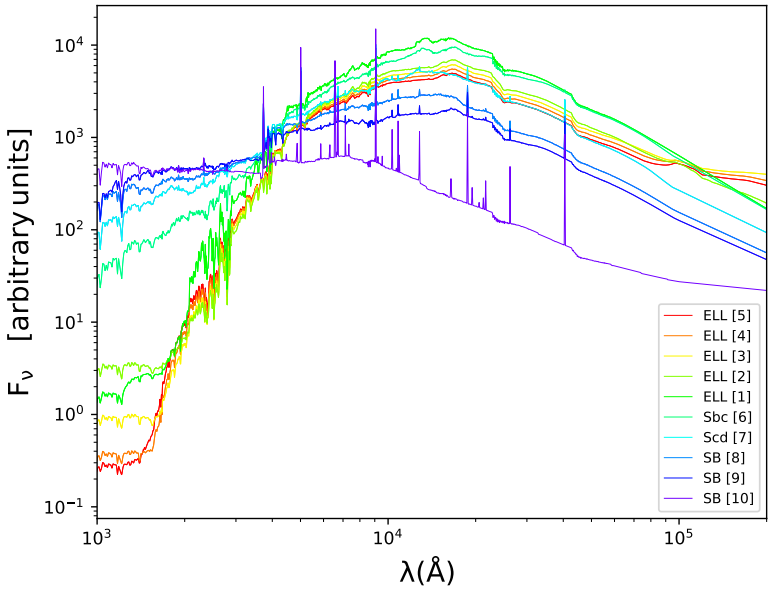

Figure 2.13: SED templates used by BPZ2.0 for the estimation of the redshift distribution in the ALHAMBRA K_s-band catalogue. The models in the library range from elliptical galaxies to starburst galaxies

improve the accuracy of the best-fit values and minimises the number of redshift outliers. The output consists on a probability distribution function $P(T_B, z)$ for each galaxy in the sample, where T_B is the galaxy tipe and z the photometric redshift.

A total of 10 different galaxy spectral energy distribution (SED) templates were used: five for elliptical galaxies, two for spiral galaxies and four for starburst galaxies. The SED types are numbered following a sequence from $T_B = 1$ to $T_B = 10$ (see Figure 2.13). The spectral fitting includes emission lines and dust extinction within the templates themselves, and not as separate parameters. Linear interpolation between the types was included in order to improve the coverage of SED-space and make it denser. BPZ calculates the likelihood of the observed photometry for all the combinations of redshift and SED type in the given parameter space, and combines it within a Bayesian formalism with priors calculated as distributions of the density of the different spectral types as a function of redshift and magnitude, compiled from observations from the Hubble Deep Fields

and COSMOS. The output of the code includes both best-fitting solutions, one coming from the likelihood analysis alone and the second one including the prior information. It also outputs the full probability distribution function PDF(T_B, z) which should be used preferentially for the ensuing analyses.

BPZ calculates an extra parameter which will be very important for us: the *Odds* parameter, which corresponds to the integration of the PDF within a narrow redshift range around the best-fitting solution. High values of the *Odds* parameter mark objects whose redshift is very well determined, with a narrow, single peak in the probability distribution. Low values of *Odds* signal either objects that due to poor-quality photometry or to a lack of an adequate SED in our library of templates suffer a poor fitting; or objects that inhabit an area of colour space which has an intrinsic degeneracy between two different redshifts[11].

The K_s-band catalogue includes as output from BPZ 2.0: the photometric redshift Bayesian estimate z_b, the associated SED best-fitting type T_B, the *Odds* parameter, the maximum-likelihood estimates of redshift and SED type, and some derived measurements like absolute magnitudes and an estimate of the stellar mass[12].

[11] This should in fact be a minimal problem for ALHAMBRA because of the 23 photometric bands that are used, but can be more serious in our case because for very red objects we are sometimes left with detections only in a few of the reddest filters.

[12] The stellar mass is a rough estimate, derived from the flux normalisation and SED type.

Chapter 3

Catalogue Properties

In this chapter we present the K_s-band catalogue main properties. We present the galaxy counts and colour-magnitude diagrams. We then show a series of tests on the catalogue that we have performed in order to ensure the validity of the photometric calibration and the accuracy of the photometric redshifts we have derived. We introduce the photometric redshift distribution, including a study of the different galaxy type distributions.

In anticipation of the work that we will develop in the next chapter we also perform a brief analysis to study the reliability of the cross-match between the K_s-band catalogue and data from the *Spitzer Space Telescope* Infra-Red Array Camera (IRAC, Fazio et al. 2004) in those fields where such data are available. We use data obtained in the ALHAMBRA-7 (ELAIS-N1, Rowan-Robinson et al. 1999) overlapping area and show some of the benefits of including this new information in the infrared spectral range.

Finally, we also include in this chapter a brief study of the clustering properties of a subsample of red galaxies at moderate redshift. We present the results that we have obtained, which extend the study made for the general-purpose ALHAMBRA optical catalogue in Hurtado-Gil et al. (2016) to higher redshifts, previously selected against because of the I_{814}-band selection.

Part of the contents of this chapter have been published in Nieves-Seoane et al. (2017).

Field name	RA (J2000)	DEC (J2000)	Area (full) deg^2	Area (masked) deg^2	Sources (full)	Sources (masked)	Sources/deg^2 (masked)
ALHAMBRA-2/DEEP2	02 28 32.0	+00 47 00	0.441	0.402	19989	16546	$4.12 \cdot 10^4$
ALHAMBRA-3/SDSS	09 16 20.0	+46 02 20	0.500	0.415	19489	16654	$4.01 \cdot 10^4$
ALHAMBRA-4/COSMOS	10 00 28.6	+02 12 21	0.250	0.209	11154	9587	$4.59 \cdot 10^4$
ALHAMBRA-5/HDF-N	12 35 00.0	+61 57 00	0.250	0.218	9528	8549	$3.92 \cdot 10^4$
ALHAMBRA-6/GROTH	14 16 38.0	+52 25 05	0.500	0.415	17051	14565	$3.51 \cdot 10^4$
ALHAMBRA-7/ELAIS-N1	16 12 10.0	+54 30 00	0.500	0.414	18045	15262	$3.69 \cdot 10^4$
ALHAMBRA-8/SDSS	23 45 50.0	+15 34 50	0.500	0.390	16116	13019	$3.34 \cdot 10^4$
		TOTAL	2.941	2.463	111372	94182	$3.82 \cdot 10^4$

Table 3.1: ALHAMBRA K_s-band catalogue counts.

3.1 Catalogue counts

The ALHAMBRA K_s-selected catalogue covers 7 ALHAMBRA fields[1]. As we have mentioned is Chapter 2, a total of 48 CCDs are included in the final catalogue. The full data set includes the photometry in the 20+3 ALHAMBRA filters, performed by SExtractor, and photometric redshifts computed by BPZ2.0. The results include the best-fitting galaxy model from those included in the BPZ2.0 library. Each individual catalogue, corresponding to a single pointing (one CCD area) includes a header that documents the column information. We include in Appendix A a list with the content and description of the individual columns in each catalogue file. In this part of the work magnitudes are given in the AB system (Oke & Gunn 1983).

Our complete catalogue includes photometry for 94,182 sources. They are distributed in the ALHAMBRA fields as shown in Table 3.1. The derived density is $\sim 38,000$ sources per square degree.

In the top panel of Figure 3.1 we show the histogram of the raw K_s-band magnitude counts. We have separated stars and galaxies using the star-galaxy classifier described in Section 2.5. As expected, stars are dominant until $K_s \approx 17.5$. From this magnitude on, the galaxy fraction increasingly dominates the counts. In the bottom panel of Figure 3.1 we see how the fraction of stars falls, representing less than 10% of our counts from $K_s \approx 20.5$.

The top panel of this latter plot can be compared to Figure 2.11, where we

[1] ALHAMBRA-1 has not being fully reduced at this stage.

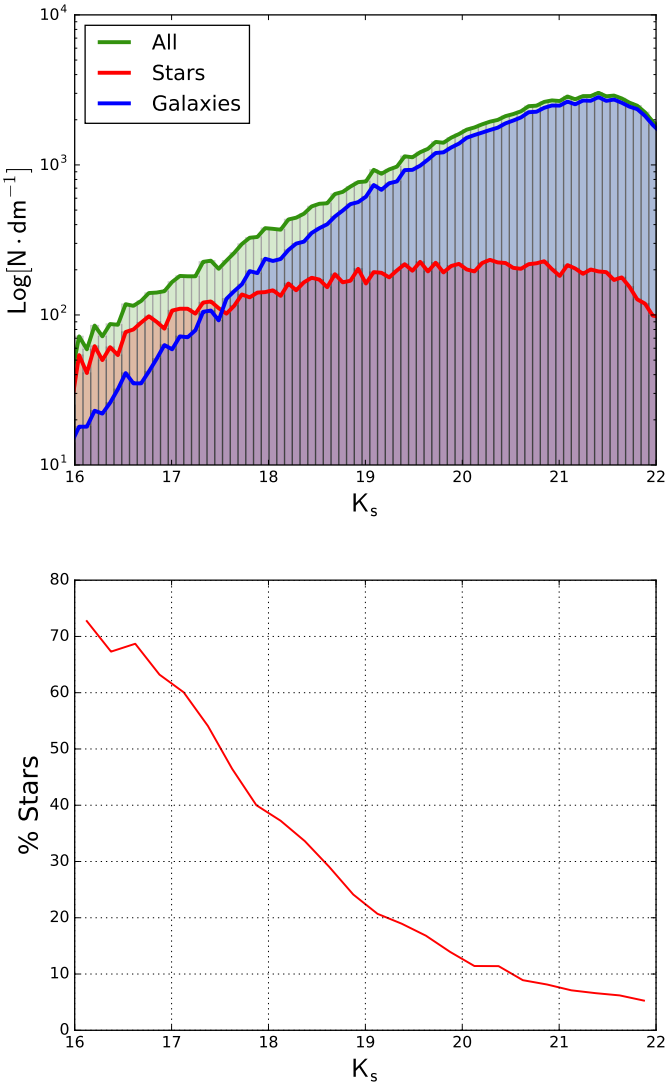

Figure 3.1: Top panel: Raw number of detected sources on the K_s image. The green line corresponds to the full sample, whereas the red and blue colours correspond to the star and galaxy counts, respectively. Bottom panel: Percentage of stars in the total sample as a function of magnitude.

showed the galaxy number density vs magnitude plot, once the completeness correction calculated in Section 2.4 is applied. In that case we can extend the range over which the counts are accurate out to $K_s \approx 22$. Comparison with previous works shows that the counts are consistent, and allows us to perform the following tests.

3.2 Colour-magnitude diagram

Our main motivation to provide a K_s-band selected sample is to cover the area of the colour-magnitude diagram where sources with high $(I_{814} - K_s)$ colour reside. These objects are detected in the K_s-band catalogue, but many of them have barely any signal in the F814W images. In fact, as expected when a deeper image is used to detect objects and perform photometry in a second band, many objects that went undetected in the original catalogue (because their detected flux did not reach the minimum necessary to fulfill the detection criteria) do have positive flux once the apertures are defined with a second deeper/redder band.

Figure 3.2 shows the $(I_{814} - K_s)$ vs K_s colour-magnitude diagram for the ALHAMBRA-4 field in the top panel, and for the whole ALHAMBRA K_s-band catalogue in the bottom panel. We present both, so that the reader can see a cleaner case with fewer points and more homogeneous data and magnitude limits (the single ALHAMBRA-4 field), as well as the diagram for the whole catalogue. The shadowed bands represent the magnitude limits for the K_s images (vertical) and the F814W images (diagonal), and their width is due to the inhomogeneity of the achieved magnitude limits. Black dots and contours correspond to the ALHAMBRA catalogue (I_{814}-band selected), while the blue dots and contours correspond to the K_s-band selected catalogue. We signal with red points the sources detected in the latter with no counterpart in the M14 catalogue. We have detected 503 new sources in the ALHAMBRA-4 field alone, and a total of 4305 new sources in the full K_s-band catalogue. This diagram can be directly compared with the one in Figure 2.3, and shows that this new catalogue does indeed fill the area that corresponds to moderate-redshift, high-luminosity, intrinsically red sources.

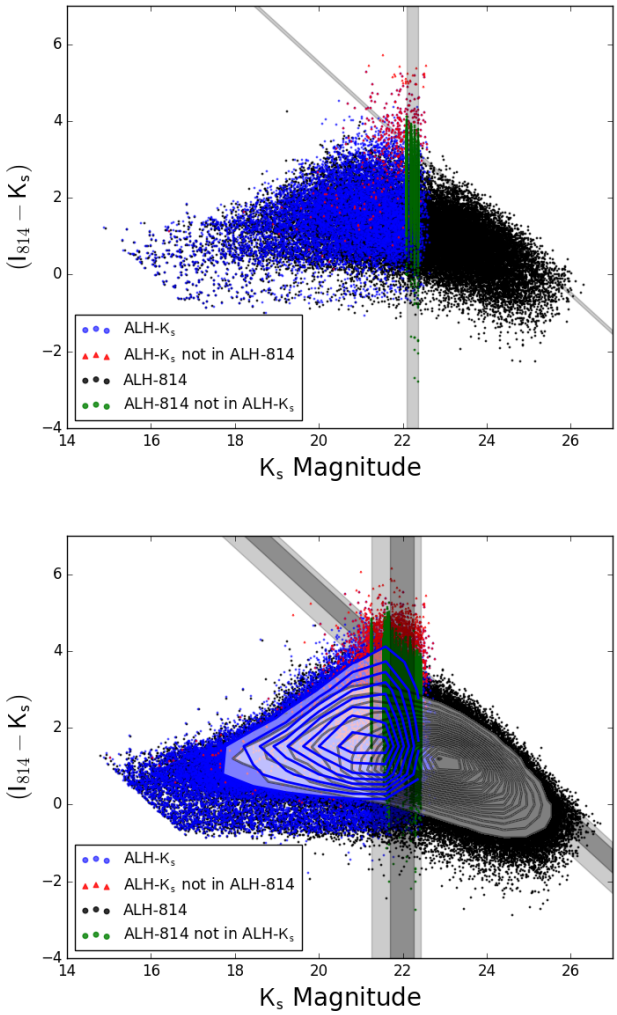

Figure 3.2: Colour-magnitude diagrams. The top panel shows the one corresponding to the ALHAMBRA-4 field alone, and the bottom panel shows the full catalogue. Black points (and contours) are objects in the ALHAMBRA F814W-band selected catalogue, while blue points (and contours) come from this work. The red points correspond to sources detected in the K_s-band image that have no counterpart in the optical selected catalogue. Conversely, the green points mark objects in the F814W catalogue with no K_s-band flux detected. Grey bands mark the K_s (vertical) and the I_{814} (diagonal) 3σ magnitude limits. As each CCD has different properties, we represent them using a shadowed band spanning the range from the minimum to the maximum value. In the bottom panel the band is darker in the central 68% of the CCD magnitude limit values.

3.3 Tests of photometric calibration

There are two obvious tests that we can perform to check the quality of our photometry: a first, basic test will be to link the photometry that we are measuring with the one previously published in the ALHAMBRA catalogue. Our catalogue, being based on a shallower image, includes only $\sim 20\%$ of the targets that ALHAMBRA includes over the same area, and uses image-defined apertures that can be significantly different, particularly in the case of targets which are faint in one or both of the detection images. However, over the common sample and in particular for bright objects, the photometry must be fully consistent. A second test will imply comparison with the aforementioned UltraVISTA catalogue, that overlaps a large part of our ALHAMBRA-4/COSMOS field and reaches ~ 2 magnitudes deeper.

3.3.1 Comparison with M14

We have cross-matched our ALHAMBRA K_s-selected catalogue with the main ALHAMBRA catalogue published in M14, which was selected using a synthetic F814W image for detection. The combined catalogue includes a total of 89,877 sources (77,568 of them galaxies) for which we have 23-band photometry measured with different apertures in each of our catalogues.

We have compared the K_s-band photometry of each object in this work with the one in M14, and show the result in Figure 3.3. As expected, there is hardly any observable bias in the comparison for the bright sources ($K_s<19$), and the net average difference is comparable to or smaller than the typical photometric uncertainty. The bottom panel in Figure 3.3 shows the distribution of the magnitude differences for bright sources, whose median is ≈ 0.03 magnitudes. This value indicates that the K_s magnitudes in the original ALHAMBRA catalogue are (in average) slightly brighter than the ones we obtain. We have tested that this effect is caused by the fact that the apertures defined by the F814W image are larger than the ones defined by the K_s-band, which pushes for a slightly larger flux to be measured in them[2]. We must insist that, in any case, both the scatter

[2]We must remark, however, that this effect is strongly intertwined with another effect which

and the typical photometric uncertainties at the faint end of the catalogue are larger than this average effect.

3.3.2 Comparison with UltraVISTA

We perform a second, external consistency check of our photometry comparing it with the already mentioned UltraVISTA catalogue, which was observed in the same band (Muzzin et al. 2013). The data we compare correspond to the overlap between ALHAMBRA-4 and the UltraVISTA COSMOS field. As we discussed in Section 2.4, the total overlapping area is $\sim 0.21\mathrm{deg}^2$ and the number of sources in common is 9,579.

In the top panel of Figure 3.4 we show the results of the comparison of the K_s-band magnitudes for the objects in the common sample. As UltraVISTA is deeper than ALHAMBRA we can check our photometry all the way down to the ALHAMBRA K_s magnitude limit.

Selecting only bright targets ($15.5 < K_s < 19$) to avoid the larger photometric uncertainties at the faint end, we can confirm an excellent agreement between both datasets. The bottom panel of Figure 3.4 proves this result: we find a systematic difference of 0.02 magnitudes—which is, in fact, comparable with the calibration uncertainty of the UltraVISTA data compared to the COSMOS catalogues and 2MASS (McCracken et al. 2012). For the fainter sample the scatter between both datasets becomes larger, but remains always within the typical photometric uncertainties of both catalogues.

3.4 Photometric redshift accuracy

Once we have tested the correctness of the photometry performed on our images we can proceed to check the quality of the photometric redshifts, which are one of the key ingredients of our catalogue. As we did in the previous section for the photometry, we will perform two separate tests: an external one, comparing our

pushes in the opposite direction: in general, the apertures that we use are, by definition, better suited to measure the K_s-band flux, which is thus expected to be slightly larger in our measurement. This effect tends to be more noticeable for the faintest objects.

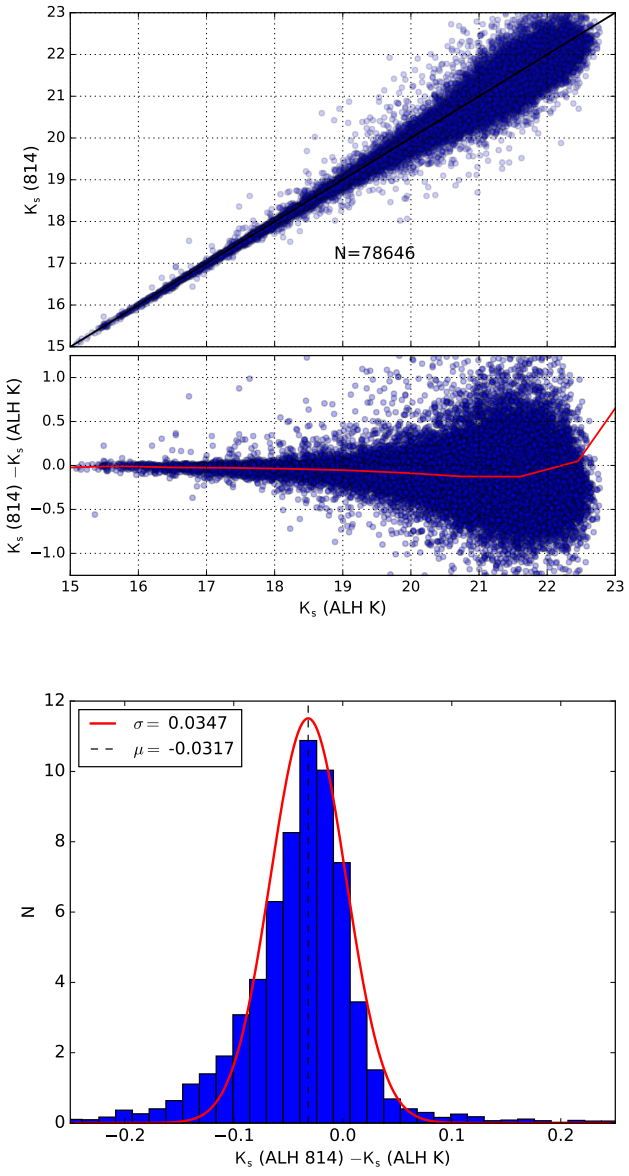

Figure 3.3: The top panel shows the ALHAMBRA F814W-band catalogue and ALHAMBRA K_s-band catalogue photometry comparison. The bottom panel shows the distribution of K_s magnitude differences for the bright sample (15< K_s <19), over-plotted with its Gaussian best fit, whose parameters are given in the inset.

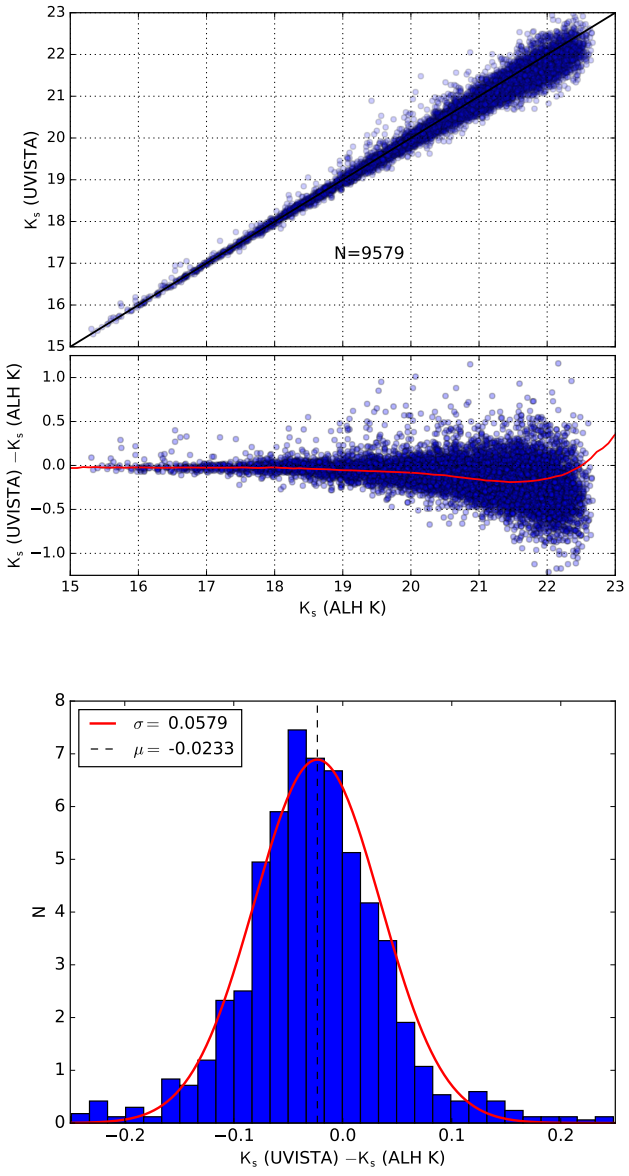

Figure 3.4: Top panel: UltraVISTA and ALHAMBRA K_s-band catalogue photometry comparison for the ALHAMBRA-4 COSMOS field. Bottom: Distribution of magnitude differences for the bright sample ($15< K_s <19$), over-plotted with its Gaussian best fit whose parameters are given in the inset.

photometric redshifts with those compiled from spectroscopic catalogues covering the same areas, and an internal one, comparing our results with the ones originally published in M14, whose quality was already assessed in that work.

In what follows we will use, in order to assess the quality of the photometric redshifts, the normalised median absolute deviation $\sigma_{\rm NMAD}$, as defined in Ilbert et al. (2006):

$$\sigma_{\rm NMAD} = 1.48 \times {\rm median}\left(\frac{|\delta z - {\rm median}(\delta z)|}{1+z_s}\right), \tag{3.4.1}$$

where $z_{\rm s}$ is the spectroscopic redshift and $\delta z = (z_{\rm s} - z_{\rm b})$ is the difference between the spectroscopic and the Bayesian photometric values. This parameter allows an accurate estimate of the rms for a Gaussian distribution and is less sensitive to outliers than the standard deviation. We will define the outlier rate (fraction of catastrophic errors) using two different criteria as in M14: η_1 is the fraction of sources that verify $\frac{|\delta z|}{1+z_{\rm s}} > 0.2$ and η_2 represents the fraction of sources that verify $\frac{|\delta z|}{1+z_{\rm s}} > 5 \times \sigma_{\rm NMAD}$.

One of the features of BPZ (Benítez 2000) is that it can be forced to use the information in a spectroscopic redshift sample to re-calibrate photometric zero points in each band. To do this the program compares the observed photometry with the one that would be expected of the galaxy templates at the known (spectroscopic) redshift for each object. If this comparison shows a significant zero-point bias in a given filter, this value is added to all the magnitudes in that filter and the whole process is iterated. Molino et al. (2014) discussed in detail this photometric redshift-based zero-point re-calibration. We have used this feature for our K_s-band catalogue, finding very small corrections (median absolute deviation per filter ≈ 0.02 mags), and a small but noticeable improvement in the quality of the photometric redshifts.

3.4.1 Spectroscopic redshift comparison

We have repeatedly mentioned that one of the advantages of the ALHAMBRA Survey is the overlap with other well-known fields. This allowed M14 to compile a sample of 7144 galaxies with spectroscopic redshifts from public databases. We have identified the objects in this spectroscopic sample within our catalogue in order to compare the spectroscopic redshifts, $z_{\rm s}$ with the Bayesian photometric

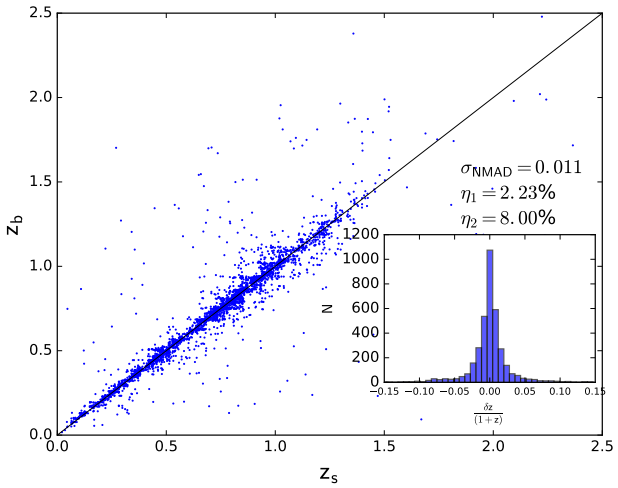

Figure 3.5: ALHAMBRA K_s photometric redshift $z_{\rm b}$ vs. spectroscopic redshift $z_{\rm s}$ for 3736 sources. The inset shows the distribution of the deviations $\delta_z/(1+z)$. The measured scatter is $\sigma_{\rm NMAD} = 0.011$, with catastrophic error rates $\eta_1 \sim 2.3\%, \eta_2 \sim 8.0\%$.

redshifts estimated in this work, $z_{\rm b}$.

We show in Figure 3.5 the result of the comparison of the photometric redshifts and the spectroscopic sample, which in our case includes 3736 sources. We obtain a dispersion $\sigma_{\rm NMAD} = 0.011$[3] for the total sample, and a catastrophic error rate $\eta_1 \sim 2.3\%$. Both figures are similar to the ones obtained by M14 for their F814W ≤ 22.3 sample.

As we have mentioned in Section 2.6, among the output of the BPZ code we get for each object a Bayesian *Odds* parameter, which measures the affidability of the measured photometric redshift (Benítez 2000). We thus expect that both the dispersion $\sigma_{\rm NMAD}$ and the outlier rate parameters η_1 and η_2 should decrease when samples with increasingly large *Odds* values are selected. This effect is clearly shown in Figure 3.6: all the quality indicators ($\sigma_{\rm NMAD}, \eta_1, \eta_2$) consistently improve when we impose a lower limit on the *Odds* parameter (top panel), at the

[3]The figure was $\sigma_{\rm NMAD} = 0.015$ before the zero-point recalibration performed with the spectroscopic redshift sample, as explained in the previous paragraph.

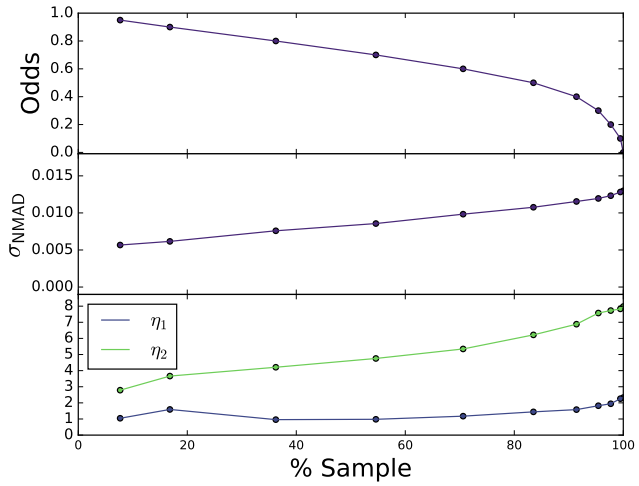

Figure 3.6: Effect of the selection of sub-samples based on the *Odds* parameter. Top panel:Evolution of the *Odds* parameter with sample size. Middle panel: Evolution of the photometric redshift accuracy $\sigma_{\rm NMAD}$ with sample size, thresholded by *Odds* values. Bottom panel: Outlier rate parameters η_1 and η_2 as a function of sample size.

obvious price of a decreasing sample size. In the extreme case, when only objects with *Odds*> 0.95 are selected, the scatter falls to $\sigma_{\rm NMAD} = 0.005$, but the sample size is less than 10% of the original.

3.4.2 ALHAMBRA F814W catalogue photometric redshift comparison

As shown in the previous section, the number of sources with spectroscopic information is scarce. In order to compile a larger sample with which our results can be compared, we have used the ALHAMBRA photometric redshifts calculated in M14 for the F814W-based catalogue. It is obvious that we are, after all, using the same imaging data for the same sources (those which are common to both catalogues), so we should necessarily reach similar results. However, we see this test as a necessary trial of the detection, aperture definition, and photometry processes we have performed.

In order to create a pseudo-spectroscopic sample, where the systematic effects

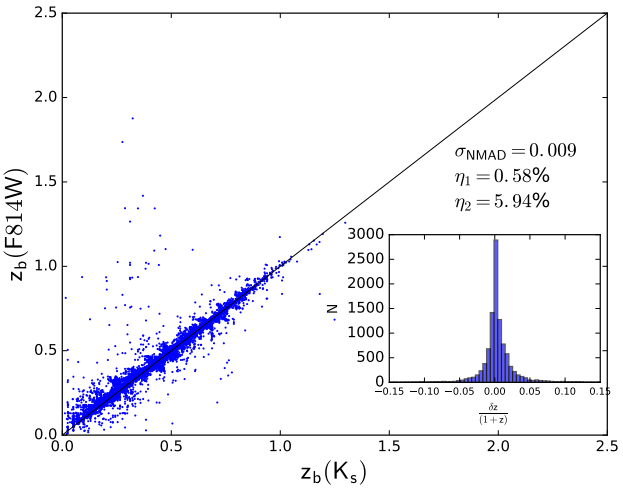

Figure 3.7: M14 photometric redshift $z_{\rm b}$(F814W) vs. K_s-band photometric redshift $z_{\rm b}(K_s)$ for 10,251 common sources. The inset shows the distribution of $\delta_z/(1+z)$. The small concentration of outliers at $z_{\rm b}(K_s) \sim 0.3$ is due to the colour degeneracy between low-redshift red galaxies and moderate-redshift bluer ones.

will not be dominated by the photometric uncertainties, we have selected sources with magnitudes $K_s < 19.5$ and $I_{814} < 21$. From this sample we have excluded objects identified as stars in any of the two catalogues. This sample includes 10251 sources.

Comparing the photometric redshifts in M14 and in this work we obtain a scatter $\sigma_{\rm NMAD} = 0.009$, and catastrophic error rates $\eta_1 \sim 0.58\%$ and $\eta_2 \sim 5.94\%$ (see Figure 3.7). As expected, the comparison between our catalogue and the ALHAMBRA F814W sample yields results that are much better than the spectroscopic comparison, even though the number of sources included in the analysis is larger.

After this final check we are satisfied that our catalogue can be scientifically exploited. Figure 3.8 shows the photometry and best fit results for three example objects, which cover a wide range in photometric redshift, best-fitting spectral type and K_s magnitude.

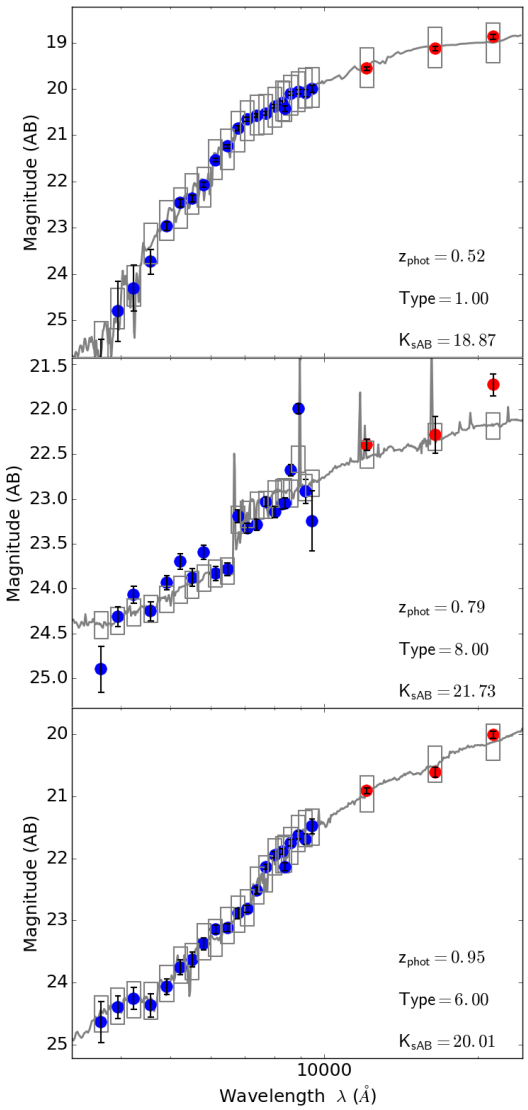

Figure 3.8: Three examples of spectral fits to the ALHAMBRA data of different galaxies. Redshifts range from 0.5 to 1, SEDs from $T_B = 1$ (elliptical) to $T_B = 8$ (starburst), and K_s-band magnitudes from ~ 19 to ~ 22. On each plot the grey line is the spectrum corresponding to the best fit, as indicated in the inset text, and the grey rectangles are the model photometry in the 23+1 ALHAMBRA bands (we include the synthetic F814W image flux). We use blue (red) markers for the optical (near infrared) spectral range.

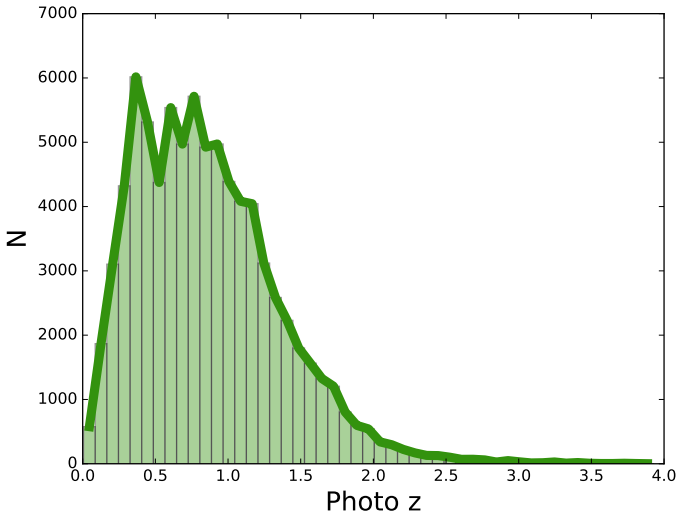

Figure 3.9: Histogram of BPZ best-fitting photometric redshifts for a total of 81,873 galaxies.

3.5 Photometric redshift distribution

After checking the quality of our catalogue regarding photometry and redshifts, and once we are satisfied that the number count distribution is correct, we can move on to the exploitation of the catalogue. The most basic functions to analyse include the individual and multivariate redshift-magnitude-spectral type distributions.

In what follows we have cleaned our galaxy sample using the `COLOR_CLASS_STAR` parameter to avoid stars, leaving us with a catalogue of 81,873 galaxies. We show the histogram of best-fitting photometric redshifts for this sample in Figure 3.9. The median redshift is $\langle z \rangle = 0.80$, and the values of the first and third quartiles of the redshift distribution are $z_{\rm Q1} = 0.47$, $z_{\rm Q3} = 1.15$.

The top panel of Figure 3.10 shows a contour plot of the redshift-apparent magnitude plane. We have overplotted on it as a red line the evolution of the mean redshift as a function of the K_s magnitude. In the bottom panel of the same figure we present an alternative view of the same distribution, in this case showing the redshift distribution of galaxies for different apparent magnitude cuts. This plot

shows very clearly that any increase in K_s-band depth represents a corresponding increase in redshift depth, as we expected from the colour-magnitude diagrams analysed in previous sections. The tail of the distribution towards high redshift is populated with intrinsically red objects, most of them showing very red ($I_{814W} - K_s$) colours and in most cases absent from the general-purpose ALHAMBRA catalogue presented in M14. We will check this statement in the next section.

3.5.1 Redshift distribution of galaxy types

We will now focus on the analysis of the distribution of galaxy types in the catalogue. As was mentioned in the Introduction, the ALHAMBRA F814W catalogue shows a dearth of early type galaxies at redshifts $z \gtrsim 1.1$, which is induced by the passage of the 4000 Å break and associated absorption at such redshift through the F814W filter, the one used for source detection by M14.

We will compare the redshift/SED distribution obtained by M14 (F814W-selected) with the one we have obtained with our catalogue selected in the K_s-band. This comparison will allow us to check whether we are, in fact, recovering those early-type galaxies at z$\gtrsim$ 1.1.

Figure 3.11 shows in the top panel the photometric redshift distribution of galaxies in the K_s (solid line) and F814W (dashed line) catalogues. As the NIR sample is shallower we have applied a cut in the original ALHAMBRA catalogue ($I_{814} < 23.5$), and to render both curves directly comparable we have multiplied the NIR distribution by a factor 1.44, so that the areas under both curves are the same. There is a hint of structure in both lines over the range $0.3 < z < 0.8$, which can be due to the large-scale structure which is obviously common to both catalogues.

It is remarkable that, even though the K_s-band selected sample presented here is less deep than the original ALHAMBRA catalogue, its tail extending to high redshift is clearly more noticeable. This is exactly what we expect from the recovery of $z \gtrsim 1$ early-type galaxies. To confirm this point we have measured the fraction of early-type galaxies (defined as those with $1 \leq T_B \leq 5.5$) at each redshift. This fraction is plotted in the lower panel of Figure 3.11. The increase in the fraction of early-type galaxies is significant already at low redshift ($\approx 35\%$ at $z < 1$ in the NIR sample, compared to $\approx 20\%$ in the F814W case). But the effect is much stronger at higher redshifts—the fraction of early-type galaxies decreases

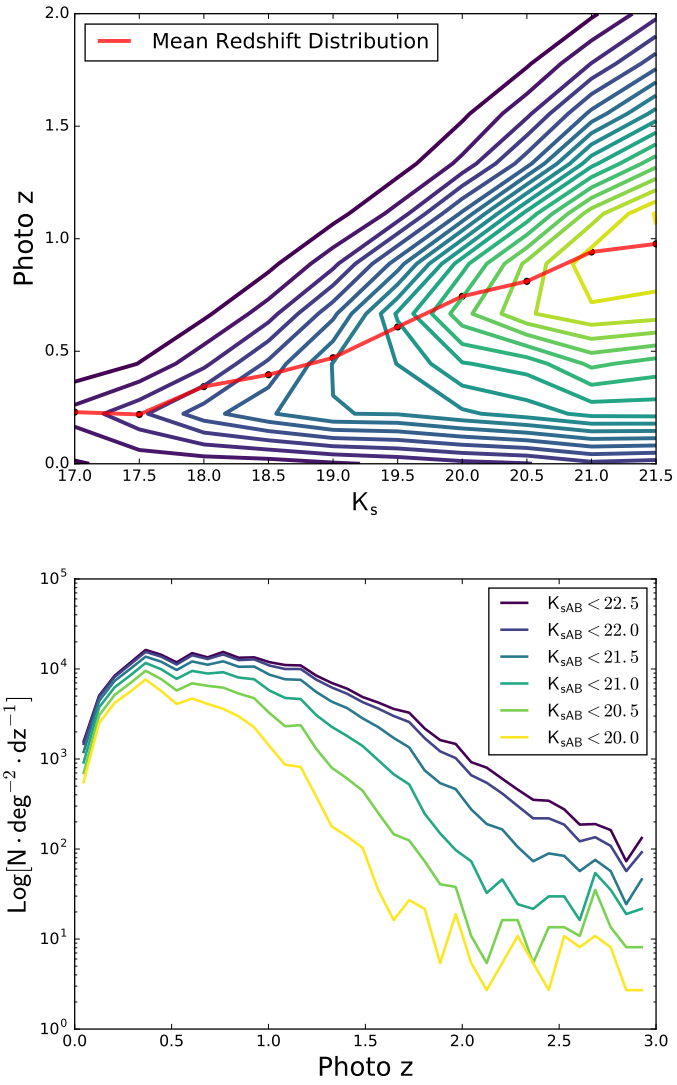

Figure 3.10: Top: Density contour plot in the redshift-K_s magnitude plane. The solid red line shows the evolution of the mean photometric redshift as a function of magnitude. Bottom: Redshift distribution of galaxies in our catalogue, selected in successive K_s magnitude cuts.

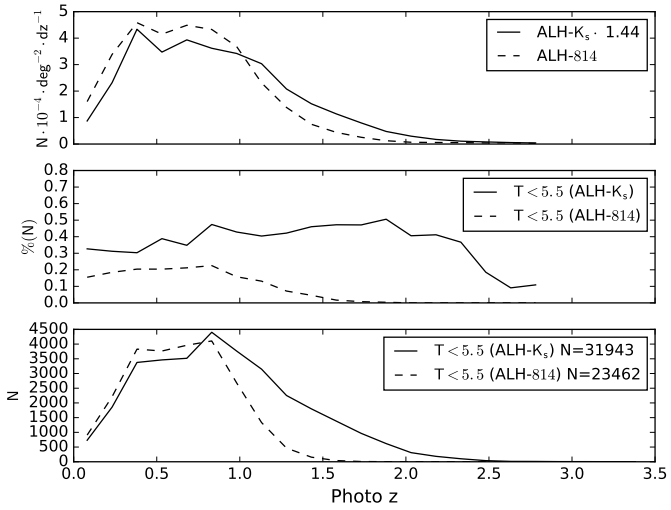

Figure 3.11: Top: Photometric redshift distribution for the K_s-selected (solid line) and F814W-selected (dashed line) samples. Centre: Fraction of galaxies in both samples whose best-fitting templates are $1 < T_B < 5.5$, which we identify as early-type SEDs. Bottom: Absolute number of early-type sources at each redshift in each catalogue.

to reach almost zero at redshift $z \approx 1.5$ in the ALHAMBRA M14 catalogue, whereas we still observe a sizeable fraction of early types ($\approx 40 - 50\%$) out to the highest redshifts accesible to our catalogue ($z \approx 2.5$). We show the same fact, this time using absolute numbers from both catalogues, in the bottom panel.

3.6 A test of the IRAC cross-match

As we have shown in the previous sections, the ALHAMBRA survey overlaps with fields that have been extensively studied by other projects. This will allow us to benefit from ancillary information added to our catalogue, as was the case with the spectroscopic sample.

One of the most interesting additions for the particular aims addressed in this work is the possibility of extending the photometry further into the infrared range, using public catalogues provided by different teams. Although for some of our targets and objectives we will also benefit from data from the all-sky WISE

Survey (Wright et al. 2010) and the *Spitzer* MIPS instrument, we will concentrate here only in the data from the *Spitzer Space Telescope* Infra-Red Array Camera (IRAC, Fazio et al. 2004). Images taken with this instrument will add photometric data in four new bands, centered at 3.6, 4.5, 5.8, and 8.0 μm.

There are several public fields where deep IRAC data have been taken and analysed. The extra information provided by these images will be crucial for some of our targets: we must keep in mind that the main objective of our work is to detect and analyse objects with very red intrinsic $(I_{814} - K_s)$ colours, which in some cases implies that we will only have solid detections of their flux in the JHK_s filters, combined with strong limits on their flux in the visible range. The extension to the $3 - 8\,\mu$m wavelength range provided by IRAC means that we will be able to observe a much wider rest-frame spectral window, including the characteristic potential downturn in the flux of early-type galaxies at wavelengths $\lambda > 2.5\,\mu$m in the rest frame.

As a test in this first stage we have cross-matched our ALHAMBRA-7 field catalogue (ELAIS-N1, Rowan-Robinson et al. 1999) with the public data of the *Spitzer* Wide-area Infrared Extragalactic Survey (SWIRE, Lonsdale et al. 2003). Over 75% (11,756/15,262) of our ALHAMBRA-7 K_s-selected sources have counterparts in the IRAC database. We have plotted the SEDs of some of these galaxies in Figure 3.12, covering a wide range of galaxy types (top to bottom) and redshifts (left to right). A glance at this figure is enough to show the complementarity between the ALHAMBRA visible and NIR data and the extension allowed by the IRAC available observations.

Within this ALHAMBRA-7 sample we have found a significant number of galaxies with extremely red colours, that render them observable in ALHAMBRA only in the JHK_s filters. For these objects the IRAC data becomes crucial to allow for a robust characterization. We have detected in IRAC 225 of 246 such sources, all with colour $(I_{814} - K_s) > 4$. In Figure 3.13 we show in the top panel our best fit for one such galaxy, whereas the bottom panel shows how the fit changes and the results improve when the IRAC data are added. In the next section we will give some figures about the sample of this kind of objects that we can extract from our catalogue. Galaxies of this kind are interesting by themselves, and deserve a more detailed analysis which will be the target on Chapter 4.

Other fields with similarly deep IRAC data include ALHAMBRA-2 (DEEP2),

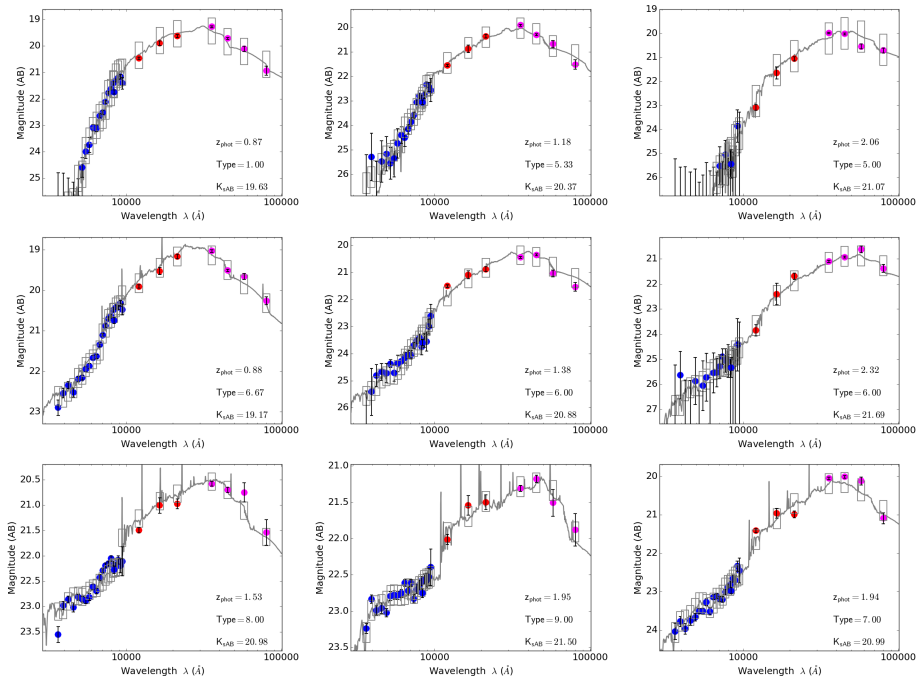

Figure 3.12: Example ALHAMBRA+IRAC pseudo-spectra and best fits for a sample of galaxies. The top (medium, bottom) row shows spectral data corresponding to early-type (late-type, star-forming) SEDs, and in each case the redshift grows from left to right. In all panels the blue markers correspond to ALHAMBRA data in the visible range, red to ALHAMBRA JHK_s, and magenta to *Spitzer* IRAC data.

ALHAMBRA-4 (COSMOS), and ALHAMBRA-6 (GROTH). A full description and analysis of the merging of our catalogue with this dataset will be the object of Chapter 4.

3.7 Extremely red objects

As discussed in the previous section, the ALHAMBRA K_s-band catalogue includes a significant number of sources typically classified as Extremely Red Objects (EROs, Elston et al. 1988). These objects are usually selected according to their very red colours (for example $(I-K) > 4$), and classified using both their visible and NIR colours as, for example, in the BzK selection technique (Daddi

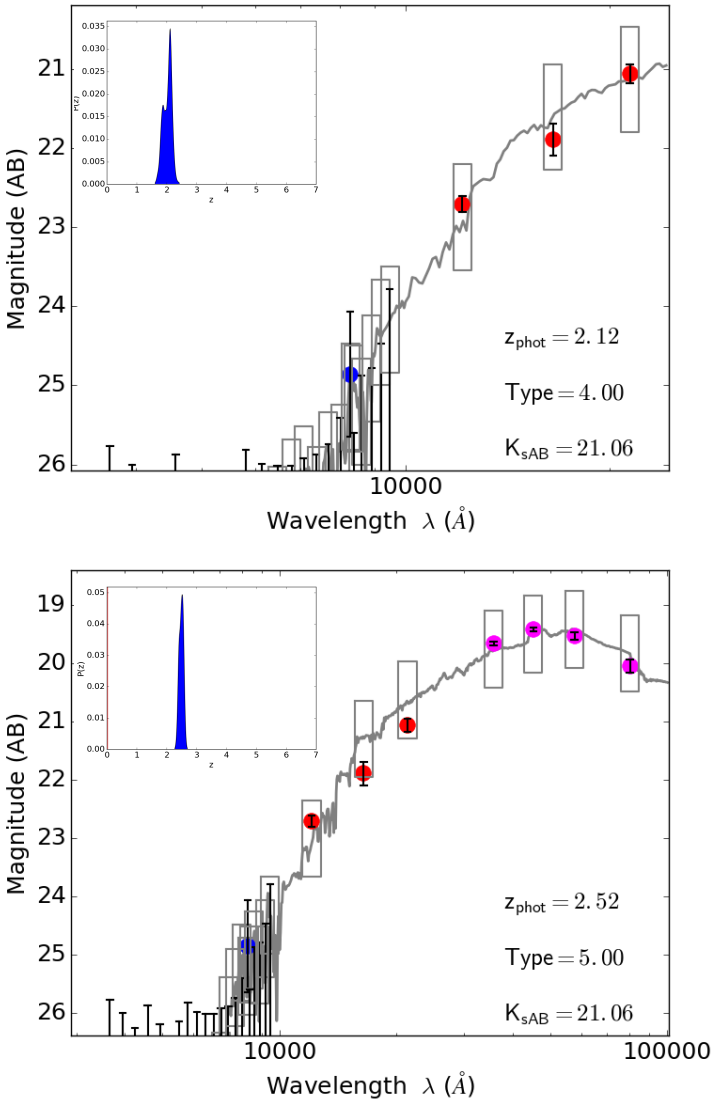

Figure 3.13: Pseudospectrum and best-fitting SED of an Extremely Red Object from our catalogue. The top panel shows the fit obtained using the ALHAMBRA 20+3 filter data set. The bottom panel shows the result of the analysis of the same object, once the IRAC data are added. In each case the inset panel shows the Bayesian redshift probability function $p(z)$.

$(I_{814} - K_s)$	N	z_{1Q}	z_{med}	z_{3Q}
All	31943	0.54	0.85	1.19
>1	30815	0.59	0.87	1.20
>2	18278	0.93	1.14	1.43
>3	7503	1.32	1.49	1.71
>4	1539	1.75	1.89	2.06
>5	408	1.95	2.11	2.27

Table 3.2: Characteristics of the redshift distribution of samples of objects characterised by early-type SEDs ($T_B < 5.5$) and different $(I_{814} - K_s)$ colour thresholds.

et al. 2004). Most of the EROs can be classified either as passively evolving or as dusty star-forming galaxies (Cimatti et al. 2002).

We can use our very deep synthetic F814W image, combined with the K_s-band images used for galaxy detection in our catalogue, to select EROs based on different $(I_{814} - K_s)$ thresholds. As was indicated above, these cuts in $(I_{814} - K_s)$, induce an almost one-to-one selection in redshift for galaxies characterised by early-type SEDs. This is clearly seen in Figure 3.14, where the redshift distributions of galaxies with $T_B < 5.5$ are plotted for different threshold values of $(I_{814} - K_s)$. We list in Table 3.2 the sizes and values of the first quartile, median, and third quartile redshifts of those samples. Taking a reference value for the threshold selection of $(I_{814} - K_s) > 4$ the total number of such ERO candidates in our catalogue is 1539.

The colours of most of the galaxies in these ERO samples fit those of old, massive, passively evolving galaxies [4]. These galaxies are one of the key steps in galaxy evolution, and the study of their properties is essential for the understanding of the early phases of the evolution of elliptical galaxies.

We show the distribution of K_s absolute magnitudes for the sample of early-type galaxies in Figure 3.15, where it is clear that the vast majority of them lie within the redshift interval $1.5 < z < 2.5$, reaching luminosities as high as

[4]We must remark, however, that BPZ does not fit the dust content as a separate parameter, but includes the effect of fixed amounts of dust within the templates themselves. Because of this, objects with a very high dust content may not be correctly identified in our catalogue.

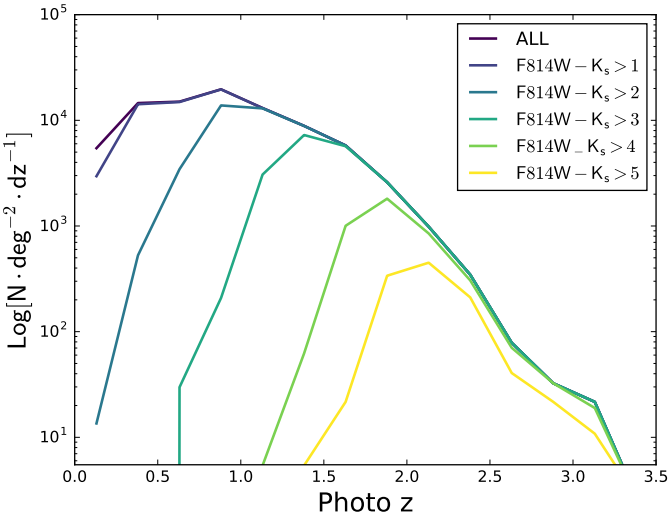

Figure 3.14: Distribution of photometric redshifts for different $(I_{814} - K_s)$ colour-selected samples, for galaxies with $T_B < 5.5$.

$M_K \approx -24.5$. We have used the stellar population analysis code MUFFIT (Díaz-García et al. 2015), which allows for the separation of two different populations (young and old) and includes dust extinction as a free parameter, to explore in more detail the properties of this sample. Results from this analysis will be presented in a future manuscript.

3.8 Galaxy clustering of early-type galaxies in the K_s-band catalogue

One of the main aims of astronomical surveys is to describe the distribution of galaxies over significant cosmological volumes. Such analysis allows us to obtain information about the large-scale structure (LSS) of the Universe and how it relates to the galaxy formation and evolution processes. As we have described in Chapter 1, we will use the two-point correlation function $\xi(r)$ as our choice statistical tool to obtain information about the galaxy distribution.

As we have mentioned in Section 1.5.2, the measurement of the two-point cor-

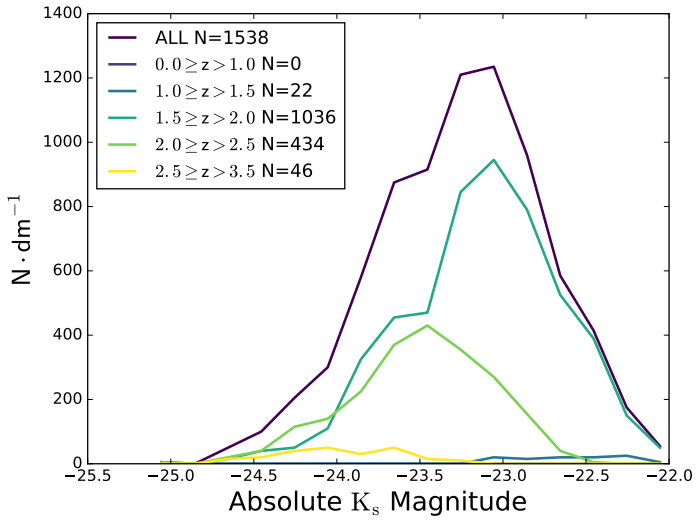

Figure 3.15: Distribution of the K_s absolute magnitudes in our catalogue for galaxies with $(I_{814} - K_s) > 4$ and $T_B < 5.5$, in different redshift ranges.

relation function in real space can be strongly affected by two different effects: The first one is the loss of the isotropy due to the peculiar velocities of galaxies: i) in the random motion inside virialised structures and ii) in the coherent infall of galaxies into big structures. Another effect is due to the use of photometric redshift techniques: the uncertainties that photometric errors induce in the measurement of distances along the line of sight become dominant in the measurement of the real-space correlation function. In order to obtain reliable measurements it is necessary to take all these effects into account. Therefore we need a method that enables the recovering of the real-space correlation function avoiding them. We present in Section 3.8.2 the method described by Arnalte-Mur et al. (2009) for the recovering of the real-space correlation function.

One of the most relevant results of the analysis of the spatial clustering of observable galaxies is that the density field of the matter does not necessarily trace the galaxy distribution in a one-to-one manner. In a simple case, it is possible to relate both distributions using a *bias* which is defined as the ratio of the over-density of the observed galaxies to the over-density of the matter

density field. The study of *bias* provides important information to understand the processes involved in galaxy formation and evolution. The *bias* depends on some galaxy properties such as the epoch of galaxy formation, the luminosity and the morphology.

In this context, one can consider that the behaviour of the *bias* parameter will be different for the different galaxy populations. This effect is known as galaxy segregation, and it describes how red, massive elliptical galaxies are more highly clustered than blue, less massive spiral galaxies. In terms of *bias*, ellipticals have a larger *bias* than spirals (Davis & Geller 1976; Dressler 1980). In this section we will study the K_s-band correlation function for the red galaxy sample, extending the study made for the ALHAMBRA optical catalogue in Arnalte-Mur et al. (2014) and Hurtado-Gil et al. (2016). In this section absolute magnitudes are given as $M - 5\log_{10}(h)$.

3.8.1 Sample selection

The main goal of this part of our work is to measure the correlation function using the data included in the K_s-band catalogue for the red type sample. We first describe how we have defined this sample, including the redshift and luminosity thresholds of the different subsamples.

We have defined subsamples from the ALHAMBRA K_s-band catalogue in a similar way as was done in Arnalte-Mur et al. (2014). The sky area over which the galaxies are selected is defined by the masks described in Section 2.3. We have considered the best-fit BPZ output galaxy type T_B parameter to select red galaxy types, i.e. values in the $1 < T_B < 5.5$ range. From those we have selected galaxies with $Odds > 0.15$, to ensure a sample of good quality photometric redshifts: the analysis performed above and shown in Figure 3.6 indicates that we will have $\sigma_{\mathrm{NMAD}} \sim 0.012$ for this sample.

Stars have been removed from the catalogue using the star/galaxy parameter estimated using the method explained in Section 2.5. As it is shown in Figure 2.4, each ALHAMBRA CCD has different magnitude limits: to avoid any significant variation in the different fields and to perform a study which is as homogeneous as possible, we restrict the galaxies in our sample to AB magnitudes $K_s < 21.0$. Under these restrictions we will be performing our clustering analyses over a sample of 13702 galaxies, covering an effective area $\mathrm{A_{eff}} = 2.463$ deg^2 with an

average of $\sim 5.6 \cdot 10^3$ deg^{-2}.

To study the evolution and luminosity dependence of the clustering of red galaxies we will split the sample in bins, both in redshift and in absolute magnitude. The line-of-sight size of our redshift bins has to be significatively larger than the distance we will integrate over the line of sight direction in order to avoid systematic uncertainties due to border effects (Arnalte-Mur et al. 2009). This leads us to define three redshift bins: $0.75 < z < 1.05$, $0.95 < z < 1.2$ and $1.15 < z < 1.45$. The overlapping of consecutive redshift bins helps us to perform the statistical analysis of the correlation function with larger number of galaxies in a more significant volume, but the obvious price is that we will have to take in account in our results the correlations effects due to the overlapping of the redshift bins. The lowest redshift limit has been selected in order to compare with the results obtained in Hurtado-Gil et al. (2016) and extend them to higher redshift. The highest redshift limit is given by the need of the sample to have sufficient density to provide a good determination of the clustering parameters.

The split in B-band absolute magnitude M_B has been chosen to define subsamples that keep the galaxy number density as close to constant as possible. We have selected the B-band because its rest-frame wavelength is well covered by the ALHAMBRA filters in the redshift range considered in this work. Moreover, it has also been used in other works with which we will be able to compare our results. Following Meneux et al. (2009) we define the absolute magnitude thresholds in the B-band $M_B^{th}(z)$ as

$$M_B^{th}(z) = M_B^{th}(0) + Az_p. \tag{3.8.2}$$

where A is a constant selected to produce subsamples with a similar number density. In this work A =0.8. The linear dependence with the redshift allows to study the evolution of the subsamples using galaxy population that can be meaningfully compared. We show in Figure 3.16 the different regions used for the study. We include in Table 3.3 the median redshift z_{med}, the median B-band absolute magnitude M_B^{med}, and the median luminosity L^{med} in terms of $L^\star$ for each subsample. The $L^\star(z)$ used in this work has been obtained from the study performed for the ALHAMBRA optical catalogue in López-Sanjuan et al. (2015). We also include the typical error of the photo-z $\sigma_z/(1+z)$ and the typical radial distance error $r(\sigma_z)$.

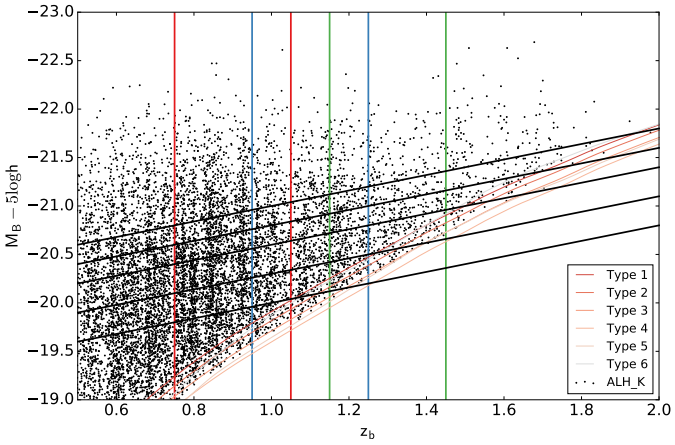

Figure 3.16: Selection of the different galaxy samples for the study of the evolution of the clustering for the early-type galaxies selected from the K_s-band catalogue. The lines show the redshift boundaries of the samples (vertical lines), and their B-band absolute magnitude limits (oblique lines). Red curves mark the B-band apparent magnitude selection limit for the different red-type galaxy templates included in BPZ.

Sample	Redshift range	N^{red}	$M_B^{th}(0)$	z_{med}	M_B^{med}	$L_{med}/L^{\star red}(z)$	$\sigma_z/(1+z)$	$r(\sigma_z)$ Mpc h^{-1}
z09_M19p2	$0.75 < z < 1.05$	3083	-19.2	0.864	-21.46	0.5492	0.0084	28.6
z09_M19p5	$0.75 < z < 1.05$	2338	-19.5	0.863	-21.64	0.6504	0.0077	26.32
z09_M19p8	$0.75 < z < 1.05$	1619	-19.8	0.864	-21.83	0.7883	0.0069	23.59
z09_M20p0	$0.75 < z < 1.05$	1159	-20	0.864	-21.99	0.9118	0.0064	21.81
z09_M20p2	$0.75 < z < 1.05$	825	-20.2	0.860	-22.13	1.0357	0.0061	20.86
z11_M19p5	$0.95 < z < 1.25$	1303	-19.5	1.089	-21.77	0.6285	0.0127	42.32
z11_M19p8	$0.95 < z < 1.25$	878	-19.8	1.088	-21.96	0.7487	0.0114	38.16
z11_M20p0	$0.95 < z < 1.25$	619	-20	1.090	-22.11	0.8647	0.0104	34.83
z11_M20p2	$0.95 < z < 1.25$	405	-20.2	1.089	-22.26	0.9793	0.0099	32.94
z13_M19p8	$1.15 < z < 1.45$	515	-19.8	1.254	-22.08	0.742	0.0172	56.39
z13_M20p0	$1.15 < z < 1.45$	356	-20	1.249	-22.22	0.8454	0.0158	51.87
z13_M20p2	$1.15 < z < 1.45$	226	-20.2	1.250	-22.37	1.0026	0.0147	48.26

Table 3.3: Characteristics of the redshift/luminosity subsamples. For each subsample we list the redshift range, number of objects N^{red}, B-band absolute magnitude threshold in the rest frame $M_B^{th}(0)$, median redshift z_{med}, median B-band absolute magnitude, median luminosity L_{med} as a function of $L^{\star red}(z)$, redshift error $\sigma_z/(1+z)$ and the distance error $r(\sigma_z)$ expressed in Mpc h^{-1}.

3.8.2 Recovering of the real-space correlation function

In order to recover the real-space correlation function we follow the method described by Davis & Peebles (1983). This method consists in trying to reach a projection of the two point correlation function, through use of the two-dimensional correlation function $\xi(r_p, \pi)$. In this section we will denote as r_p the component of the distance between two galaxies transverse to the line of sight, and π the one in the direction which is parallel to the line of sight. We define the projected correlation function as

$$w(r_p) \equiv 2 \int_0^\infty \xi(r_p, \pi) d\pi. \tag{3.8.3}$$

In order to obtain a measurement of $\xi(r_p, \pi)$ we use the estimator proposed by Landy & Szalay (1993). To do that an auxiliary random-Poisson catalogue was generated for each galaxy sample, which reproduces the same properties of the sample selected from the ALHAMBRA K_s-catalogue for this study in terms of the distribution on the masked sky and in the distribution as a function of redshift.

For each subsample we computed the distribution of pair galaxy separations in terms of (r_p, π), in all cases for the number of pairs of galaxies in the galaxy sample (denoted as DD), the number of pairs of simulated galaxies in the random-Poisson catalogue (denoted by RR) and the number of crossed pairs between both catalogues (denoted by DR). The correlation function is then estimated as

$$\widehat{\xi}_{LS}(r_p, \pi) = 1 + \left(\frac{N_R}{N_D}\right)^2 \frac{DD(r_p, \pi)}{RR(r_p, \pi)} - 2\frac{N_R}{N_D}\frac{DR(r_p, \pi)}{RR(r, \pi)} \tag{3.8.4}$$

where N_R and N_D are the number of galaxies in the random-Poisson catalogue and in the ALHAMBRA K_s-catalogue respectively. For the measurement of the correlation function performed in this work we followed the recommendations in Anderson et al. (2014), from where $N_R = 20N_D$.

When performing the calculation of the integral 3.8.3 with the real data set it is not possible to estimate the integral out to infinity. Setting a finite upper limit becomes necessary, and it must be large enough to include all the relevant survey data, but always keeping in mind that too large a limit will introduce too much additional noise in our calculations. Taking into account the typical redshift errors of the ALHAMBRA K_s-band catalogue (see Section 3.4) and following a

similar path to the one used by Arnalte-Mur et al. (2014), we fixed the value to $\pi_{\rm max} = 200$ Mpc h^{-1}. Taking this change into account Equation 3.8.3 can be rewritten as

$$w_p(r_p, \pi_{\rm max}) \equiv 2 \int_0^{\pi_{\rm max}} \xi(r_p, \pi) d\pi. \tag{3.8.5}$$

When measuring the correlation function $w_p(r_p)$ in a finite volume it is necessary to introduce in our calculations the integral constraint term (Peebles 1980). This term corrects the bias due to the fact that we are estimating the mean galaxy density and the correlation function from the same data set. Bernardeau et al. (2002) and Labatie et al. (2010) showed that the bias introduced in the correlation function in a finite volume V takes the form

$$\xi(r) = \xi^{\rm true}(r) - K, \tag{3.8.6}$$

being

$$K \equiv \frac{1}{V^2} \int_V \int_V d^3 r \xi^{\rm true}(r). \tag{3.8.7}$$

If we translate the integral constraint in terms of the projected correlation function and then in terms of $\pi_{\rm max}$, we finally obtain for Equation 3.8.5:

$$w_p(r_p, \pi_{\rm max}) = w_p(r_p, \pi_{\rm max})^{\rm true}(r) - 2K\pi_{\rm max} \tag{3.8.8}$$

A full analysis of the method leading to the recovery of the real space correlation function and a test of the method in the case of the (general) ALHAMBRA Survey can be found in Arnalte-Mur et al. (2014). We have followed the same steps for the analysis presented hereafter.

3.8.3 Modelling of the correlation function and results

In order to describe the two-point correlation function over a large range of scales, a power-law model is widely used to parameterise the real-space correlation function $\xi(r)$ (e.g. Hawkins et al. (2003); Coil et al. (2006)). We assume that at large scales, $\xi(r)$ can be expressed as

$$\xi^{\rm pl}(r) = \left(\frac{r}{r_0} \right). \tag{3.8.9}$$

We can apply this relation to the projected correlation function $w(r_p)$ in terms of the parameters r_0 and γ, using equation 3.8.3, to obtain

$$w_p^{\rm pl}(r_p) = r_p \left(\frac{r_0}{r_p}\right)^{\gamma} \frac{\Gamma(1/2)\Gamma[(\gamma-1)/2]}{\Gamma(\gamma/2)} \tag{3.8.10}$$

where Γ is Euler's Gamma function. From this power-law fit it is possible to recover the parameters r_0 and γ for the real correlation function ξ. As we have mentioned in Section 3.8.2, the use of finite volumes in the analysis introduces a bias term in the projected correlation function measurements, given by the integral constrain.

Taking this into account and following Equation 3.8.8 we can finally rewrite the projected correlation function model as

$$w_p^{\rm model}(r_p|r_0,\gamma) = w_p^{\rm pl}(r_p|r_0,\gamma) - 2K(r_0,\gamma)\pi_{\rm max} \tag{3.8.11}$$

where the term $w_p^{\rm pl}(r_p|r_0,\gamma)$ is the projected correlation function expressed in Equation 3.8.10.

The integral constrain term $K(r_0,\gamma)$ is calculated following Roche et al. (1999). Equation 3.8.7 needs a value for the real two-point correlation function in order to calculate the integral constraint. To obtain an approximate estimate of this value we fitted the parameters of the model using data included in an auxiliary Poisson catalogue. The value of the integral 3.8.7 was computed numerically using the estimator Landy & Szalay (1993) (Equation 3.8.4) as

$$K \simeq \frac{\sum_i RR(r_i)\xi^{\rm model}(r_i)}{\sum_i RR(r_i)} = \frac{\sum_i RR(r_i)\xi^{\rm model}}{N_R(N_R-1)} \tag{3.8.12}$$

where the sums are computed for each bin as defined in Section 3.8.1.

3.8.4 Results and discussion

We present in this section the results obtained for the correlation function and a brief discussion of our results.

In Figure 3.17 we show the results we obtain for the measurement of the projected correlation function for the different redshift and B-band absolute magnitude limits, as defined in Table 3.3. The error-bars were obtained using a jackknife method (Norberg et al. 2009), in a similar way as was done in Hurtado-Gil et al.

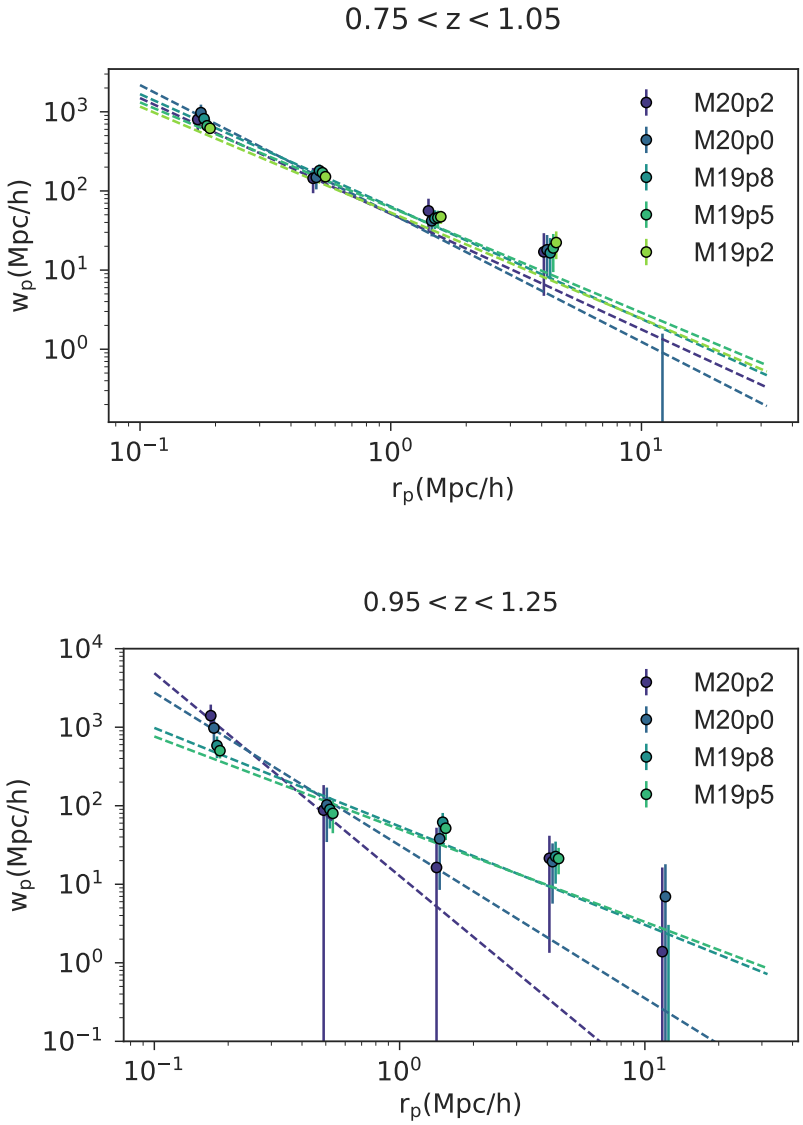

Figure 3.17: Projected two-point correlation functions $w_p(r_p)$ of red-type galaxies in the ALHAMBRA K_s-band catalogue for different B-band luminosity samples. Each panel corresponds to a different redshift range, as labelled. Dashed lines show the best-fit power-law models as in Equation 3.8.11.

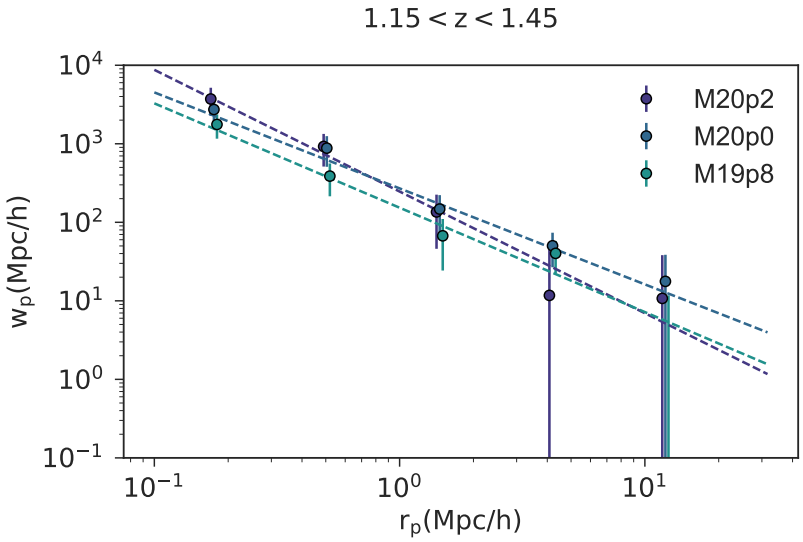

Figure 3.17: (Continued) Projected two-point correlation functions $w_p(r_p)$ of red-type galaxies in the ALHAMBRA K_s-band catalogue for different B-band luminosity samples. Each panel corresponds to a different redshift range, as labelled. Dashed lines show the best-fit power-law models as in Equation 3.8.11.

(2016). The results of the best-fit of the projected correlation function power-law models $w_p^{\rm model}(r_p)$, are shown as dashed lines.

We observe some interesting features in the measured correlation functions. Over the range of scales probed in this work, i.e. from $r_p \sim 0.15\,{\rm Mpc}\,h^{-1}$ to $r_p \sim 12\,{\rm Mpc}\,h^{-1}$, the correlation functions for all our samples are well fitted by a power-law. There is a hint of a possible break towards a larger slope at scales $r \lesssim 1$ Mpc h^{-1}, which was also detected in Hurtado-Gil et al. (2016). At this stage we cannot delve on the significance of this possible break, which will be object of a deeper analysis in the future.

Some evolution in redshift is detectable, particularly at the higher redshift end and for the more luminous samples. From our calculations we observe that, in general, galaxies at higher redshift are more clustered. Regarding a possible luminosity segregation, only in the $z \in [1.15, 1.45]$ range it is clearly noticeable: faint galaxies are less clustered than luminous ones. All these results are in agreement with previous analyses presented in Hurtado-Gil et al. (2016), who analysed the segregated clustering of galaxies in the general purpose, I_{814}-band selected ALHAMBRA catalogue. Our work extends theirs by allowing us to measure a larger sample of red galaxies out to higher redshifts.

In order to quantify the possible clustering evolution we have also analysed the best-fit model values of the parameters r_0 and γ, listed in Table 3.4. We show in Figure 3.18 those results for each redshift bin, as a function of the median B-band luminosity expressed in terms of the reference luminosity $L^\star(z)$ in each bin. We also include in both panels the results obtained for the red-type galaxies at similar redshift in Hurtado-Gil et al. (2016). On the top panel of Figure 3.18, we plot the results for the r_0 parameter. We appreciate in this plot the abovementioned evolution in redshift, particularly the difference between the highest redshift case and the other two.

It is important to underline that the points from the previous analysis by Hurtado-Gil et al. (2016), which correspond to the clustering of red galaxies at lower luminosities at the two lower redshift ranges in our comparison, fit the luminosity trends in all cases. This reinforces our idea that we can extend their results to higher redshift in an homogeneous way.

We must insist in the well-known fact that the values of r_0 and γ are very highly (anti-)correlated, which means that the apparent change of both parameters with

Sample	$r_0(\mathrm{Mpc}\,h^{-1})$	γ
z09_M19p2	3.65±0.66	2.34±0.19
z09_M19p5	3.90±0.62	2.33±0.17
z09_M19p8	3.82±0.68	2.42±0.19
z09_M20p0	3.29±0.61	2.62±0.24
z09_M20p2	3.45±0.94	2.46±0.32
z11_M19p5	3.76±1.13	2.18±0.31
z11_M19p8	3.80±1.10	2.25±0.35
z11_M20p0	2.53±0.70	2.95 ±0.39
z11_M20p2	1.75±0.63	3.58 ±0.64
z13_M19p8	5.77±1.00	2.33±0.17
z13_M20p0	7.89±0.86	2.22±0.10
z13_M20p2	6.21±0.76	2.55±0.10

Table 3.4: Values and confidence limits of the best-fit parameters r_0 and γ in equation 3.8.11 calculated for each redshift and luminosity subsample.

luminosity that is observed at intermediate redshift (green line in both panels) may actually approximately cancel out, yielding similar power-law fits, as is in fact seen in Figure 3.17 (central panel). This change may in fact be pointing once more at a change in the clustering scale, and not in its intensity.

It is important to emphasise that due to the overlapping between the redshift ranges the correlation effects between subsamples become important in our study, rendering any difference among contiguous redshift bins less noticeable. A more complete analysis of the observed evolution of the clustering with redshift and luminosity will have to take this into account. It should also include an analysis of the bias associated to the different subsamples and its possible change with time. Such an analysis, which has already been performed in part, will be presented as a future manuscript.

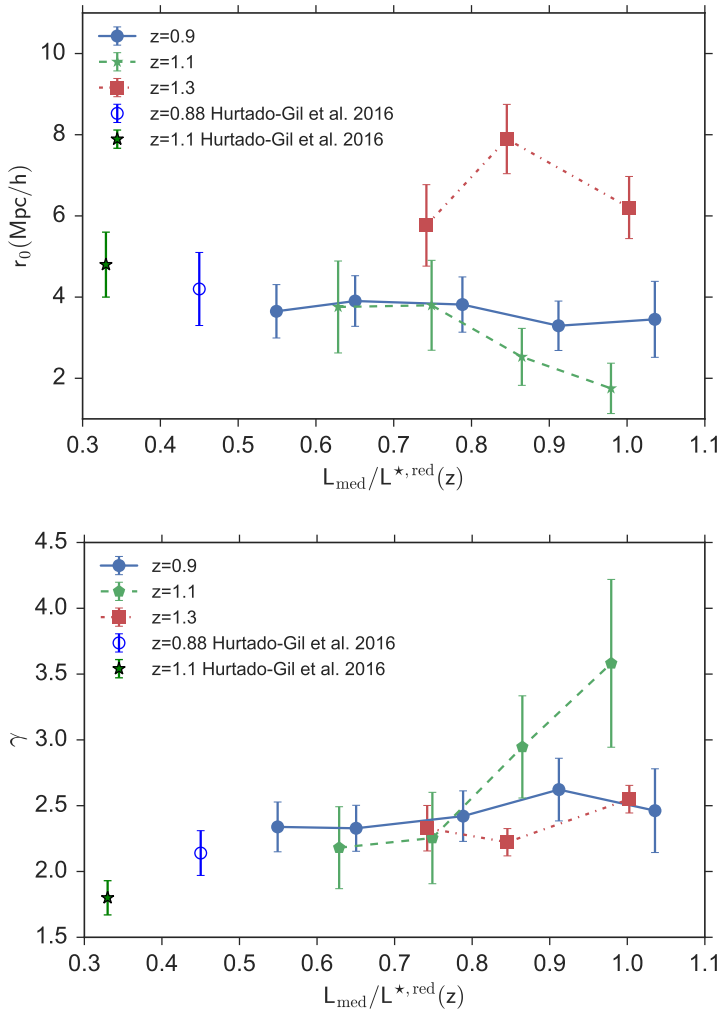

Figure 3.18: Best-fit values for the r_0 (top panel) and γ (bottom panel)parameters as a function of the median luminosity of the rest-frame B-band, calculated for each redshift bin.

Chapter 4

IRAC cross-match catalogue and Luminosity Function

As we have introduced in Section 3.6, one of the main benefits of the ALHAMBRA project is the fact that the observed fields have been chosen to overlap with other well-studied areas in the sky. All the ALHAMBRA fields have been observed and analysed by other astronomical surveys, opening a range of possibilities, for example, to extend the available photometry into other wavelengths.

One of the most interesting spectral ranges to extend the photometry in the case of our K_s-selected catalogue is that of redder infrared wavelengths. This range is specially useful to characterise the new set of galaxies detected in the K_s-band, not included in the optical ALHAMBRA catalogue. These sources usually only show a significant flux in a few filters, if any, within the optical bands, and they are relatively bright in the JHK_s range. When we add other infrared (IR) bands, we expect to improve the photometric redshift values computed for the ALHAMBRA K_s-band catalogue, obtaining at the same time a better characterisation of these galaxies. Other benefit added when we include photometry in these bands is the possibility to observe a wider redshifted spectral window, including the characteristic potential downturn in the flux of early-type galaxies at wavelengths $\lambda > 2.5\mu$m in the rest frame.

We present in this chapter the ALHAMBRA K_s-band cross-match catalogue (AK_s-IR),including data from the *Spitzer Space Telescope* Infra-Red Array Cam-

era (IRAC, Fazio et al. 2004). Images provided by this instrument will add photometric data in four new bands, centered at 3.6, 4.5, 5.8, and 8.0μm. In all cases we will be including data from public surveys, and in all cases we will be working with source catalogues, as opposed to the original IRAC images. This means, on one side, a simplification of our task, as we will not need to work on the data reduction but will directly take object lists and photometry as published by the different teams. On the other hand we will need to analyse in detail the level of agreement of the data obtained from the different surveys with the photometry in our data, checking for different possible effects. Analogously to the work we performed in the case of the K_s-band sample, we will compute BPZ2.0 photometric redshifts using our AK_s-IR catalogue. We will also test the accuracy of the photometric redshifts, comparing the results obtained for the galaxies in the AK_s-IR catalogue with their spectroscopic redshift counterparts and with our previous 23-band results.

We finish this chapter with the presentation of the rest-frame K_s-band luminosity function (KLF) computed for the K_s-IR catalogue in a similar way as in the optical B-band LF (López-Sanjuan et al. 2017). As was already discussed in Chapter 1 the luminosity function (LF) is a powerful statistical tool that provides information about the formation and evolution of galaxies. Studying the evolution of the LF in the NIR results particularly useful because observations of the galaxy emission in the rest-frame in this spectrum range are less affected by dust absorption and recent star formation episodes, which renders it an excellent stellar mass tracer (e.g. Lilly & Longair 1984; Dunlop et al. 1989; Cowie et al. 1996). Our AK_s-IR catalogue provides a complete and well defined sample of galaxies to obtain an accurate measurement of the luminosity function in the rest-frame K_s band. In this chapter all magnitudes are given in the AB system (Oke & Gunn 1983).

4.1 ALHAMBRA K_s + IRAC catalogue: AK_s-IR

As we already mentioned in the introduction to this chapter, the ALHAMBRA survey fields were selected in order to overlap with other areas covered by other surveys in different wavelengths. This overlapping enables us to extend the photometric coverage to other bands. We have thus created a new catalogue starting

from our sample selected in the K_s-band, including data from the *Spitzer Space Telescope* Infra-Red Array Camera (IRAC, Fazio et al. 2004), on the infrared bands centered at 3.6, 4.5, 5.8, and 8.0 μm. In this section we describe the process that we follow to compile the IRAC public data, and method to perform the cross-match of those catalogues with ALHAMBRA K_s sample.

In order to search for the overlapping area between our ALHAMBRA Survey fields and the available data covered by the different IRAC fields (see Figure 4.1) we have used the application RADAR. This tool is included in the Infrared Science Archive (IRSA) website[1]. We introduce in each case the central coordinates of the region of interest, together with a given field size. RADAR outputs a complete list with the existing infrared data sets included in the IRSA archive. In the particular case of theALHAMBRA fields, we proceed to input the central coordinates for each field (see coordinates in Table 3.1) with a radius of search large enough to cover the whole field area. We found IRAC surveys which share coverage with ours for the fields ALHAMBRA-2, ALHAMBRA-4, ALHAMBRA-6 and ALHAMBRA-7:

- ALHAMBRA-2: IRAC counterpart included in the Spitzer Enhanced Imaging Products (SEIP) (Strasburger et al. 2015). The SEIP provides a list of highly reliable sources extracted from the Spitzer images, called Source List (SL).
- ALHAMBRA-4: we have used the data from the COSMOS Spitzer (S-COSMOS) survey (Sanders et al. 2007).
- ALHAMBRA-6: IRAC counterpart from the Extended Groth Strip (EGS) catalogue (Barmby et al. 2008).
- ALHAMBRA-7: IRAC counterpart in the Spitzer Wide-area Infrared Extragalactic Survey SWIRE, data from the ELAIS-N1 field (Lonsdale et al. 2003).

All the catalogues used for the cross-match data, provide aperture fluxes for different aperture sizes, together with their corresponding errors. According to

[1] `http://irsa.ipac.caltech.edu/applications/Radar/`

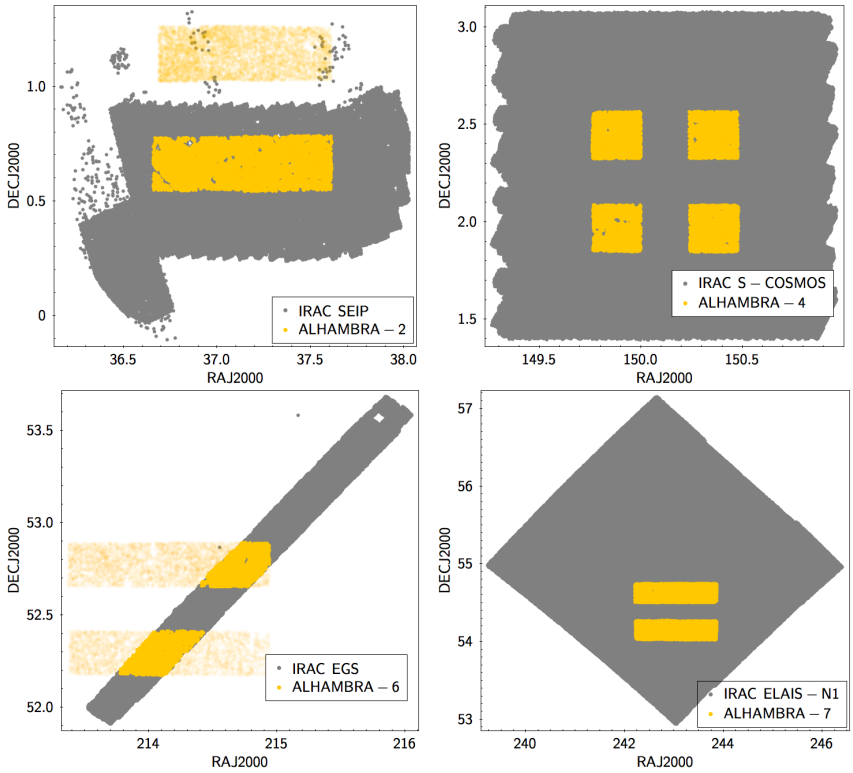

Figure 4.1: ALHAMBRA & IRAC overlapping area. Grey regions correspond the area covered by IRAC, whereas the ALHAMBRA covered area is given by the yellow marks. The region in dark yellow is the overlapping area.

the recommendations found in the manual for each individual survey, and also from other similar works (e.g. Barro et al. (2011); Muzzin et al. (2013)), the best aperture size for an accurate IRAC photometry is `Flux aperture`$\sim$2". The accuracy of this selection will be one of the objects for the tests we will describe along this section.

One step further in the building of the catalogue is to define the overlapping area of the surveys. This is an important part of the survey development, as the survey area masks will play an important role in (among others) the determination of the luminosity functions or the clustering properties. Following the same method previously used for the K_s-band catalogue (see Section 2.3), we have designed new angular masks to reliably estimate the detection area. We have included a column flag in the K_s-band catalogue to indicate whether the source is or not in the common area. In Table 4.1 we list the overlapping area for each ALHAMBRA fields. The total area once all four ALHAMBRA fields are summed is 0.93 deg^2.

We then performed the cross-match between the catalogues using the TOPCAT software (Taylor 2005). TOPCAT provides a specific tool (*Match Table*) to perform cross-matching of catalogues. This tool allows to select different criteria to how objects in the corresponding catalogues are paired. At this point it is important to mention that both the SEIP source list catalogue and the SWIRE ELAIS-N catalogues include also photometry in the JHK bands. In those cases, we have performed the cross-match using the `Match Table` option "`Sky+X`". When this option is used TOPCAT selects the best matching objects considering not only the sky coordinates but also a third component. In this case, to improve the match in the catalogues, we require the matched objects to have the same sky position (within a given cross-match offset allowance) and K_s-magnitude. In the case of the S-COSMOS and EGS catalogues we have selected the option "`Sky`", that only requires the sky coordinates as input for the cross-match. In order to make an estimate about the number of possible miss-matches in the cross-match process, we compared the results for the number of matches obtained using both methods, "`Sky+X`" and "`sky`", for the ELAIS-N1 field. The number of sources with multiple matches in the allowed radius is very small (less than $\sim 0.04\%$), so we conclude that the cross-match radius offset selected to perform this work is a good compromise to seek a balance between obtaining a maximum of matches,

Table 4.1: Basic properties of the ALHAMBRA K_s + IRAC catalogue. In the first column we show the name of ALHAMBRA field and IRAC catalogue counterpart. The second column is the selected cross-match radio and the third column is the number of cross-matched sources. In the next two columns we include the values of the overlapping area for each ALHAMBRA field and the number of sources included in each cross-matched catalogue.

Cross-Match Field	Cross-Match radio	Cross-Match sources	Overlapping area deg^2	Number of $K-band$ sources
ALHAMBRA-2 & SEIP	1.2"	7085	0.2064 deg^2	7574
ALHAMBRA-4 & S-COSMOS	1.2"	8232	0.2063 deg^2	9587
ALHAMBRA-6 & EGS	1.0"	3348	0.1012 deg^2	3601
ALHAMBRA-7 & ELAIS-N1	1.0"	11717	0.4133 deg^2	15262
	TOTAL	30382	0.9272 deg^2	36024

and avoiding miss-matching in the samples. The cross-match radii selected in each field are listed in Table 4.1.

85% of the sources in our K_s-band selected catalogue have counterparts in the IRAC data. In the case of objects in the ALHAMBRA-K_s catalogue for which no counterpart is found in the corresponding IRAC catalogues we use the detection limits corresponding to each band and survey to define the magnitude limits that will be given in the catalogue. It is important to remark at this point that in the calculation of the photometric redshifts there is an important difference between having no data and having a maximum flux limit—particularly a stringent one, as is the case of the IRAC catalogues we are using.

After this process is complete we obtain a catalogue of sources selected in the K_s-band over an area of almost one degree squared, for which we have 23+1 optical+NIR bands from ALHAMBRA plus the photometry in the IRAC four infrared bands centered in 3.6, 4.5, 5.8, and 8.0 μm.

4.1.1 AK_s-IR catalogue photometry test

We perform a first test of the photometry included in our catalogue in order to check the validity of our approach when defining the merged catalogues. In order to have a manageable sample we only consider the sources in the ALHAMBRA-7+IRAC overlapping area, i.e. ~ 0.41 deg^2. To this aim we have used the data included in the SWIRE-N1 catalogue (Lonsdale et al. 2003). We first compare their photometry with the photometry performed on the same data by Barro et al. (2011), who performed a full reduction and photometric analysis.

Figures included in the panels of 4.2 show the comparison of both photometries. We observe a good agreement between both samples for the IRAC channel 1 (3.6 μm), channel 2 (4.5 μm), and channel 3 (5.8 μm). However, we notice a larger scatter in IRAC channel 4 (8.0 μm). The small offset observed in the comparison in channels 1, 2 and 3 could be attributed to differences in the data reduction or the use of different aperture corrections. The observed scatter in those three bands grows in the faint end, but remains within typical photometric uncertainties.

Colour-colour diagrams

The previous test is a first proof of the quality of our photometry, but it is available only for a fraction of our data. It is necessary to check all IRAC data included in our catalogue, and we also want to test their consistency with the ALHAMBRA K_s-band catalogue photometry.

In order to have an external test of the data quality we have performed colour-colour diagrams using the IRAC channels. We will compare the position of the catalogued galaxies in these diagrams with the redshift tracks of galaxies that form the BPZ galaxy template set. In this manner we will be able to test the concordance between the photometry in the IRAC channels and the ALHAMBRA K_S-band photometry. Another issue that can be directly observed in these plots is the dispersion due to the noise characteristics, and whether it matches the expectations from the catalogue.

As a first test that should allow us to check the agreement of the data that straddle the transition between the ALHAMBRA and IRAC data we show in the top panel of Figure 4.3 the (K_s - IRAC$_{ch1}$) colour versus (IRAC$_{ch1}$-IRAC$_{ch2}$) for

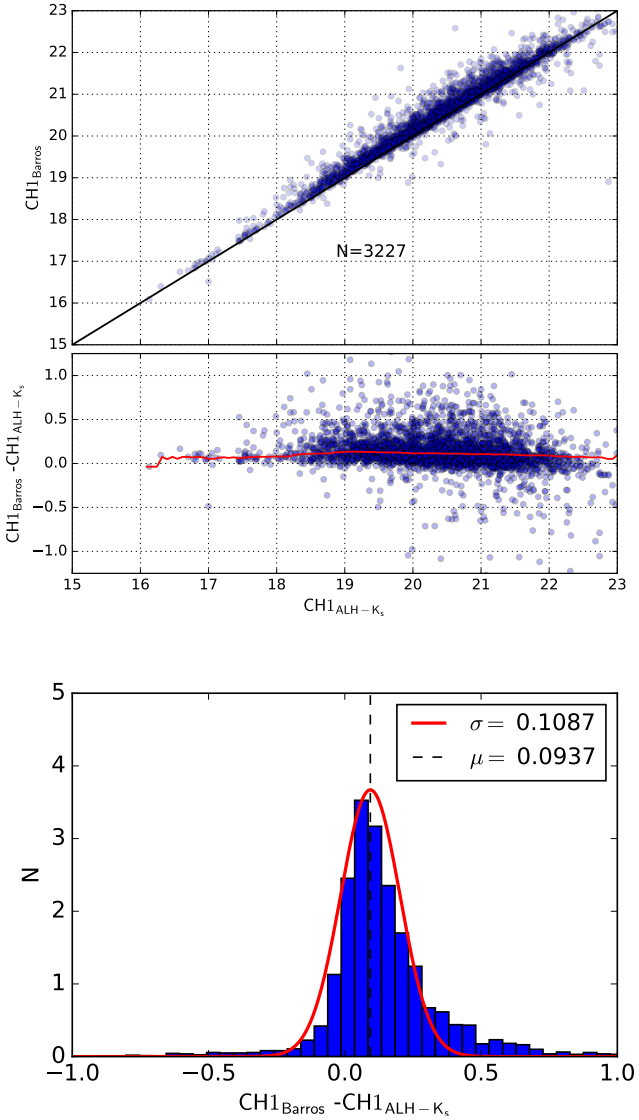

Figure 4.2: IRAC channel 1 photometry comparison for the common sources in the AK_s-IR and the Barro et al. (2011) Extended Groth Strip catalogue. Top panel shows the photometry comparison for each channel, with the red line marking the running average. Bottom panel shows the distribution of the differences for a bright subsample ($16 < IRAC_{CH} < 20$), together with the Gaussian best fit whose parameter values are given in the plot legend.

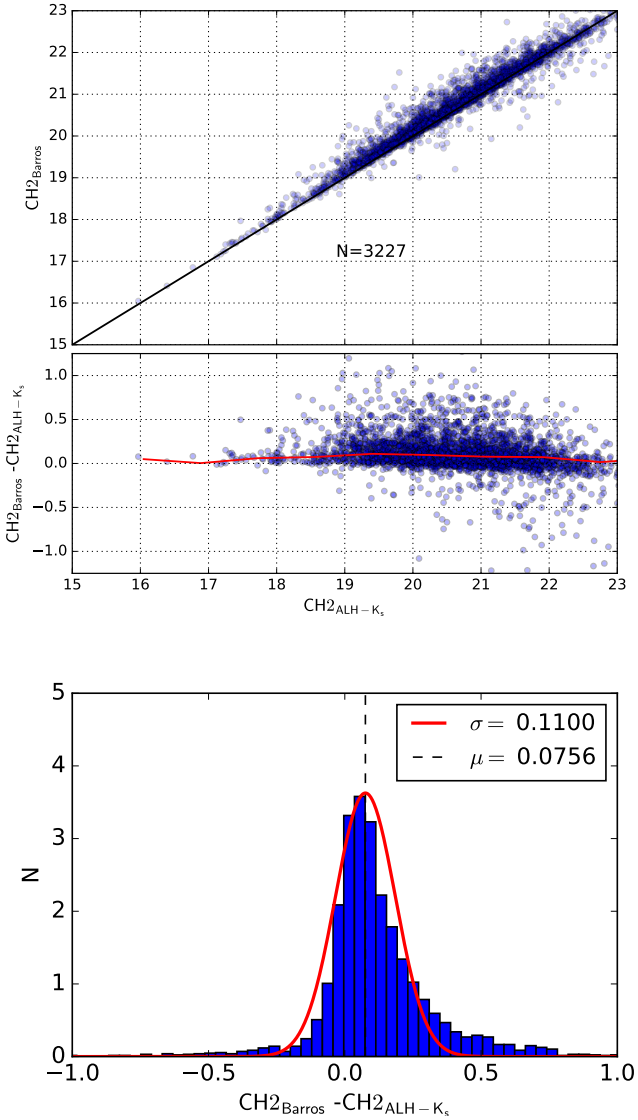

Figure 4.2: (continued) IRAC channel 2 photometry comparison for the common sources in the AK_s-IR and the Barro et al. (2011) Extended Groth Strip catalogue. Top panel shows the photometry comparison for each channel, with the red line marking the running average. Bottom panel shows the distribution of the differences for a bright subsample ($16 < IRAC_{CH} < 20$), together with the Gaussian best fit whose parameter values are given in the plot legend.

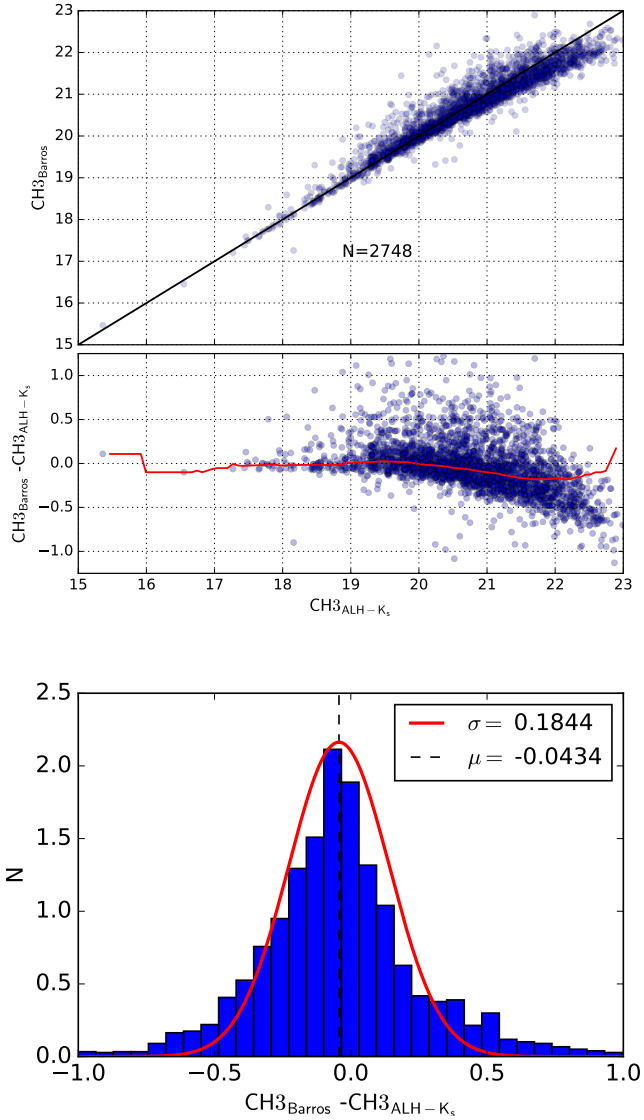

Figure 4.2: (continued)IRAC channel 3 photometry comparison for the common sources in the AK_s-IR and the Barro et al. (2011) Extended Groth Strip catalogue. Top panel shows the photometry comparison for each channel, with the red line marking the running average. Bottom panel shows the distribution of the differences for a bright subsample ($16 < IRAC_{CH} < 20$), together with the Gaussian best fit whose parameter values are given in the plot legend.

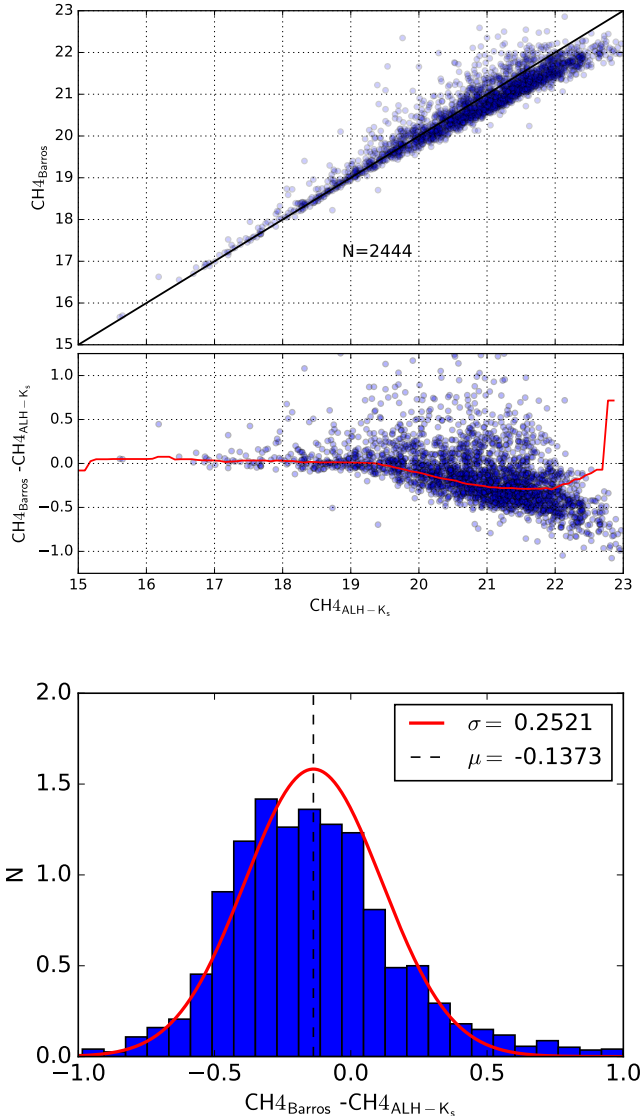

Figure 4.2: (continued)IRAC channel 4 photometry comparison for the common sources in the AK_s-IR and the Barro et al. (2011) Extended Groth Strip catalogue. Top panel shows the photometry comparison for each channel, with the red line marking the running average. Bottom panel shows the distribution of the differences for a bright subsample ($16 < IRAC_{CH} < 20$), together with the Gaussian best fit whose parameter values are given in the plot legend.

all the sources included in the catalogue, together with the tracks corresponding to template galaxies at different redshifts. We do not observe any offset in the sample, and the positions of the points are in reasonable agreement with the redshifted template tracks. We conclude that the photometry of the different IRAC channels is consistent with that of the K_s-band.

In the bottom left panel of Figure 4.3 we show the ($F814W$ - K_s) vs (K_s - IRAC$_{ch1}$) colour-colour diagram. In this case data from the four different fields are plotted using different colours. By doing this we can check that all the fields share very approximately the same loci within the plot. We thus conclude that our photometric measurements do not suffer from strong field-to-field dependences.

Finally the bottom right panel of Figure 4.3 shows a new colour-colour diagram which only involves three IRAC bands, (IRAC$_{ch1}$-IRAC$_{ch2}$) vs (IRAC$_{ch2}$-IRAC$_{ch3}$). Looking at this figure shows a more noticeable scatter, particularly along the horizontal direction. This is to be expected, as we have seen in the last two panels of Figure 4.2 above that the photometric uncertainties of the reddest filters (IRAC$_{ch3}$ and, specially, IRAC$_{ch4}$) are largest. We can check again, however, that there is no offset between data from different fields.

The results obtained in this series of analyses lead us to conclude that the photometry of the IRAC channels 1, 2 and 3 is in good agreement with our ALHAMBRA K_s-band photometry in all fields, and that there are no significant offsets between the different fields—which is particularly important since we will be merging data from four different and independent IRAC projects. On the other hand there is a significant difference regarding the quality of the IRAC$_{ch4}$ data, with a much larger scatter which can indeed be at least partly explained by the lower signal-to-noise of the involved images.

In order to study the effects of the dispersion found in the channel 4 in our future analyses we performed a preliminary run using BPZ2.0. In Figure 4.4 we represent the photometric redshifts obtained when comparing the AK_s-IR versus the spectroscopic redshift. In the top panel we show the results we obtain including the IRAC$_{ch4}$ photometry, whereas in the bottom panel we show the results of the same analysis when we omit the IRAC$_{ch4}$ photometry. The plot insets include the corresponding values of the dispersion σ_{NMAD} and the outlier rate η_1 for both samples.

The result of this analysis, combined with the previous results regarding the

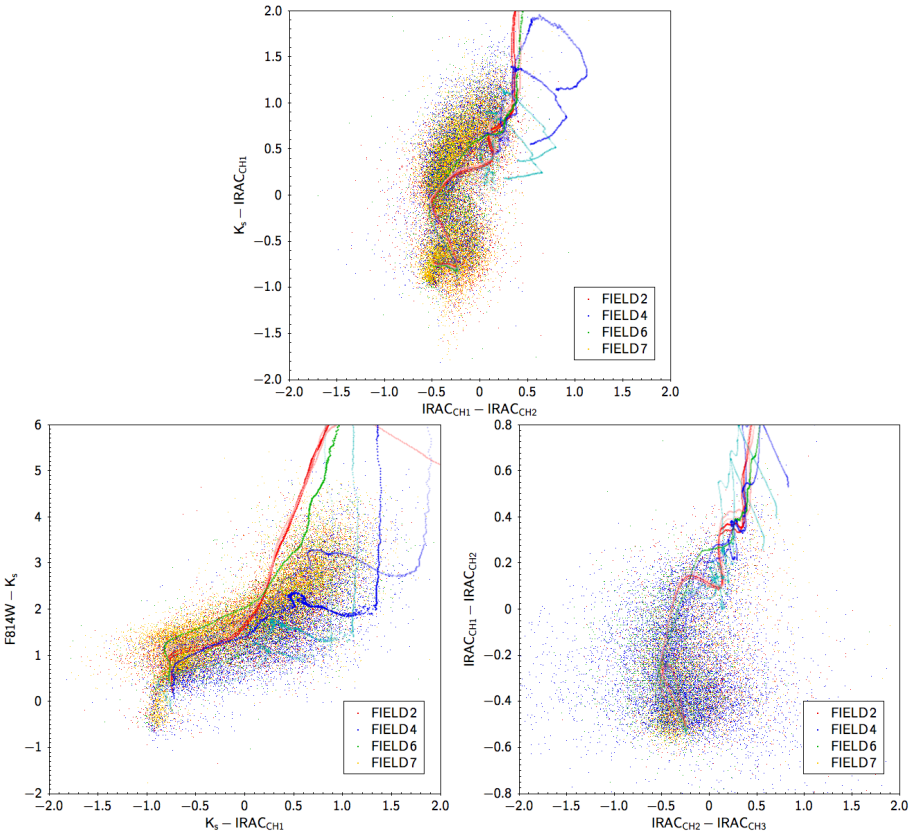

Figure 4.3: Top: Colour-colour diagram using the IRAC channels 1 ($IRAC_{ch1}$) and 2 ($IRAC_{ch2}$) together with the K_s-band photometry from the ALHAMBRA K_s-band selected catalogue for the ALHAMBRA-2 Field. The lines are the BPZ galaxy template redshifted in range $z \in [0, 12]$. Bottom: Colour colour diagrams corresponding to different combinations of ALHAMBRA and IRAC filters.

quality of the IRAC$_{ch4}$ photometry, shows us that we can clearly improve the accuracy of our photometric redshifts when the IRAC$_{ch4}$ data are removed. This led us to the decision of not to including this channel in the final catalogue. We must remark that we have found in the literature other works that have exclude the IRAC$_{ch3}$ and IRAC$_{ch4}$ from their analyses, as for example Galametz et al. (2013); Yang et al. (2014).

4.1.2 Cross-matched catalogue photometric redshifts

In the same way that we have done with the ALHAMBRA K_s-band selected catalogue, we have obtained photometric redshifts using (BPZ2.0, Benítez 2000, Benítez in preparation) for our AK_s-IR cross-matched catalogue.

Our final cross-matched catalogue thus includes, for the ALHAMBRA K_s-band selected objects: photometry in the ALHAMBRA 20+3 filters, the synthetic F814W filter, and the 3 selected IRAC channels, plus the data that are obtained as BPZ2.0 output. As before, some of the important measurements are the Bayesian photometric redshift z_b, the associated SED best-fitting type T_B, and the *Odds* parameter.

Following a similar process to that already explained for the ALHAMBRA-K_s catalogue, we performed a basic test to measure the accuracy of the 27-band photometric redshifts. We have compiled a sample of 2860 sources which have spectroscopic redshifts included in the catalogue, and we compare them with the photometric redshifts obtained with BPZ2.0.

We show in the bottom panel of Figure 4.4 the result of the comparison. The median magnitude of those sources with spectroscopic counterpart is K_s = 20.39; with first and third quartiles Q_1 = 19.57 and Q_3 = 21.19. We measure a dispersion $\sigma_{\rm NMAD}$=0.018 and a catastrophic error rate $\eta_1 \sim 4.96\%$. Despite the fact that we have significantly increased the photometric information in terms of wavelength range, these results are worse than the obtained for the ALHAMBRA-K_s catalogue[2]. In the next section we will assess the possible reasons for this result.

[2]The value of $\sigma_{\rm NMAD}$ for a comparable sample without IRAC was ~ 0.013.

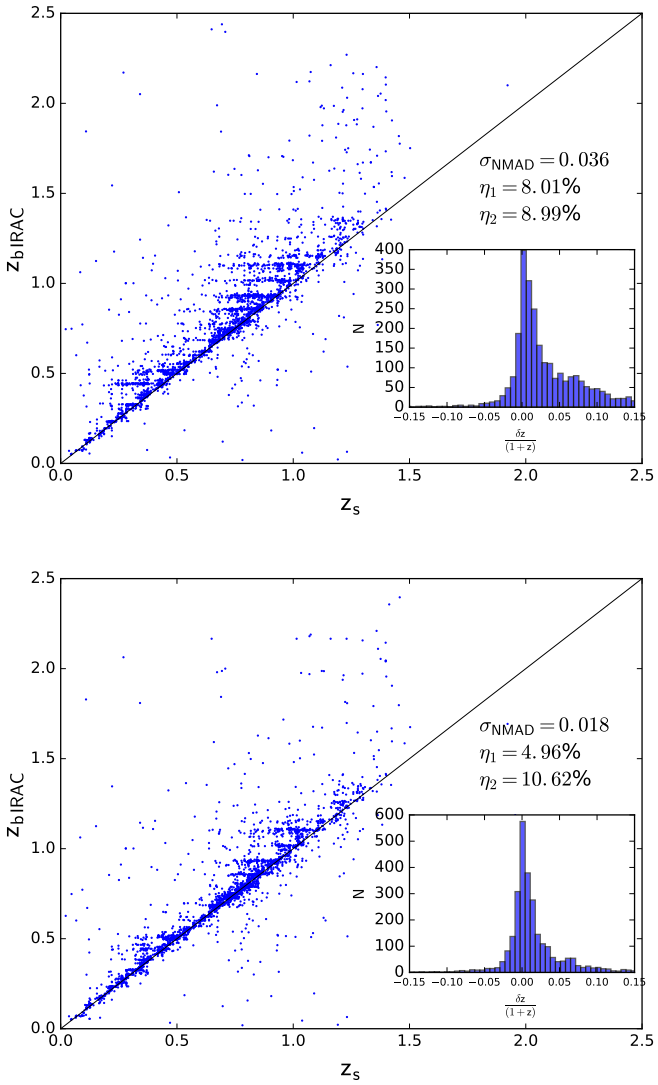

Figure 4.4: AK_sIR photometric redshift z_{bIRAC} vs. spectroscopic redshift z_s for a sample of 2860 sources. The top panel shows the results obtained in a preliminary BPZ2.0 analysis, including the $IRAC_{ch4}$ photometry, which yielded values of $\sigma_{NMAD} = 0.036$, $\eta_1 = 8.01\%$ and $\eta_2 = 8.99\%$. The bottom panel shows the photometric redshifts included in the final AK_sIR- catalogue, which yield significantly better values of $\sigma_{NMAD} = 0.018$, $\eta_1 = 4.96\%$ and $\eta_2 = 10.62\%$. The inset plots represent the distributions of $\delta_z/(1+z)$

Testing the BPZ2.0 templates in the IR range

In the previous section we noticed that the quality of the photometric redshifts is apparently worse when we include the IRAC channels in the analysis. At first sight one would expect that the accuracy of the results would improve when we increase the spectral information about the analysed sources. In this section we study the reasons that in fact lead us to the opposite result.

There are two main effects that may be causing these worse results. One of them could be due to any possible inconsistency between the photometry added from the IRAC channels. But in Section 4.1.1 we have performed different photometric tests that point at a good agreement with other works, and to a correct compatibility between the ALHAMBRA K_s-band and the IRAC catalogues, so we do not expect this to be an issue.

Another effect could be related with the ALHAMBRA/BPZ template set. We must keep in mind that the templates used for our analysis are those developed by (Benítez 2000, Benítez in preparation) for use in BPZ, and subsequently refurbished to be optimised for the analysis of the ALHAMBRA original catalogue (Molino et al. 2014). The templates were thus designed to work under their best conditions in the analysis of data covering the observed-frame wavelength range between 0.3 and 2.5 microns. We are now applying them out to 6 microns, and we think that this may in fact be the principal reason why we do not observe the expected improvement in photometric redshift accuracy. In this section we perform a test to analyse how the coverage of the SED-space in the NIR spectral range of the BPZ2.0 galaxy templates may affect our results. We want to remark that, in any case, the quality of the photometric redshift estimates is perefectly comparable to the one obtained with the original ALHAMBRA data.

To find out in detail how the use of the BPZ2.0 templates in the IR spectral range may interfere with the accuracy of the photometric redshift results, we have compared the apparent magnitude in each band with the apparent magnitude that we would expect to measure given the best-fit template and redshift for each source, using the BPZ `flux_comparison` files. That is, we subtracted the expected flux *if the template represented a perfect fit* from the one observed, and repeated the same for all galaxies in a large sample. We expect any systematic, significant, differences to give us clues about possible systematic effects.

For this work we defined a "good quality" galaxy sample which includes sources

with magnitudes in the range $17 < K_s < 19.5$ and $Odds > 0.2$. In addition, using the BPZ2.0 output parameter T_B, we separate the sample in red-type galaxies ($T_B < 5.5$) and blue-type galaxies ($T_B > 5.5$). For all the galaxies included in this sample we compared their measured fluxes and their expected template flux, as well as their corresponding errors in the ALHAMBRA bands $F814W$, J, H, K, and in the four IRAC channels[3].

We show in Figure 4.5 the study of a galaxy sample with redshift $z \in [0.20, 0.35]$. The dark-blue band shows the typical flux uncertainty measured in each band. In absence of systematic effects or errors in the uncertainty estimation, the expected and measured magnitudes should approximately fall within this band. The points are the median values of the difference between the observed and the expected magnitude in each filter, and the error-bars correspond to the sample dispersion of those differences. The violet and purple vertical lines mark the positions of the rest-frame wavelengths of 1.0μm and 2.5 μm at the mean redshift of the sample. The top panel shows the results for the blue-type subsample, and the bottom panel shows the results for the red-type galaxy galaxy one. It is noticeable that the red sample results seem to fit well both in the ALHAMBRA bands and in the IRAC channels. However, the blue sample shows an evident discrepancy in the IRAC channels, specially for the measurements in IRAC$_{ch3}$ and IRAC$_{ch4}$.

In order to check whether this effect is due to a template discrepancy, we repeated the same test for different redshift ranges. We tried to keep the homogeneity in the number of sources included in the samples. Figure 4.6 and Figure 4.7 show the same study performed for redshifts $0.5 < z < 0.7$ and $0.8 < z < 1.1$ respectively. We notice in these figures that at those redshifts ranges the average, systematic, differences between the observed magnitudes and the best fit template magnitudes are decreasing.

In order to check visually whether these differences are induced by a SED template mismatch or else, we look at the results of the average differences taking into account the rest-frame wavelength that each filter is probing at each redshift. The ensemble results are shown in Figure 4.8. In the top panel we represent the

[3]Although it is not included in our catalogue, we include the IRAC$_{ch4}$ data to perform this test in order to show more complete results

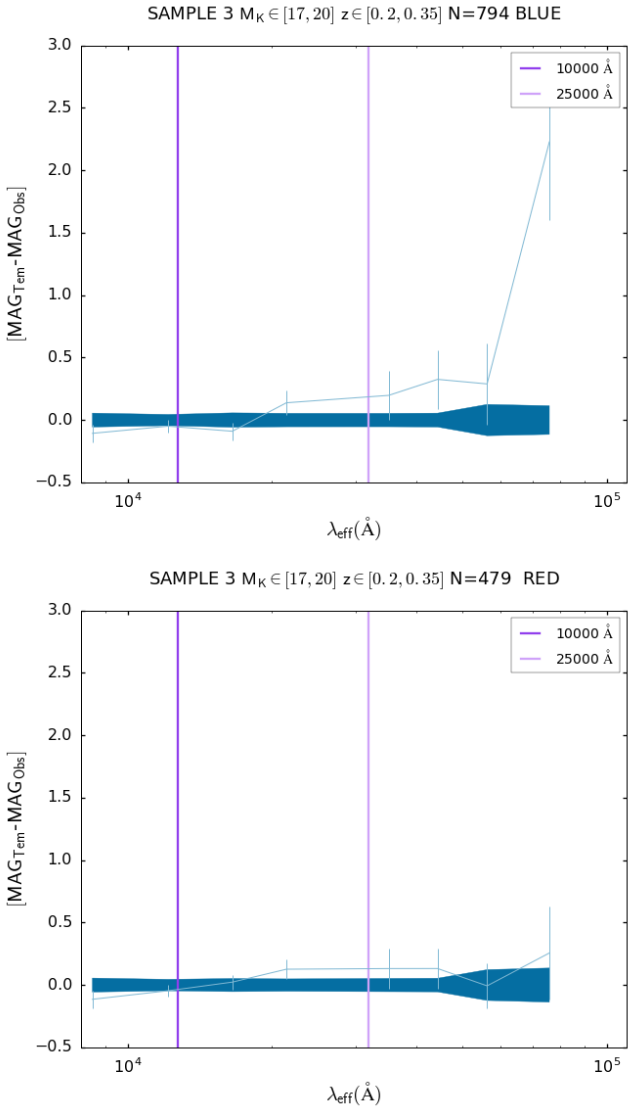

Figure 4.5: Result of the subtraction of the observed magnitude minus the expected template magnitude for the ALHAMBRA bands $F814W$, J, H, K, and the four IRAC channels, for sources with photometric redshift $z \in [0.2, 0.35]$. The dark-blue band around zero difference marks the typical source magnitude uncertainty in each band.The light-blue line shows the median of the subtraction in each filter and the error bars are the dispersion of the subtraction measurements. The violet (purple) vertical line marks a wavelength of 1 (2.5) μm in the rest-frame at the mean redshift under analysis. Top: Blue galaxies. Bottom: Red galaxies.

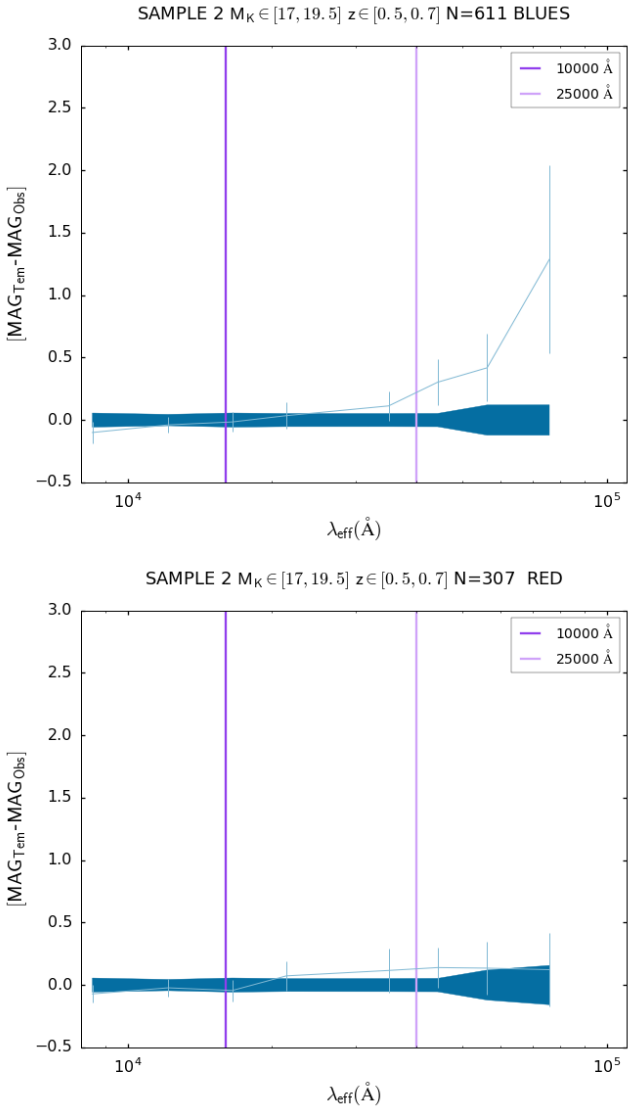

Figure 4.6: Result of the subtraction of the observed magnitude minus the expected template magnitude for the ALHAMBRA bands $F814W$, J, H, K, and the four IRAC channels, for sources with photometric redshift $z \in [0.50, 0.70]$. The dark-blue band around zero difference marks the typical source magnitude uncertainty in each band.The light-blue line shows the median of the subtraction in each filter and the error bars are the dispersion of the subtraction measurements. The violet (purple) vertical line marks a wavelength of 1 (2.5) μm in the rest-frame at the mean redshift under analysis. Top: Blue galaxies. Bottom: Red galaxies.

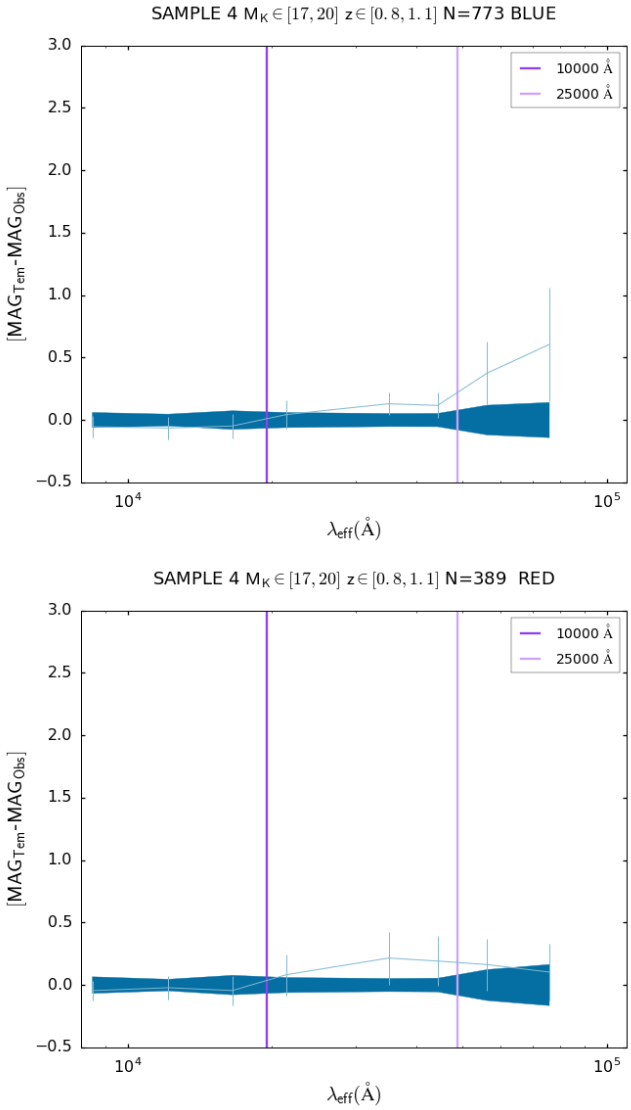

Figure 4.7: Result of the subtraction of the observed magnitude minus the expected template magnitude for the ALHAMBRA bands $F814W$, J, H, K, and the four IRAC channels, for sources with photometric redshift $z \in [0.80, 1.10]$. The dark-blue band around zero difference marks the typical source magnitude uncertainty in each band.The light-blue line shows the median of the subtraction in each filter and the error bars are the dispersion of the subtraction measurements. The violet (purple) vertical line marks a wavelength of 1 (2.5) μm in the rest-frame at the mean redshift under analysis. Top: Blue galaxies. Bottom: Red galaxies.

results for the blue-type galaxies in the rest frame: we have converted the X axis of the previous plots in terms of $\lambda/(1+z)$, where z is the average redshift in each range. In this plot we clearly see the discrepancy between the blue-type templates and the data at low redshifts is systematic. In fact, it grows very rapidly once we reach $\lambda > 2.5\,\mu$m, exactly when we leave the wavelength range for which the templates were originally optimised. On the other hand, the red-type galaxy data shows a good agreement with the templates over the whole redshift range.

We conclude from this study that the BPZ2.0 templates have a clear discrepancy for blue-type galaxies at low redshift when we include the IRAC channels photometry. There are two main possibilities to explain the results obtained: i) it is precisely in the IRAC filters at low redshift, that the effects of (non corrected) dust can be more significant, and ii) the template spectra have not been optimised in BPZ2.0 to analyse the spectral range $\lambda > 2.5\,\mu$m.

These results reinforce us in our decision not to use the IRAC$_{ch4}$ data, and convince us that we understand the reason why the quality of the photometric redshifts does not improve further with the addition of the new IRAC bands. We understand that, however, the addition of these new data greatly improves the quality of the data in terms of wavelength coverage and information content. The results obtained in this section will be taken into account for the building of an optimised SED-template library for future use with BPZ.

4.1.3 Cross-matched final catalogue

The AK_s-IR catalogue includes the photometry of 36 024 sources, distributed in the overlapping area between the ALHAMBRA fields and the fields whit IRAC public data. We have obtained a cross-matched catalogue that includes photometry through the ALHAMBRA 20 filters in the optical range, the ALHAMBRA $F814W$ synthetic band, the ALHAMBRA NIR JHK_s bands, and the IRAC channels at 3.5 μm, 4.5 μm and 5.8 μm (see Figure 4.9. The total area is 0.93 deg^2. The properties for each field are shown in Table 4.1. We include in Appendix B the content and description of the individual columns. This catalogue will now be used to calculate the luminosity function as is described in the text below.

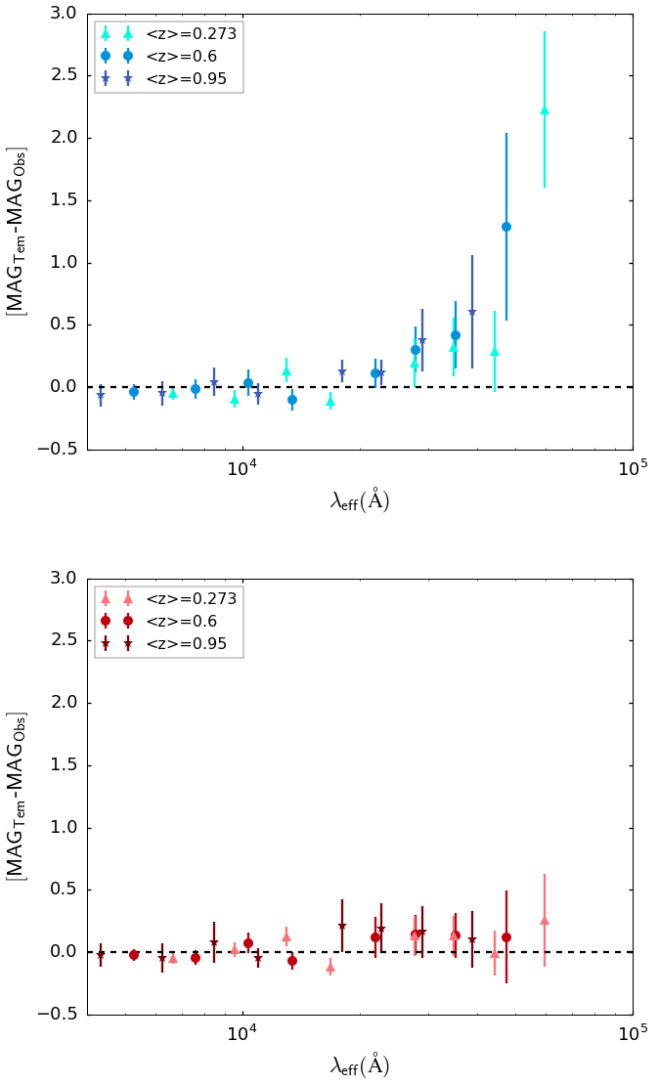

Figure 4.8: Average differences between observed magnitude and expected template magnitude obtained for the eight broad-band filters and the three redshift ranges $z \in [0.2, 0.35]$, $z \in [0.5, 0.7]$ and $z \in [0.8, 1.1]$ in terms of $\lambda/(1+z)$. The top panel shows the results obtained for the blue-type galaxies from the lower redshift range (light-blue) to the higher redshift range (dark-blue). Analogously, on the bottom panel we plot the results for the red-type galaxies from the lower redshift (light-red) to the higher redshift (dark-red).

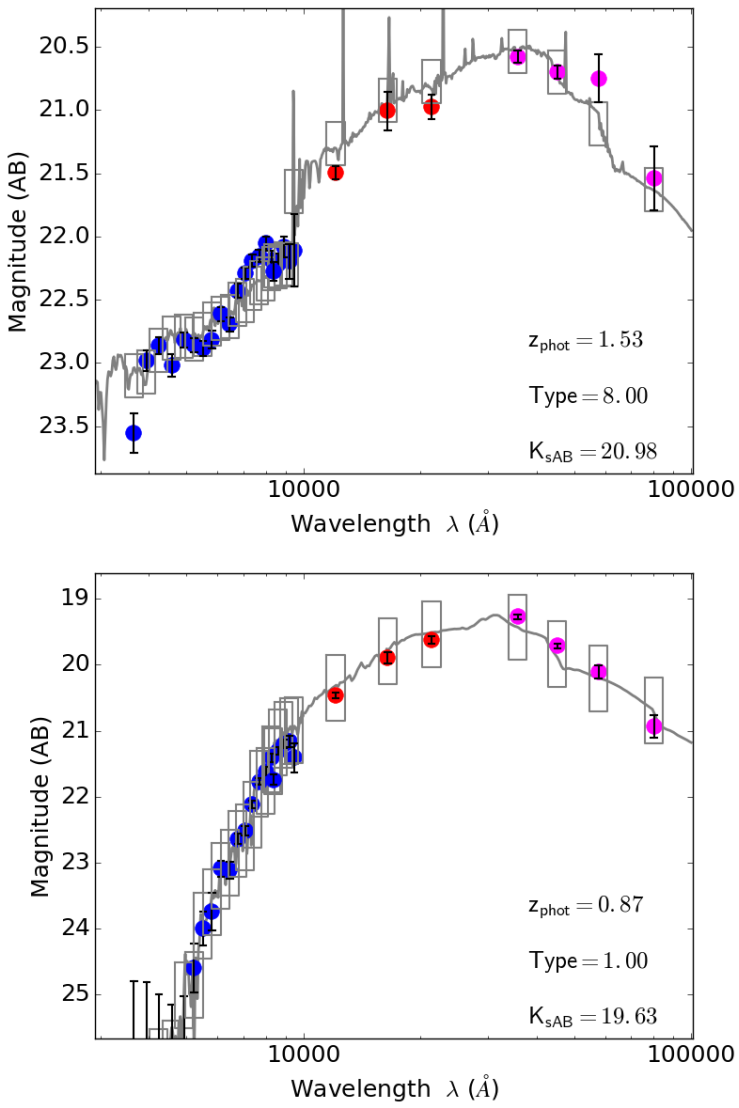

Figure 4.9: Example of ALHAMBRA+IRAC pseudo-spectra and best fits of a blue-type and of a red-type galaxy. The blue markers correspond to the optical ALHAMBRA bands, red markers to a ALHAMBRA JHK and magenta markers to *Spitzer* IRAC data.

4.2 K_s-band luminosity function

As we introduced in Chapter 1, the luminosity function (LF) is a powerful statistical tool that provides information about the processes of galaxy formation and evolution. In this section we present the rest-frame K_s-band luminosity function (K_s-band LF) computed from the K_s-IR catalogue which combines ALHAMBRA and IRAC information. We use this catalogue for the calculation of the LF instead of the ALHAMBRA K_s-band catalogue we presented before because the wavelength extension that the IRAC data provides allows us to extend the rest-frame analysis to the K band, and this compensates the fact that this dataset is smaller (in terms of numbers) than the previous one.

The techniques we employ are very similar to the ones developed for the analysis that was performed to measure the ALHAMBRA B-band luminosity function in López-Sanjuan et al. (2017). First we will describe the methodology to measure the K_s-band LF using a PDFs analysis, and then we will present the K_s-band LF segregated for red-type galaxies and for blue-type galaxies in several redshift bins. Finally, we will discuss the main results we obtain.

4.2.1 Measuring the LF with PDFs

The photometric redshifts computed using the BPZ2.0 (or any other similar code) are not exact values but estimates. Many applications treat the best-fit estimates of redshift and type as precise pieces of data and apply classical methods that rely on them and ignore the probability distribution function (PDF) that is also an important part of the BPZ output. An example is shown if Figure 4.10, where we can see the Probability Distribution Function for an individual galaxy (i) in the 2D-space defined by redshift z and spectral type T_B. In case we were interested only in the redshift PDF distribution, we would use:

$$PDF_i(z) = \int PDF_i(z, T) dT. \tag{4.2.1}$$

The main advantage of using the full PDF information instead of the estimated value of the photometric redshift as a point value, is that the PDF contains much more information, and when it is properly used it allows to improve very notably the accuracy of the LF measurements. Further information about the BPZ PDFs can be found in Benítez (2000) and Molino et al. (2014). An adequate use of

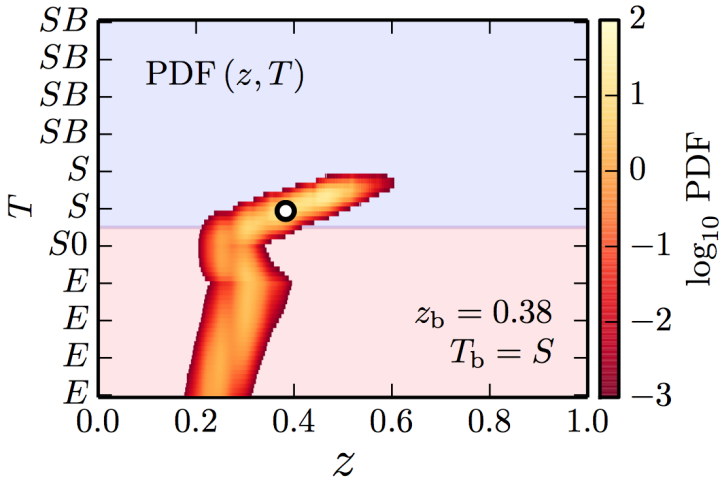

Figure 4.10: Probability distribution function (PDF) represented in the redshift-spectral type space ($z-T$) for a given galaxy with apparent magnitude $F814W = 22.17 \pm 0.06$. According to our operational definition, we shade in blue the area that is occupied by blue templates and in red the one occupied by red templates. The white dot marks the (Bayesian) best fit in (z-T) space, as labelled. This value provides the best fit in terms of photometric redshift z and SED-template. Figure from López-Sanjuan et al. (2017).

the PDF allows us to use all the objects in the catalogue for the LF analysis, as the uncertainties in each one are correctly taken into account in the process. On the other hand, if we chose to treat the photometric redshift of each object as a single-valued estimate, we would need (at the very least) to define a stringent cut in the *Odds* parameter, thus reducing the size of the sample by a large factor.

For the estimation of the K_s-band LF we will use the BPZ2.0 full PDFs obtained for the AK_s-IR catalogue. As in this work we will segregate our galaxy sample and estimate the LF for both blue-type and red-type galaxies, we will define for operational purposes a spectral threshold: red-type galaxies will be those with spectral templates $T_B < 5.5$, and blue-type galaxies will be those with $T_B > 5.5$. Please note that we do not take any decission for *individual galaxies*, but that we apply this definition to the PDFs, in such a manner that any given galaxy will contribute a fractional amount to the red and blue galaxy LF, depending on the exact shape of its PDF. Under this assumption, we can write the PDFs for red-type galaxy and for blue-type galaxy as:

$$\mathrm{PDF}_i(z) = \int_{T<5.5} \mathrm{PDF}_i(z,T)dT + \int_{T>5.5} \mathrm{PDF}_i(z,T)dT. \tag{4.2.2}$$

We can also express the probability of a given galaxy i, to be either red or blue as:

$$P_i^{red} = \int \mathrm{PDF}_i(z, T_{red})dz, \tag{4.2.3}$$

$$P_i^{blue} = 1 - P_i^{red} = \int \mathrm{PDF}_i(z, T_{blue})dz. \tag{4.2.4}$$

Galaxies in our sample are selected by their observed magnitude in the K_s-band, and not by their real intrinsic apparent magnitude, that we denote as K_{s0}. Both quantities are obviously linked by a stochastic relation that involves the measurement uncertainty σ_{K_s}. This will induce effects of bias or incompleteness in the galaxy samples, so we need a measurement of the number of sources corrected by incompleteness and selection effects. For that aim we define the Source Function $S(K_{s0})$ as:

$$S(K_{s0}|K_s, \sigma_{K_s}) = \frac{1}{f_c(K_0)} \mathrm{PDF}(K_{s0}|K_s, \sigma_{K_s}) \int P(K_s|K_{s0}, \sigma_{K_s})dK_{s0} \tag{4.2.5}$$

where K_{s0} is the real magnitude at a given observed magnitude K_s, σ_{K_s} is the photometric error and f_c is the completeness function obtained in Section 2.10.

The $P(K_s|K_{s0},\sigma_{K_s})dK_{s0}$ term is the probability of observe K_s having a real magnitude K_{s0} and a photometric redshift error σ_{K_s}.

4.2.2 Sample selection

Following a process similar to the one developed and presented in López-Sanjuan et al. (2017), we have made a sample selection of sources included in the AK_s-IR catalogue. We have excluded stars from the catalogue using the star/galaxy parameter presented in Section 2.5, and we also exclude sources with $Odds > 0.2$. The latter correspond to objects for which there is no good spectral fit within the BPZ2.0 template set, probably in some cases because they are dominated by AGN, they correspond to stellar objects not correctly identified by other means, or suffer from contamination from different sources. This kind of objects were already noticed in Molino et al. (2014), and represent a small fraction of the catalogue in our case ($\sim 4.5\%$ of the total sample).

As discussed above we will separate our analysis in two LFs according to the observed galaxy colours, with "red" galaxies having $T_B \leq 5.5$, and "blue" galaxies having $T_B > 5.5$. We should emphasise that these red and blue colours do not necessarily represent a one-to-one split in star-forming and quiescent galaxies. As shown in López-Sanjuan et al. (2017), some dust-reddened star-forming galaxies could be described by red colour templates in BPZ2.0. In a future work we will in fact quantify this effect by adding stellar population and dust content information obtained by running the MUFFIT (Díaz-García et al. 2015) code on our sample.

4.2.3 Treatment of an individual galaxy

In the following sections we briefly describe the method for the estimation of the LF using the full PDFs. As is show in Equation 4.2.1, the PDF is defined in the $z-T$ space. In order to compute the LF, it is necessary to convert the PDFs into the space formed by redshift, type, and absolute magnitude M_{K_s}. Using Equation 1.6.39 for the K_s-band we have

$$M_{K_s}(z,T|K_{s0}) = K_{s0} - 5\log[D_L(z)] - k(z,T) - 25 \tag{4.2.6}$$

where $D_L(z)$ is the luminosity distance in Mpc and $k(z,T)$ is the k-correction for the K_s-band at a given redshift. From this equation we can derive the probability

distribution of each ALHAMBRA galaxy i in the $(z-M_{K_s})$ space, as was done for the B-band analysis in (López-Sanjuan et al. 2017). The probability distribution of each individual galaxy from the AK_s-IR catalogue is given by

$$P_i(z, M_{K_s}|K_i)dM_{K_s} = \int \mathbf{1}_{M_{K_s}}(M_{K,i})\mathrm{PDF}_i(z,T)dT \tag{4.2.7}$$

Where $\mathbf{1}_{M_{K_s}}$ is an index function, valued =1 when $M_{K,i} \in [M_{K_s}, M_{K_s}+dM_{K_s}]$ and =0 otherwise. It is important to emphasise that the uncertainties of the observed colours in the "new" (z, M_{K_s}) space, include the correlation between both variables. From this equation we have used the probability using the observed magnitude K_s. To compute the final $\mathrm{PDF}(z, M_{K_s})$, it is necessary to convolve this probability with the Source Function of equation 4.2.5, obtaining

$$\mathrm{PDF}_i(z, M_{K_s}) = P_i(z, M_{K_s}|K_{s,i}) * S(K_{s0}|K_{s,i}, \sigma_{K_{s,i}}). \tag{4.2.8}$$

The individual $\mathrm{PDF}_i(z, M_{K_s})$ thus estimated for a single galaxy can be thought of as an "atom" of the luminosity function, that includes all the information about that particular galaxy. It is obvious that in the case of a well-defined, single-peaked PDF this would be a delta function and would take us back to the classical LF estimate.

In order to further illustrate the method explained we show in Figure 4.11 the probability distributions in the (z, M_B) space for a galaxy with magnitude $I = 22.17 \pm 0.06$. This figure corresponds to the B-band LF analysis by López-Sanjuan et al. (2017). The top panel shows the $P_i(z, M_B|I)$ (the corresponding term in the K_s selected catalogue would be $P_i(z, M_{K_s}|K_i)$), whereas the bottom panel shows the convolved probability $PDF(z, M_B)$ ($PDF(z, M_{K_s})$ in the K_s-selected catalogue). These plots clearly show the effect of the Source Function, that increases the uncertainty on the "real" absolute magnitude of the source. The method we will follow is the same applied in the work by López-Sanjuan, adapted for use in the rest-frame K_s-band.

4.2.4 Ensemble LFs

Using these results it is possible to estimate the partial PDFs that correspond to the different galaxy types. Taking into account the equations 4.2.5 and applying the Source Function we obtain the partial PDFs for blue (T_{blue}) and red-type

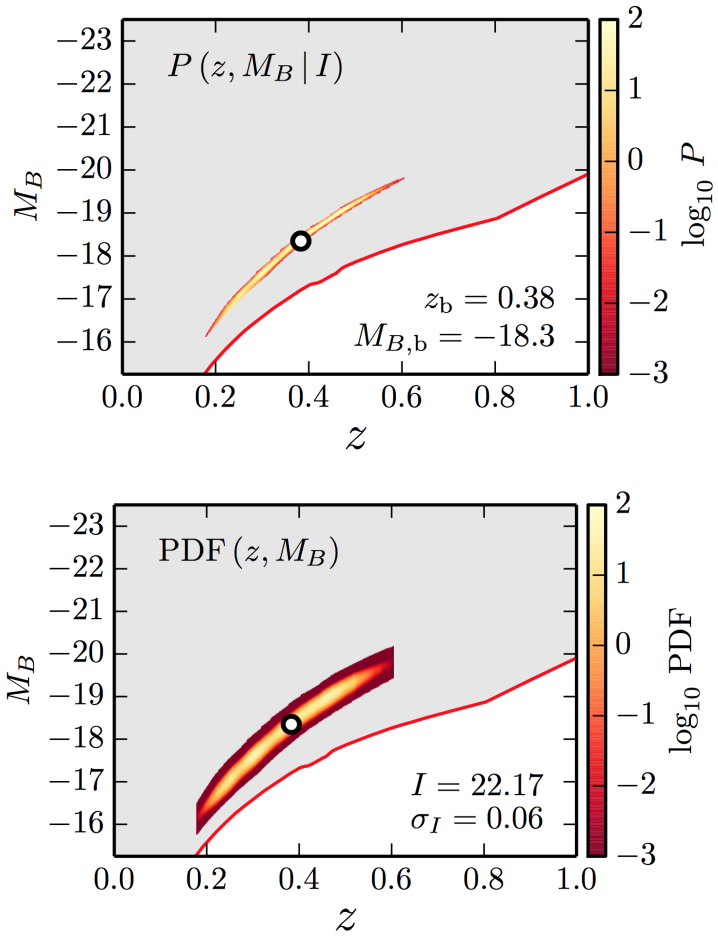

Figure 4.11: Probability distribution function represented in the redshift-absolute magnitude space ($z - M_B$) for a selected galaxy with magnitude $I = 22.17 \pm 0.06$. The red line in the plot marks the survey limit magnitude $I_0 = 24$, and the grey area is the accessible volume in the z, M_B space. The top panel represents $P_i(z, M_B|I)$ and the bottom panel panel shows the convolved probability $PDF(z, M_B)$. The white dot marks the best-fit solution in the (z, M_B) space. Figure from López-Sanjuan et al. (2017)

(T_{red}) galaxies as[4]:

$$\mathrm{PDF}_i(z, M_{K_s}|T_{red}) = P_i(z, M_{K_s}|K_{s,i}, T \leq 5.5) \times S(K_{s0}|K_{s,i}, \sigma_{K_{s,i}}), \quad (4.2.9)$$

$$\mathrm{PDF}_i(z, M_{K_s}|T_{blue}) = P_i(z, M_{K_s}|K_{s,i}, T > 5.5) \times S(K_{s0}|K_{s,i}, \sigma_{K_{s,i}}) \quad (4.2.10)$$

Sheth & Rossi (2010) demonstrated that the real LF in photometric surveys can be built using the posterior probability functions given by $PDF(z, M_K)$. Following the method presented in López-Sanjuan et al. (2017), we obtain the LF of the ALHAMBRA field j as:

$$\Phi_j(z, M_{K_s}) = \frac{1}{A_j} \sum_j \mathrm{PDF}_i(z, M_K) \left(\frac{dV'}{dz} \right)^{-1} \quad [\mathrm{Mpc}^{-3}\,\mathrm{mag}^{-1}] \quad (4.2.11)$$

where the i index represents the galaxies in the field, A_j is the area in deg^2 subtended by the field j, and $\frac{dV'}{dz}$ is the differential cosmic volume.

In the same way that we already did for the PDFs for red and blue-type galaxies, we can obtain the LF for each galaxy type as:

$$\Phi_j^{red}(z, M_{K_s}) = \Phi_j(z, M_{K_s}|T_{red}), \quad (4.2.12)$$

$$\Phi_j^{blue}(z, M_{K_s}) = \Phi_j(z, M_{K_s}|T_{blue}) \quad (4.2.13)$$

and from these equations it is possible to obtain the total LF as

$$\Phi_j^{tot}(z, M_{K_s}) = \Phi_j(z, M_{K_s}|T_{red}) + \Phi_j(z, M_{K_s}|T_{blue}) \quad (4.2.14)$$

We imposed a limit in the apparent K_s magnitude $K_s < 21.5$ for the calculation of the luminosity functions. The limit in the absolute magnitude M_{K_s} that is seen, for example, in Figure 4.11 corresponds to the brightest template at a given redshift z that yields an apparent K_s-band magnitude $K_s < 21.5$ (the same

[4]López-Sanjuan et al. (2017) perform an analysis to estimate the probability of star-forming/quiescent galaxies to be assigned to a wrong subsample because of dust extinction. We have not yet completed that analysis in our case, and the consequences will be discussed later.

limit is seen in Figures 4.13 and 4.16). At this point, it should be remarked that the selection of the sample was made a posteriori, using all the galaxy PDFs, and the work was performed in real magnitudes, with the aim of avoiding edges and completeness effects induced by the binning in magnitude or redshift.

To ensure a correct processing of the errors in the LF, the resolution of the $\Phi_j(z, M_{K_s})$ was degraded to create a binned LF. Following the same physical arguments as followed for the ALHAMBRA B-band LF (López-Sanjuan et al. 2017), we set the absolute magnitude bin size to $\Delta M_{K_s} = 0.3$, and the redshift bin size to Δz =0.2. Finally, we obtain the total binned K_s-band LF combining the estimation for each field, as:

$$\Phi^{tot} = \Phi^{T_{blue}} + \Phi^{T_{red}} = \sum_t \Phi^t = \sum_t \frac{1}{N} \sum_j \Phi_j^t \tag{4.2.15}$$

where the index t runs the galaxy types, and the index j runs the number of AK_s-IR fields.

4.2.5 Estimation of the LF uncertainties

The LF errors are dominated by two main terms (Robertson 2010; Smith 2012): the Poissonian term due to statistical errors (shot noise) and the cosmic variance term. The first term is due to correlations in adjacent bins caused by the uncertainties in photometric redshift and the observed magnitudes. The estimation for this term was computed using a bootstrap method (Davison & Hinkley 2013).

In this work we could not assess adequately the cosmic variance term because the AK_s+IR catalogue contains only 4 different fields. We have used the cosmic variance results obtained in López-Sanjuan et al. (2017) for their study of the ALHAMBRA B-band LF as an approximation.

A full covariance matrix analysis is performed in order to estimate the uncertainties in the calculation of the LF. The covariance matrix encodes the complete information of the correlations between the redshift and magnitude uncertainties, and also the correlations due to the cosmic variance. We denote in the text the covariance matrix term as

$$\Sigma_\Phi = \Sigma_P + \Sigma_\nu \tag{4.2.16}$$

where the first term corresponds to the shot noise, and the second to the cosmic variance.

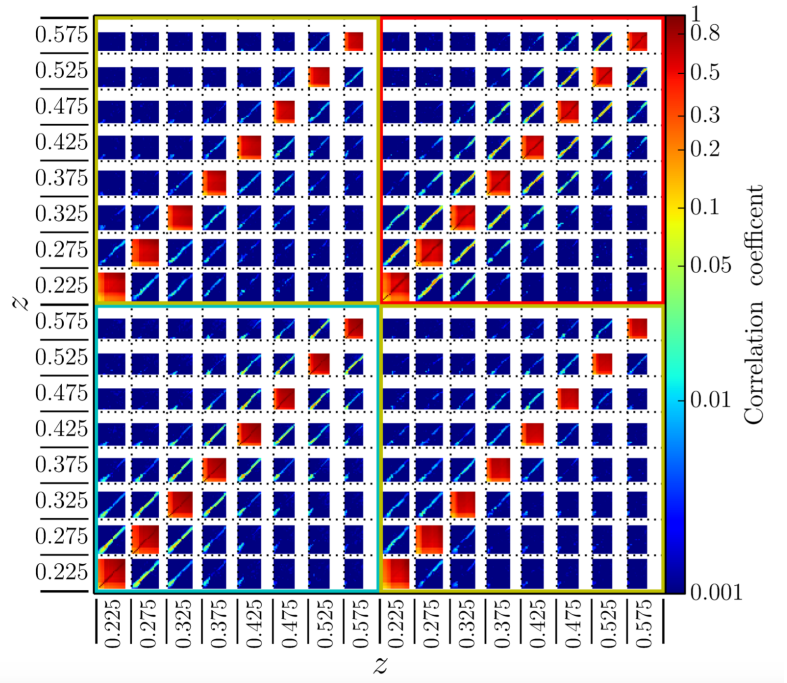

Figure 4.12: Correlation coefficients of the covariance matrix estimated for the ALHAMBRA B-band LF. The axes are binned according to the different redshift ranges for star forming galaxies (blue box), quiescent galaxies (red box) and the cross-terms between star forming and quiescent (green boxes). Within every small box the correlation between luminosities is plotted. The auxiliary axes marks the value of correlation coefficient. Figure from López-Sanjuan et al. (2017).

In Figure 4.12, we plot the correlation coefficients of the first eight redshift bins in the case of the study of the ALHAMBRA B-band LF covariance matrix. There are obvious correlations between galaxies of the same type and redshift due to the photometric uncertainties. Correlations at different types and close redshifts are inherited from the definition of the redshift bins and the uncertainties in the PDFs. A similar work was performed to the K_s-band LF.

4.2.6 Modelling the K_s luminosity function

For the modelling of the K_s-band LF we used a combination of Schechter functions (Schechter 1976) for the different galaxy-type samples. As we have introduce in

Chapter 1, the Schechter function is defined with three different parameters: i) the characteristic magnitude denoted by $M^{\star}_{K}$, ii) the characteristic density $\phi^{\star}$, and iii) the slope of the power-law at the faint-end. The Schechter function is thus formally defined as:

$$\mathcal{S}(M_{K_s}|M^{\star}_{K_s},\phi^{\star},\alpha) = 0.4\ln(10)\phi^{\star}\frac{10^{0.4[M^{\star}_{K_s}-M_{K_s}](1+\alpha)}}{exp\left\{10^{0.4[M^{\star}_{K_s}-M_{K_s}]}\right\}}. \tag{4.2.17}$$

The model blue-type galaxy LF as a function of redshift is defined using a redshift-dependent Schechter function, as:

$$\Phi^{BT}_{mod}(z, M_{K_s}|\theta^{BT}_{\Phi}) = \mathcal{S}(M_{K_s}|M^{\star}_{K_s,BT}(z), \phi^{\star}_{BT}(z), \alpha_{BT}) \tag{4.2.18}$$

where we have defined:

$$M^{\star}_{K_s,BT}(z) = M^{0}_{K_s,BT} + Q_{BT}(z-0.5), \tag{4.2.19}$$

and

$$\log\phi^{\star}_{BT}(z) = \log\phi^{0}_{BT} + P_{BT}(z-0.5). \tag{4.2.20}$$

Assuming that the behaviour of the α_{BT} parameter is constant with redshift, we encode the model parameter set as

$$\theta^{BT}_{\Phi} = [M^{0}_{K_s,BT}, Q_{BT}, \phi^{0}_{BT}, P_{BT}, \alpha_{BT}] \tag{4.2.21}$$

In the same manner as done for the blue-type galaxies, we define the model LF for red-type galaxies taking into account that for these galaxies we need to model the excess of faint elliptical galaxies (identified as f) (Madgwick et al. 2003; Loveday et al. 2012). We include in the model a second Schechter function, so we end up with a first term to describe the bright part of the LF and a second term for the faint part. The final double Schechter function is defined as:

$$\Phi^{RT}_{mod}(z, M_{K_s}|\theta^{RT}_{\Phi}) = \mathcal{S}(M_{K_s}|M^{\star}_{K_s,RT}(z), \phi^{\star}_{RT}(z), \alpha_{RT}) + \mathcal{S}(M_{K_s}|M^{\star}_{f}, \phi^{\star}_{RT}(z), \beta). \tag{4.2.22}$$

As we did for blue-type galaxies, the functional dependence on the redshift of $M^{\star}_{K_s,RT}(z)$ and $\phi^{\star}_{RT}(z)$ can be included using equations like 4.2.19 and 4.2.20, and the K_s-band LF for red-type galaxies is described by the model parameter set:

$$\theta^{RT}_{\Phi} = [M^{0}_{K_s,RT}, Q_{RT}, \phi^{0}_{RT}, P_{RT}, \alpha_{RT}, M_f, \beta] \tag{4.2.23}$$

For simplicity we only consider a linear evolution of the Schechter function parameters with redshift[5]. This leads us to a set of 12 parameters with which we must fit the red and blue-type K_s-band luminosity functions.

The fit to the data was performed using the MonteCarlo code `emcee` (Foreman-Mackey et al. 2013). Both the median values and their dispersions were estimated for each parameter using the projected solutions given by the code.

4.2.7 K_s-band Luminosity Funcion

In this section we present the K_s-band LF results, including the segregated blue- and red-type galaxy LFs, and the global one. We also present and discuss the redshift evolution of the Schechter parameters $M^{\star}_{K_s}$ and $\phi^{\star}$, and an analysis of the K_s-band luminosity density j_{K_s} obtained as an integral of the LF. We also compare our results with those of previous groups that have performed similar analyses.

In Figure 4.13 we show the K_s-band LF for blue-type galaxies $\Phi(z, M_{K_s}|BT)$ in the two-dimensional space defined by redshift z and absolute magnitude in the K_s-band. We have plotted the differential (top panel) and the binned (bottom panel) LF versions. The differential K_s-band LF shows over-dense regions in redshift space possibly due to cosmic structures and also to correlations in the (z, M_K) space. In the binned version, all these structures fade out. At the faintest regions, a volume effect due to the absent of sufficient data can be noticed.

Blue LF

We show in Figure 4.14 the results of the K_s-band LF calculation in different redshift ranges (as labelled in each panel), selected to facilitate comparison with previous works. The LF values included in this plot are given in Appendix C. In each figure we plot the observed luminosity function and its uncertainty (blue dots with error bars), and the best-fit median model and its uncertainty (blue band and shadowed area). We have also included the results and Schechter fit from UKIDSS (Cirasuolo et al. 2010), and the Schechter fit from GALEX VIMOS-VLT

[5]Other evolutionary forms could be treated, but a model with linear evolution yields a good fit to our data.

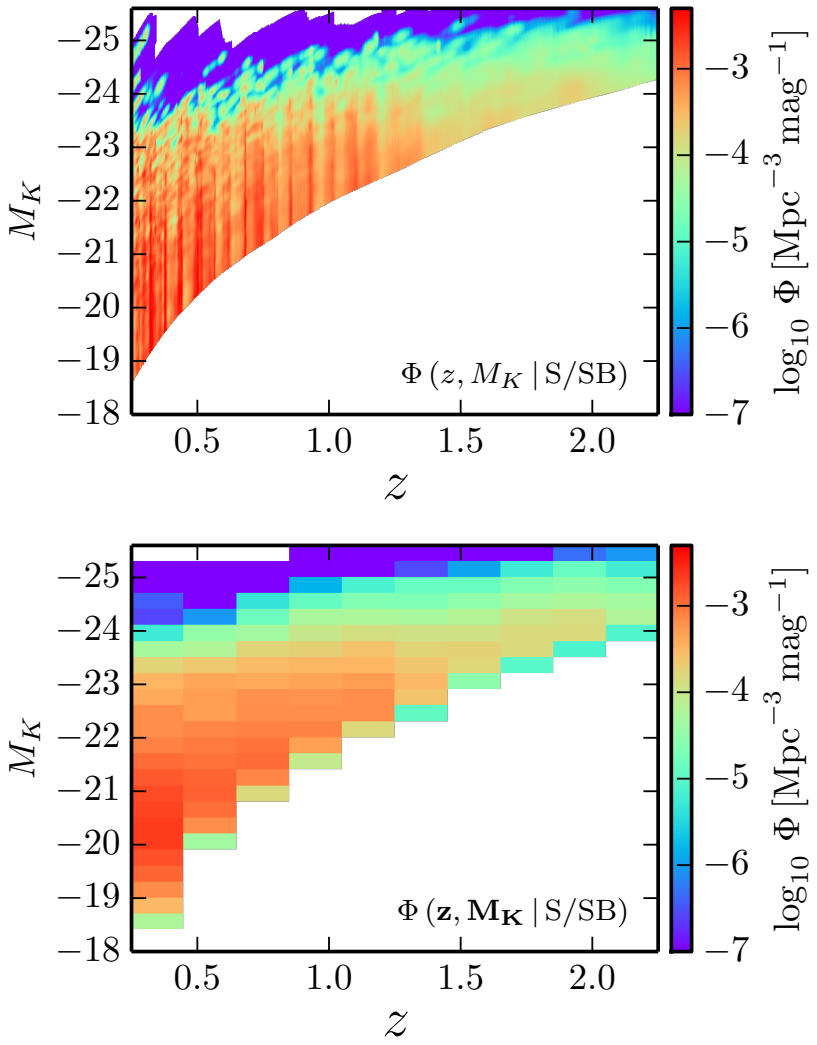

Figure 4.13: Top panel: K_s-band differential luminosity function of blue-type galaxies in the (z, M_{K_s}) plane. Bottom panel: Binned luminosity function using Δz =0.2 and ΔM_{K_s} =0.3. The K_s-band LF has been calculated with an apparent magnitude limit K_s =21.5.

(Arnouts et al. 2005b). We observe a good agreement with the results obtained in Cirasuolo et al. (2010). However, both our results and the results obtained by Cirasuolo et al. (2010) show in general lower densities than the Arnouts et al. (2005b)—except at the very highest redshift.

The slight discrepancies observed in the different LFs in the plot could be due to the different galaxy-type selection criteria performed in each work (our selection is colour-based, wheras Arnouts et al. (2005b) used spectroscopy to separate the quiescent and star-forming populations), to the difficulty of properly characterising the galaxy types due to the absence of emission lines or a clear Balmer break in the $1.75< z <2.25$ redshift range, or to cosmic variance effects.

Red LF

We show the results of the K_s-band LF for the red-type galaxies in a analogous way to that we have done previously with the blue-type sample. In Figure 4.16 we show the K_s-band LF for red-type galaxies $\Phi(z, M_{K_s}|RT)$ in the two dimensional space defined by z and the absolute magnitude M_{K_s}. As we have done for the blue-type sample, we plot the differential (top panel) and the binned (bottom panel) LF versions. As in the case of blue-type galaxies, the differential K_s-band LF, shows over-dense regions in redshift space due to the cosmic structures and also due to the correlations in the (z, M_K) space that fade out in the in the binned version. As expected we also notice a relative decrement in the LF values in the faintest part of the plot, due to completeness effects.

In Figure 4.16 we present the results of the K_s-band LF over the same redshift ranges we presented for the blue-type sample. We also list the values of the LF points in Appendix C. Each panel includes the observed luminosity function and its uncertainty (red dots), and the double Schechter function model for red-type galaxies (red dashed line) and its uncertainty (shadow red band). Likewise, we have included the results from UKIDSS (Cirasuolo et al. 2010) and GALEX VIMOS-VLT (Arnouts et al. 2005b). Once again, we observe a good agreement with previous results, although at the higher redshift range our data are in better agreement with Cirasuolo et al. (2010).

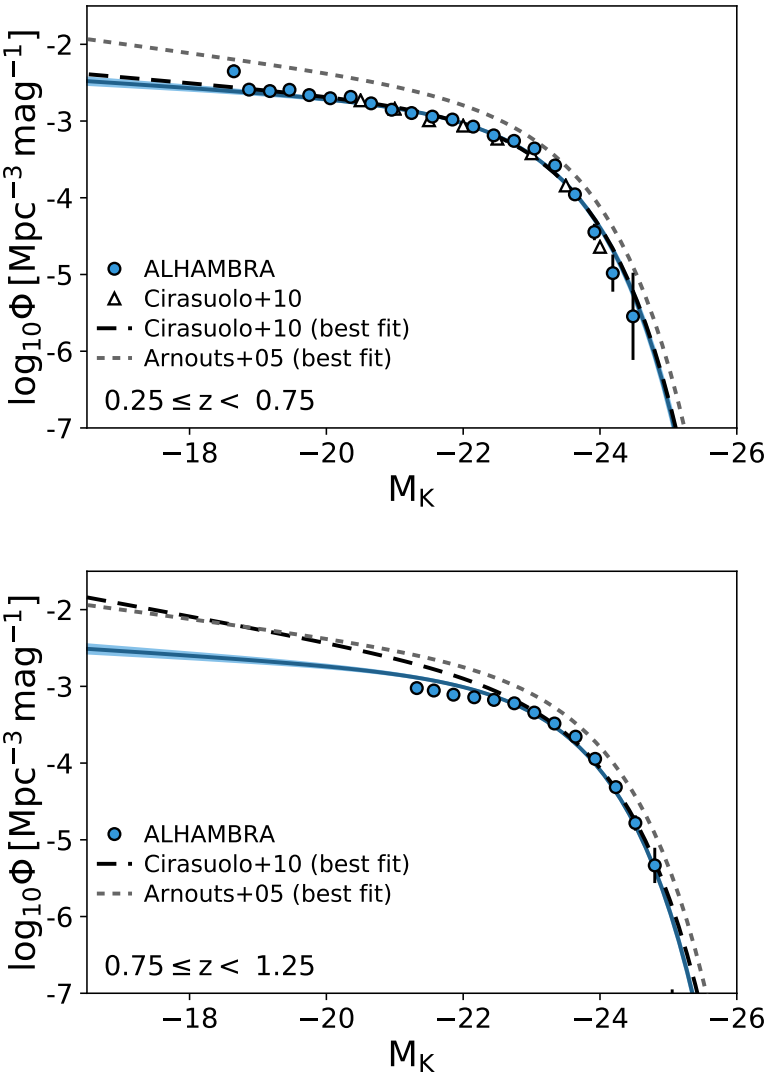

Figure 4.14: K_s-band luminosity function estimated for the blue-type galaxy sample in different redshift ranges as labelled in each panel. Blue dots with error bars, the blue dark line, and the light blue band correspond to our results. Long- and short-dashed lines are the best-fits obtained from UKIDSSS Cirasuolo et al. (2010) and GALEX VIMOS-VLT Arnouts et al. (2005b). White triangles are measurements from UKIDSSS Cirasuolo et al. (2010).

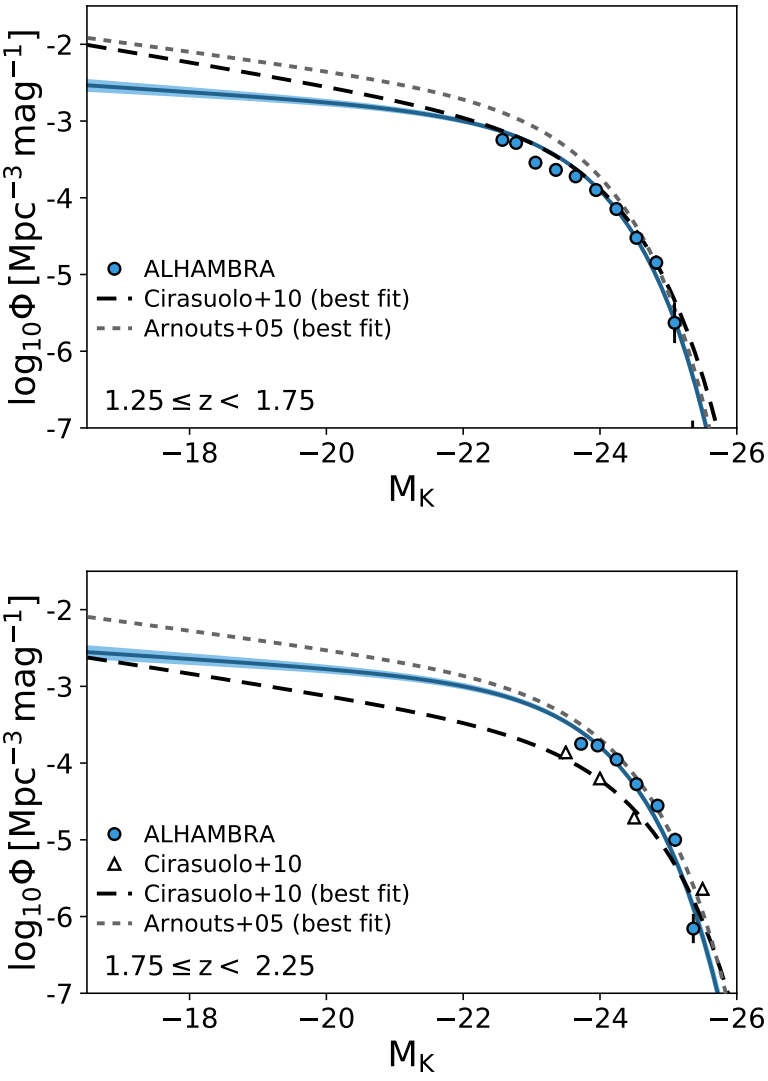

Figure 4.14: (continued)K_s-band luminosity function estimated for the blue-type galaxy sample in different redshift ranges as labelled in each panel. Blue dots with error bars, the blue dark line, and the light blue band correspond to our results. Long- and short-dashed lines are the best-fits obtained from UKIDSSS Cirasuolo et al. (2010) and GALEX VIMOS-VLT Arnouts et al. (2005b). White triangles are measurements from UKIDSSS Cirasuolo et al. (2010).

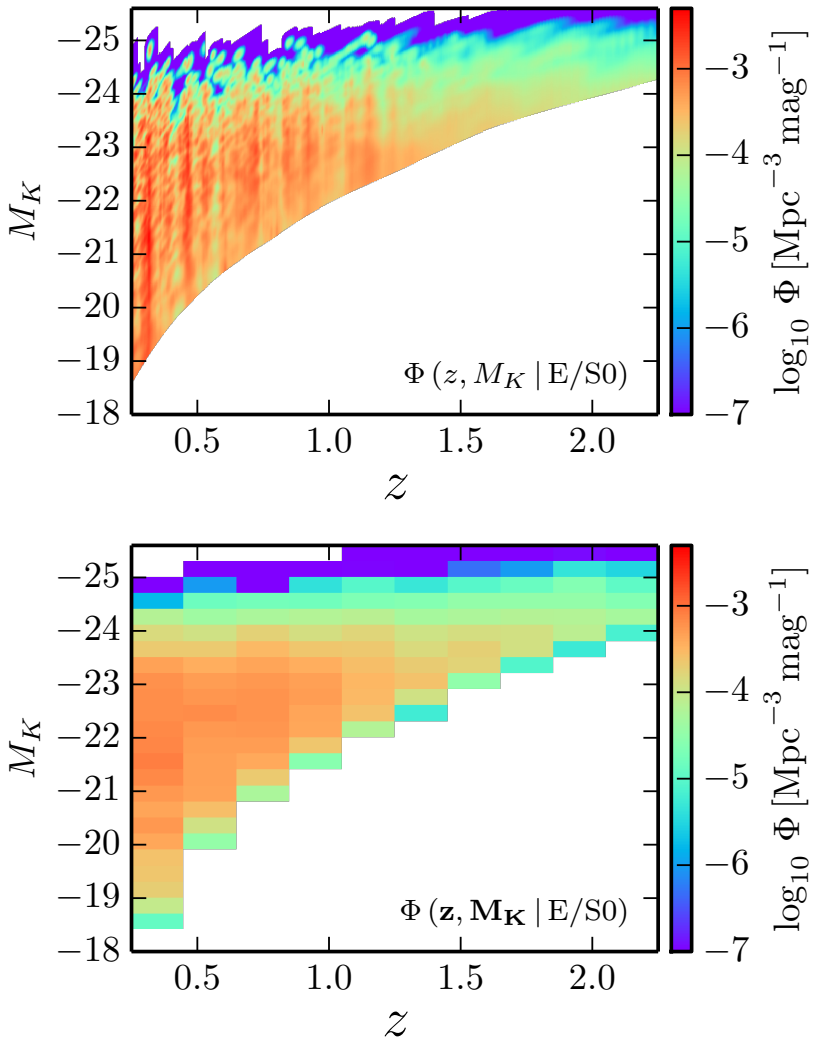

Figure 4.15: Top panel: K_s-band differential luminosity function of red-type galaxies in the (z, M_{K_s}) plane. Bottom panel: Binned luminosity function using Δz =0.2 and ΔM_{K_s} =0.3. The K_s-band LF has been calculated with an apparent magnitude limit K_s =21.5.

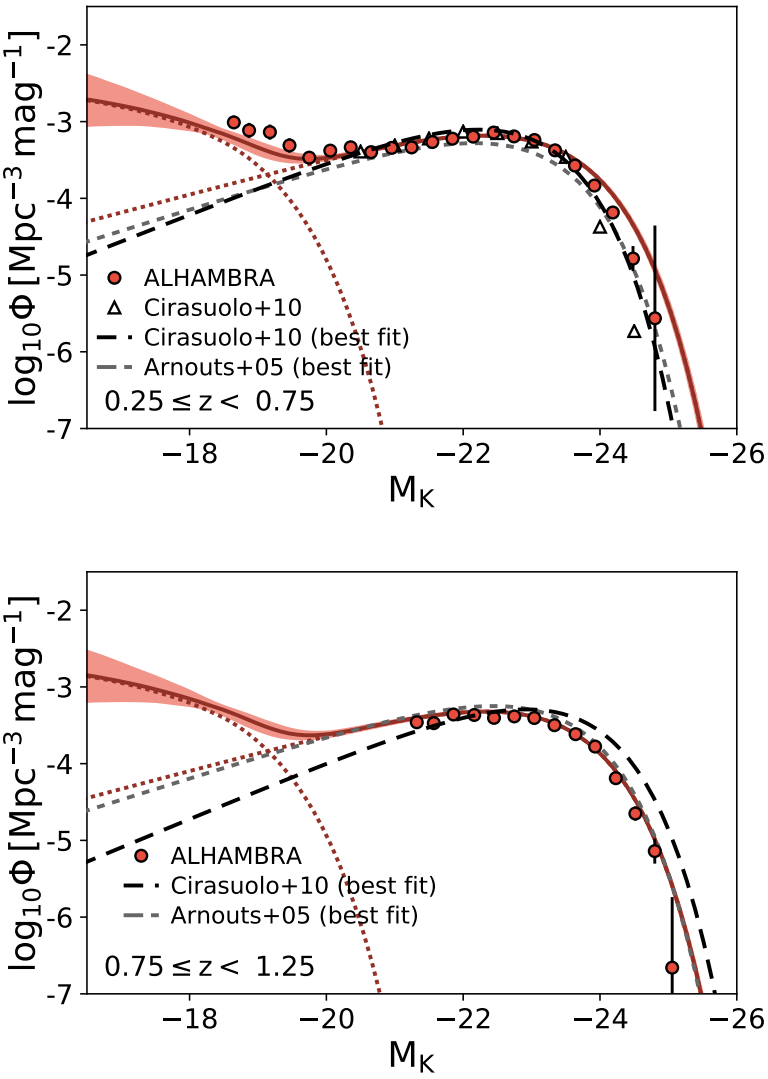

Figure 4.16: K_s-band luminosity function estimated for the red-type galaxy sample, over the different redshift ranges labelled in each panel. Red dots marks the observed K_s luminosity function, the red dark line is the median Schechter model and the light red band marks the uncertainty in the model. Dotted red lines show the faint and bright components of the Schechter model. Dark long- and short-dashed lines are the best-fit models obtained from UKIDSSS (Cirasuolo et al. 2010) and GALEX VIMOS-VLT (Arnouts et al. 2005b). White triangles are from UKIDSS (Cirasuolo et al. 2010).

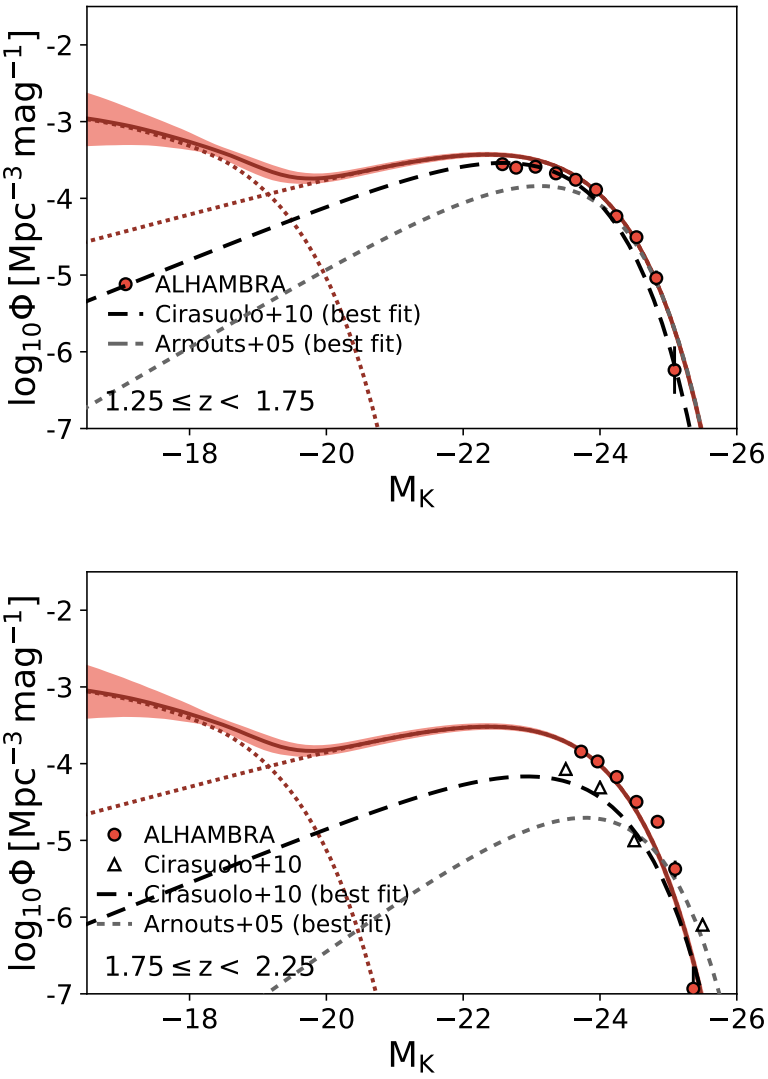

Figure 4.16: (continued)K_s-band luminosity function estimated for the red-type galaxy sample, over the different redshift ranges labelled in each panel. Red dots marks the observed K_s-band luminosity function, the red dark line is the median Schechter model and the light red band marks the uncertainty in the model. Dotted red lines show the faint and bright components of the Schechter model. Dark long- and short-dashed lines are the best-fit models obtained from UKIDSSS (Cirasuolo et al. 2010) and GALEX VIMOS-VLT (Arnouts et al. 2005b). White triangles are from UKIDSS (Cirasuolo et al. 2010).

Full LF

In order to explore the agreement with other results found in the literature we also calculate the global K_s-band LF for the complete sample.

We show in Figure 4.17 the results of the K_s-band LF: the green points with the corresponding error-bars are the observed K_s-band LF and their uncertainties. The green dashed line is the Schechter-function obtained as $\mathcal{S}(M_{K_s}|M^\star_{K_s}) = \mathcal{S}(M_{K_s}|M^\star_{K_s,BT}) + \mathcal{S}(M_{K_s}|M^\star_{K_s,RT})$, and the green shadowed region marks the uncertainty of this model.

On the same diagrams we plot the results for the global LF obtained by Mortlock et al. (2017) as white dots and a short-dashed line, and also the Schechter fit obtained by Cirasuolo et al. (2010). We observe that our global LF is in excellent agreement with the results of both groups, particularly when compared with Cirasuolo et al. (2010) at all redshifts explored.

LF parameters and evolution

Finally, we present in Figure 4.18 the redshift evolution of the parameters used to describe the Schechter-function fit for both the blue (in blue) and red (in red) galaxy types. In all cases the circles correspond to the data from Cirasuolo et al. (2010) and the triangles to the data from Mortlock et al. (2017). There is a fair scatter in both cases, although we must remark that the parameters $M^\star_K$ and ϕ^* are strongly (anti-)correlated, so that the error bars in these plots, when only one of both parameters is included, must be taken with caution.

In all the plots we represent the results from our best-fit full LF model, as given in Equations 4.2.19 and 4.2.20. We use dashed dark-colour lines (red and blue), surrounded by shadowed areas of the same colour that represent their uncertainty.

In the top panel we represent the evolution of $M^\star_{K_s}$. We observe that $M^\star_{K_s}$ undergoes an evolution of over one magnitude[6] for the blue galaxies, whereas there is no significant evolution of $M^\star_{K_s}$ in the case of red-type galaxies. This results points at the possibility of negative luminosity evolution in the blue galaxies, as would be expected from the regular model in which the largest, most strongly star-forming events happened in the past and progressively disappeared. In red

[6]We refer in these comparisons to the redshift range z=0.0 to z=2.5.

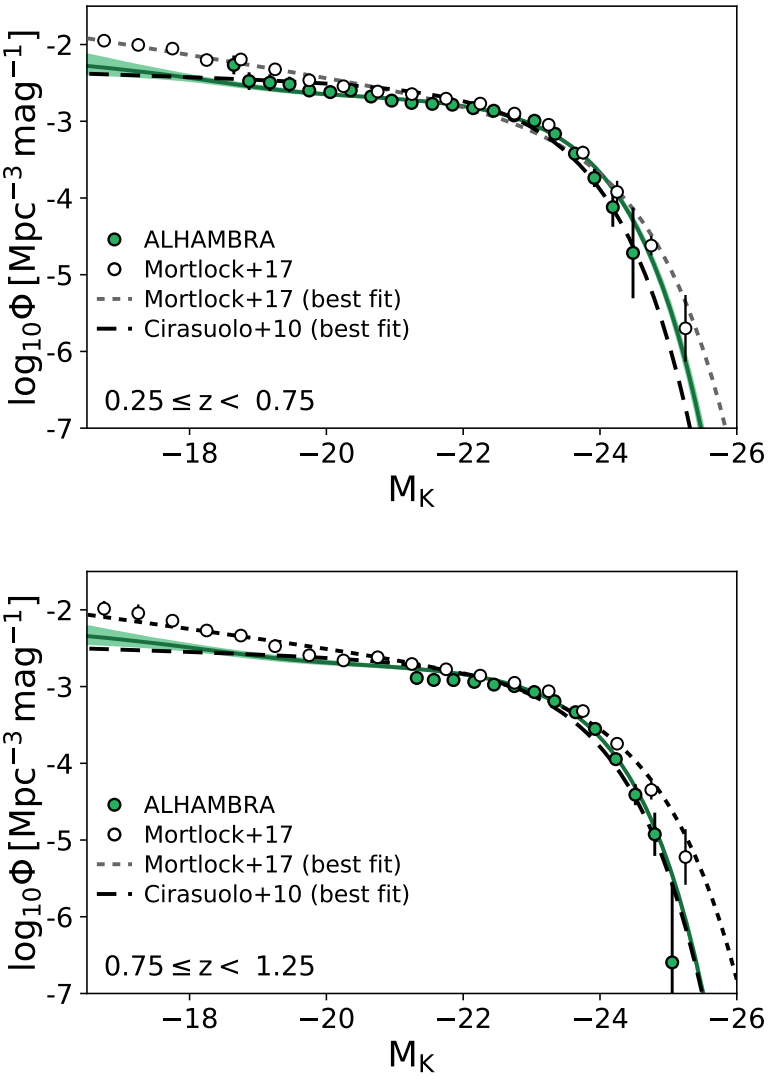

Figure 4.17: K_s-band luminosity function measured for the complete galaxy sample in different redshift ranges as labelled in each panel. Green dots mark the observed K_s-band global luminosity function, the green dark line is the median Schechter model and the light green band marks the uncertainty in that model. Long- and short-dashed lines show the best-fit models obtained by Cirasuolo et al. (2010) and Mortlock et al. (2017). White circles are from Mortlock et al. (2017).

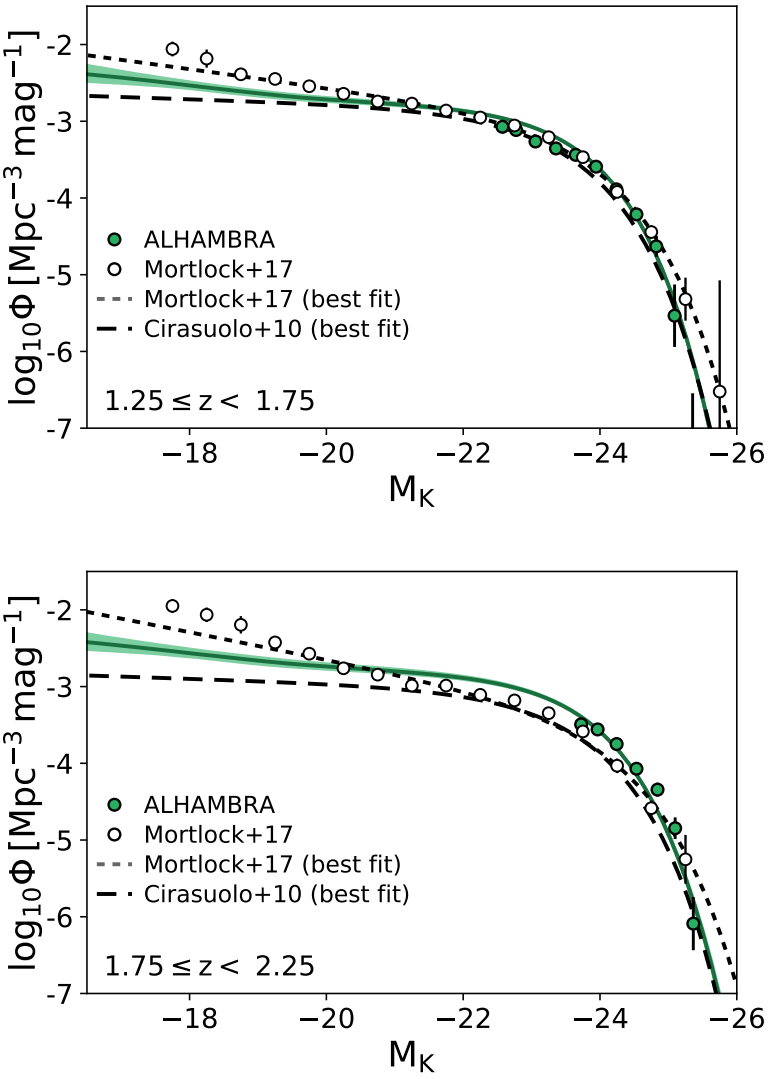

Figure 4.17: (continued) K_s-band luminosity function measured for the complete galaxy sample in different redshift ranges as labelled in each panel. Green dots mark the observed K_s-band global luminosity function, the green dark line is the median Schechter model and the light green band marks the uncertainty in that model. Long- and short-dashed lines show the best-fit models obtained by Cirasuolo et al. (2010) and Mortlock et al. (2017). White circles are from Mortlock et al. (2017).

Table 4.2: Values and uncertainties obtained for the parameters that best describe the redshift-evolving Schechter luminosity function models: $M^0_{K_s,BT}, Q_{BT}, \phi^0_{BT}, P_{BT}, \alpha_{BT}$ for the blue sample and $M^0_{K_s,RT}, Q_{RT}, \phi^0_{RT}, P_{RT}, \alpha RT, M_f, \beta$ for the red sample.

Blue-type sample						
$M^0_{K_s,BT}$	Q_{BT}	ϕ^0_{BT}	P_{BT}	α_{BT}		
-22.67 ± 0.04	-0.67 ± 0.05	-2.80 ± 0.02	-0.12 ± 0.04	1.44 ± 0.03		
Red-type sample						
$M^0_{K_s,RT}$	Q_{RT}	ϕ^0_{RT}	P_{RT}	α_{RT}	M_f	β
-22.86 ± 0.05	-0.09 ± 0.05	-2.8 ± 0.02	-0.33 ± 0.04	-0.40±0.04	-18.41 ±0.2	-1.19 ± 0.5

galaxies, on the other hand, the behaviour of the $M^\star_{K_s}$ parameter shows that the most massive red galaxies are already present at earlier cosmic times, having evolved only minimally until the present.

In the middle panel we show the evolution of $\phi^\star_{K_s}$. We observe in this case that there is some evolution in both types. Only a hint of evolution for the blue galaxy population, in the sense of the density growing from the past towards the present, and a larger evolution in the same direction for red-type population. Once again we can interpret this evolution in the frame of the usual galaxy formation and evolution paradigm, as indicating that the red population is getting increasingly dominant, mostly through the processes of secular evolution in individual galaxies, as the amount of gas left to undergo new star formation events gets continuously depleted.

In the final panel of Figure 4.18 we show the results obtained for the K_s-band luminosity density $\mathrm{j_K}$, which is obtained when the LF model is integrated over all luminosities. We find that the luminosity density for blue-type galaxies selected in the K_s-band decreases approximately by a factor of 2 from redshift $z = 2.5$ to redshift $z = 0.0$, reflecting a descent in the star formation rate in the Universe. On the other hand, the luminosity density of red-type galaxies increases almost a factor of 4 with cosmic time over the same range, which certainly marks the passage of galaxies from one galaxy population to the other.

The best fit values for all the parameters and their estimated uncertainties are listed in Table 4.2.

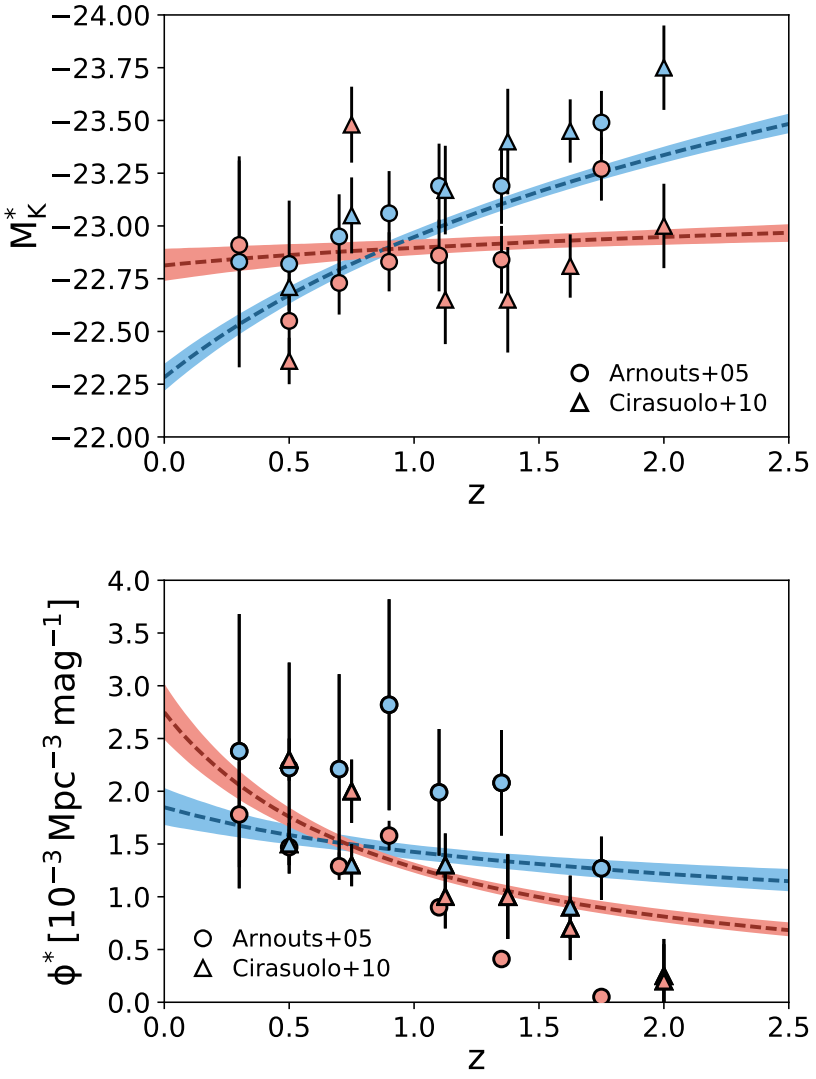

Figure 4.18: Redshift evolution of the best-fit Schechter-function model parameters $M^{\star}_{K_s}$ and $\phi^{\star}_{K_s}$. In both panels we present our own results for both the blue and red samples (with the corresponding colours) as the dashed lines, with the shadow areas representing their 1σ uncertainty. Triangles mark the results from Cirasuolo et al. (2010) and circles mark the results from Arnouts et al. (2005b).

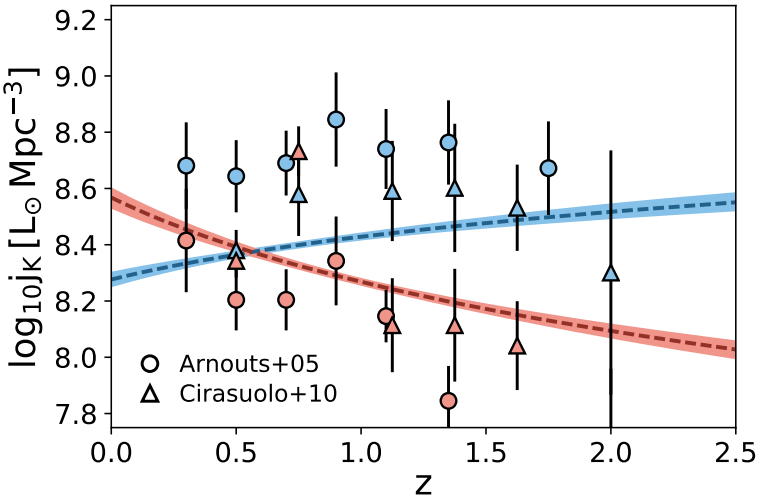

Figure 4.18: (continued) Redshift evolution of the best-fit Schechter-function model integral j_K, the luminosity density. We present our own results for both the blue and red samples (with the corresponding colours) as the dashed lines, with the shadow areas representing their 1σ uncertainty. Triangles mark the results from Cirasuolo et al. (2010) and circles mark the results from Arnouts et al. (2005b).

Chapter 5

Conclusions and future work

In this final chapter we sumarise the main results and conclusions presented in this Thesis, and comment on the main lines of work that we will pursue in order to fully exploit and complete our work.

5.1 ALHAMBRA K_s-band catalogue

We have presented in this thesis the photometric redshift catalogue of sources detected in the ALHAMBRA K_s-band images. The catalogue includes photometry for 94,182 sources distributed over seven fields, covering a total area of 2.47 deg^2. This catalogue is different from the original ALHAMBRA catalogue presented in Molino et al. (2014) because that sample was selected based on a synthetic F814W image, similar to an I-band selection. Such a selection is biased against intrinsically red galaxies at redshift $z \gtrsim 1$, an effect that became noticeable in several of the works based on the ALHAMBRA survey. This issue sparked our interest in producing a new catalogue where this bias would be avoided by selecting in the reddest band available.

Source detection and photometry was performed using SExtractor in dual mode. We estimated the photometric errors using the method presented by Labbé et al. (2003), and used an adapted version of the masks created in Arnalte-Mur et al. (2014) to define the survey window. Star-galaxy separation was performed using a colour-colour diagram, and tested with the SEDs of the NGSL stellar

library. We calculated detailed completeness functions for every pointing using the deeper UltraVISTA catalogue of the ALHAMBRA-4/COSMOS field as reference (Muzzin et al. 2013). We applied this completeness functions to extend our magnitude limit and the number counts to magnitude $K_s \approx 21.9$. Two separate tests were performed to check the photometric accuracy of our catalogue: an internal test against the photometry of those objects common to our catalogue and the original ALHAMBRA catalogue presented in Molino et al. (2014), and an external test using the objects common to our catalogue and UltraVISTA. In both cases the cross-catalogue accuracy has been shown to be compatible with that expected from the respective uncertainties, and with no significant bias.

We completed our catalogue by running the BPZ2.0 code over our sample, including the zeropoint photometric recalibration option that uses a spectroscopic redshift sample to refine, at the same time, both the photometry and the photometric redshift accuracy. Using a spectroscopic redshift sample with 3736 galaxies, and the normalised median absolute deviation (NMAD) as an estimator of the accuracy of our results, we obtain $\sigma_{\rm NMAD} = 0.011$, and a catastrophic error rate $\eta_1 \sim 2.23\%$, both comparable to the ones obtained by Molino et al. (2014). We performed a second comparison, in this case with the photometric redshifts in the ALHAMBRA F814W-selected catalogue. This comparison yields $\sigma_{\rm NMAD} = 0.009$ with a catastrophic error rate $\eta_1 \sim 0.58\%$. As expected, because of the motivation of our work, the photometric redshift distribution segregated by galaxy type shows that many of the new K_s-selected sources fill the dearth of early-type galaxies in the F814W-selected sample at $z \gtrsim 1$.

In the future we intend to exploit this catalogue by selecting populations of targets of particular interest. Our first objective will be to define a representative, significant sample of moderate-redshift, massive, red galaxies optimised to obtain moderate resolution spectroscopy that will allow us to study their masses and star formation histories (*à la* Longhetti & Saracco 2009). We intend to compare those results with the ones that can be obtained from broad-band based stellar population synthesis codes like MUFFIT (Díaz-García et al. 2015), in order to characterise the accuracy of the latter in deriving the main parameters.

5.2 ALHAMBRA K_s-band red galaxy clustering

We have studied the clustering properties of red-type galaxies in the redshift range $0.75< z <1.45$, extending the work performed in Hurtado-Gil et al. (2016). We have used the same method described in Arnalte-Mur et al. (2014) to estimate the projected correlation function $w_p(r_p)$. In order to generate a homogeneous, well-defined, clean sample, we selected galaxies from our ALHAMBRA K_s-selected catalogue with T_b <5.5, $Odds > 0.5$ and a limiting magnitude $K_s < 21.0$. Under these restrictions we have produced a sample with 13702 galaxies covering an effective area A_{eff}= 2.46 deg^2.

To study the evolution and luminosity dependence of the clustering we binned the sample both in redshift z and absolute magnitude M_B. We selected three overlapping redshift ranges, and several B-band luminosity thresholded samples in each of them.

We measured the values of the projected correlation function for each subsample using the Landy-Szalay estimator (Landy & Szalay 1993), and modelled the projected correlation function $w_p(r_p)$ performing a power-law fit. From this power-law we recovered the parameters γ and r_0.

We presented the results of the measure of the projected correlation function and we observed some interesting features. At the range of scales analysed, from $r_p \sim 0.15\,\mathrm{Mpc}\,h^{-1}$ to $r_p \sim 12\mathrm{Mpc}\,h^{-1}$ the correlation function for all the subsamples is well fitted by a power-law. However, as was also observed in the measurements presented in (Hurtado-Gil et al. 2016), the results show a possible break towards a larger slope at scales $r_p \lesssim 1$ Mpc h^{-1}. We will settle the significance of this possible break in a deeper analysis in the future.

We detected some evolution in redshift, specially at the higher redshift end and for the more luminous samples. In our results we appreciate that galaxies at higher redshift cluster more strongly, and we notice in the higher redshift sample that more luminous galaxies are also more clustered.

The same result is detected when we analyse the behaviour of the best-fit parameters r_0 and γ. We also appreciated in this results the evolution in redshift, particularly comparing the highest redshift results with the other two.

We will present in a future manuscript this whole section, together with a more complete analysis of the observed evolution of the clustering of the red

population with redshift and luminosity. We will also include the analysis of the bias associated to the different subsamples and its possible change with time. Another future work involves the search for individual large structures (galaxy clusters) as probed by massive red galaxies at $z \gtrsim 1.2$, which was not possible using the general ALHAMBRA catalogue because of the dearth of red galaxies at those redshifts induced by the selection in the F814W band (Ascaso et al. 2015).

5.3 ALHAMBRA+IRAC cross-match catalogue

In order to extend the photometry in the infrared wavelength range, we performed a cross-correlation of our K_s-band selected catalogue with public data from the *Spitzer Space Telescope* Infra-Red Array Camera (IRAC, Fazio et al. 2004). Images taken with this instrument could add photometric data to our catalogue in four new bands, centered at 3.6, 4.5, 5.8, and 8.0 μm. We have found IRAC counterparts for sources included in the following K_s-band catalogue fields: ALHAMBRA-2 with the Spitzer Enhanced Imaging Products (SEIP) catalogue (Strasburger et al. 2015), ALHAMBRA-4 with the COSMOS Spitzer (S-COSMOS) survey (Sanders et al. 2007), ALHAMBRA-6 with the Extended Groth Strip (EGS) catalogue (Barmby et al. 2008), and ALHAMBRA-7 with the ELAIS-N1 field (Lonsdale et al. 2003).

We performed tests of our photometry comparing our results with those published in Barro et al. (2011) and also with the BPZ2.0 galaxy template redshifted tracks in colour-colour diagrams. Using these tests we confirm the consistency of the catalogue photometry, but we noticed that the photometric redshift estimations are improved when we avoid the 8.0 μm IRAC channel photometry. We conclude that this is due to the larger noise intrinsic to that band, but also to the fact that the BPZ templates have been optimised to work with SEDs out to 2.5 μm in the rest frame.

We have produced a new ALHAMBRA K_s+IRAC catalogue (AK_s-IR), including the photometry of the ALHAMRA K_s 20+3 filters, the synthetic $F814W$-band and the IRAC 3.6, 4.5 and 5.8 μm. The catalogue contains all the sources detected in the K_s-band catalogue in the overlapping area, for a total of 36,024 sources in a total area of 0.93 deg^2.

As we previously did with the K_s-selected catalogue, we completed the AK_s-

IR photometric catalogue by running the BPZ2.0 code over our sample, including the zeropoint photometric recalibration option that uses a spectroscopic redshift sample to refine, at the same time, both the photometry and the photometric redshift accuracy. Using a spectroscopic redshift sample with 2860 galaxies, and the normalised median absolute deviation (NMAD) as a estimator of the accuracy of our results, we obtain $\sigma_{\rm NMAD} = 0.018$, and a catastrophic error rate $\eta_1 \sim 4.96\%$.

Despite the fact that we have increased the SED wavelength information, the results obtained are slightly worse than those of the original ALHAMBRA-K_s data alone. We have performed a test to assess the behaviour of the BPZ2.0 templates in the IR range. The results show that there is a discrepancy between the data observed and the blue galaxy templates at low redshift in the IR. We notice that it is precisely in the IRAC bands at low redshift were the dust-effects in star-forming galaxies can begin to be more significant. We expect that this effects will be taken in account in posterior versions of BPZ.

5.4 K_s-band luminosity function

As the final part of this thesis, we have calculated the rest-frame K_s-band luminosity function using the data included in AK_s-IR catalogue. We computed the data using the method developed by López-Sanjuan et al. (2017). The method consist in measuring the K_s-band LF for both, red and blue galaxies, using the full probability distribution function (PDF) in a 2D-space. The PDFs are obtained as output from the BPZ2.0 analysis, and are defined in the redshift - spectral type (z, T) space. To calculate the K_s-band LF it is necessary to convert them from the PDF space (z, T) to the target PDF space redshift - absolute magnitude (z, M_{K_s}).

In order to complete a reliable analysis, we performed a sample selection of sources included in the AK_s-IR catalogue. We excluded stars from the catalogue and sources with $Odds < 0.3$. We also split the galaxy sample according to the observed galaxy colours, with "red" galaxies having $T_B \leq 5.5$, and "blue" galaxies having $T_B > 5.5$.

We modelled the K_s-band LF using a single Schechter function (Schechter 1976) for the blue-type sample, and a double Schechter-function for the red-type sample. We showed the results obtained for each galaxy-type sample and in

different redshift ranges and we represented the Shechter function obtained for the best parameter set, together with its uncertainties.

We compare our measurements with those obtained by Arnouts et al. (2005a) and Cirasuolo et al. (2010). At all redshifts and for both colour samples the results are in good agreement. Nevertheless, our results and those from Cirasuolo et al. (2010) show slightly lower densities than those obtained in Arnouts et al. (2005a).

The slight discrepancies observed in the different LFs could be due to the different galaxy-type selection criteria performed in each work (our selection is colour-based, wheras Arnouts et al. (2005b) used spectroscopy to separate the quiescent and star-forming populations), to the difficulty of properly characterising the galaxy types due to the absence of emission lines or a clear Balmer break in the $1.75< z <2.25$ redshift range, or to cosmic variance effects.

In order to compare the results with other recent works found in the literature as Mortlock et al. (2017) and Cirasuolo et al. (2010), a third analysis was performed using the complete sample. Once again we have obtained a good agreement with both results, especially with (Cirasuolo et al. 2010) in all the redshift ranges.

Finally, we analysed the redshift evolution of the parameters $M^{\star}_{K_s}$, $\phi^{\star}_{K_s}$ and the K_s-band luminosity density. We show that $M^{\star}_{K_s}$ undergoes an evolution of over one magnitude for the blue galaxies, and no significant evolution in the case of red-type galaxies. The results obtained indicate that the star-forming events in blue galaxies took place in the past and progressively disappeared. The behaviour of $M^{\star}_{K_s}$ in the case of red galaxies shows that the most massive of these galaxies are already present at earlier cosmic times, having evolved only minimally until the present.

In the case of the $\phi^{\star}_{K_s}$ parameter, we observed a hint of evolution for the blue galaxy population and a larger evolution for the red-type population from the early universe to the present time. In terms of galaxy formation and evolution, the results suggest that the red population is getting increasingly dominant, mostly through the processes of secular evolution in individual galaxies, as the amount of gas left to undergo new star formation events gets continuously depleted.

Finally we showed the results for the K_s-band luminosity density $\mathrm{j_K}$, which is obtained when the LF model is integrated over all luminosities. We find that

the luminosity density for blue-type galaxies selected in the K_s-band decreases approximately by a factor of 2 from redshift $z = 2.5$ to redshift $z = 0.0$, while the luminosity density of red-type galaxies increases almost a factor of 4 . This results reflects a descent in the star formation rate in the Universe (given by the blue sample) and reveals the passage of galaxies from one galaxy population to other.

This work is ready to be published, and it will be submitted together with a more accurate analyses of the implications of our results for different galaxy evolution scenarios.

Bibliography

Alpher, R. A. & Herman, R. C. 1948, Physical Review, 74, 1737

Anderson, L., Aubourg, É., Bailey, S., et al. 2014, MNRAS, 441, 24

Aparicio Villegas, T., Alfaro, E. J., Cabrera-Caño, J., et al. 2010, AJ, 139, 1242

Arnalte-Mur, P., Fernandez-Soto, Martínez, V. J., Saar, E., Heinämäki, P., & Suhhonenko, I. 2009, MNRAS, 394, 1631

Arnalte-Mur, P., Martínez, V. J., Norberg, P., et al. 2014, MNRAS, 441, 1783

Arnouts, S., Lonsdale, C. J., Ilbert, O., et al. 2005a, in Bulletin of the American Astronomical Society, Vol. 37, American Astronomical Society Meeting Abstracts, 1271

Arnouts, S., Schiminovich, D., Ilbert, O., et al. 2005b, ApJL, 619, L43

Arnouts, S., Walcher, C. J., Le Fèvre, O., et al. 2007, A&A, 476, 137

Ascaso, B., Benítez, N., Fernández-Soto, A., et al. 2015, MNRAS, 452, 549

Barmby, P., Huang, J.-S., Ashby, M. L. N., et al. 2008, ApJS, 177, 431

Barro, G., Pérez-González, P. G., Gallego, J., et al. 2011, ApJS, 193, 13

Benítez, N. 2000, ApJ, 536, 571

Benitez, N., Dupke, R., Moles, M., et al. 2014, ArXiv e-prints

Bennett, C. L., Halpern, M., Hinshaw, G., et al. 2003, ApJS, 148, 1

Bernardeau, F., Mellier, Y., & van Waerbeke, L. 2002, A&A, 389, L28

Bertin, E. & Arnouts, S. 1996, A&AS, 117, 393

Bertin, E., Mellier, Y., Radovich, M., et al. 2002, in Astronomical Society of the Pacific Conference Series, Vol. 281, Astronomical Data Analysis Software and Systems XI, ed. D. A. Bohlender, D. Durand, & T. H. Handley, 228

Bielby, R., Hudelot, P., McCracken, H. J., et al. 2012, A&A, 545, A23

Bolzonella, M., Miralles, J.-M., & Pelló, R. 2000, A&A, 363, 476

Cimatti, A., Daddi, E., Mignoli, M., et al. 2002, A&A, 381, L68

Cirasuolo, M., McLure, R. J., Dunlop, J. S., et al. 2010, MNRAS, 401, 1166

Coc, A., Uzan, J.-P., & Vangioni, E. 2013, ArXiv e-prints

Coil, A. L., Newman, J. A., Cooper, M. C., et al. 2006, ApJ, 644, 671

Cole, S., Percival, W. J., Peacock, J. A., et al. 2005, MNRAS, 362, 505

Colless, M., Dalton, G., Maddox, S., et al. 2001, MNRAS, 328, 1039

Cowie, L. L., Songaila, A., Hu, E. M., & Cohen, J. G. 1996, AJ, 112, 839

Cristóbal-Hornillos, D., Aguerri, J. A. L., Moles, M., et al. 2009, ApJ, 696, 1554

Cutri, R. M., Skrutskie, M. F., van Dyk, S., et al. 2003, VizieR Online Data Catalog, 2246

Daddi, E., Cimatti, A., Broadhurst, T., et al. 2002, A&A, 384, L1

Daddi, E., Cimatti, A., Renzini, A., et al. 2004, ApJ, 617, 746

Davis, M. & Geller, M. J. 1976, ApJ, 208, 13

Davis, M., Guhathakurta, P., Konidaris, N. P., et al. 2007, ApJL, 660, L1

Davis, M. & Peebles, P. J. E. 1983, ApJ, 267, 465

Davison, A. C. & Hinkley, D. V. 2013, Bootstrap Methods and Their Application (New York, NY, USA: Cambridge University Press)

Díaz-García, L. A., Cenarro, A. J., López-Sanjuan, C., et al. 2015, A&A, 582, A14

Dicke, R. H., Peebles, P. J. E., Roll, P. G., & Wilkinson, D. T. 1965, ApJ, 142, 414

Djorgovski, S. G., Mahabal, A., Drake, A., Graham, M., & Donalek, C. 2013, Sky Surveys, ed. T. D. Oswalt & H. E. Bond, 223

Dressler, A. 1980, ApJ, 236, 351

Driver, S. & De Propris, R. 2003, APSS, 285, 175

Dunlop, J. S., Guiderdoni, B., Rocca-Volmerange, B., Peacock, J. A., & Longair, M. S. 1989, MNRAS, 240, 257

Einstein, A. 1915, Sitzungsberichte der Königlich Preußischen Akademie der Wissenschaften (Berlin), Seite 778-786.

Einstein, A. 1917, Sitzungsberichte der Königlich Preußischen Akademie der Wissenschaften (Berlin), Seite 142-152.

Eisenstein, D. J., Zehavi, I., Hogg, D. W., et al. 2005, ApJ, 633, 560

Elston, R., Rieke, G. H., & Rieke, M. J. 1988, ApJL, 331, L77

Fazio, G. G., Hora, J. L., Allen, L. E., et al. 2004, ApJS, 154, 10

Ferguson, H. C., Dickinson, M., & Williams, R. 2000, ARA&A, 38, 667

Fernández-Soto, A., Lanzetta, K. M., & Yahil, A. 1999, ApJ, 513, 34

Fields, B. D. 2012, arXiv preprint arXiv:1203.3551

Foreman-Mackey, D., Hogg, D. W., Lang, D., & Goodman, J. 2013, PASP, 125, 306

Friedmann, A. 1922, Zeitschrift fur Physik, 10, 377

Galametz, A., Grazian, A., Fontana, A., et al. 2013, The Astrophysical Journal Supplement Series, 206, 10

Gamow, G. 1946, Physical Review, 70, 572

Gregg, M. D., Silva, D., Rayner, J., et al. 2004, in Bulletin of the American Astronomical Society, Vol. 36, American Astronomical Society Meeting Abstracts, 1496

Hamilton, A. J. S. 1993, ApJ, 417, 19

Hamilton, A. J. S. 1998, in Astrophysics and Space Science Library, Vol. 231, The Evolving Universe, ed. D. Hamilton, 185

Hawkins, E., Maddox, S., Cole, S., et al. 2003, MNRAS, 346, 78

Heckman, T. M. & Best, P. N. 2014, ARA&A, 52, 589

Huang, J.-S., Cowie, L. L., Gardner, J. P., et al. 1997, ApJ, 476, 12

Hubble, E. 1929, Proceedings of the National Academy of Science, 15, 168

Hubble, E. P. 1926, ApJ, 63

Humason, M. L. 1929, Proceedings of the National Academy of Science, 15, 167

Hurtado-Gil, L., Arnalte-Mur, P., Martínez, V. J., et al. 2016, ApJ, 818, 174

Ilbert, O., Arnouts, S., McCracken, H. J., et al. 2006, A&A, 457, 841

Ilbert, O., Capak, P., Salvato, M., et al. 2009, ApJ, 690, 1236

Kaiser, N. 1987, MNRAS, 227, 1

Kauffmann, G., White, S. D. M., Heckman, T. M., et al. 2004, MNRAS, 353, 713

Kerscher, M. 1999, A&A, 343, 333

Koo, D. C. 1985, AJ, 90, 418

Kovács, Z., Mall, U., Bizenberger, P., Baumeister, H., & Röser, H.-J. 2004, in SPIE Proc., Vol. 5499, Optical and Infrared Detectors for Astronomy, ed. J. D. Garnett & J. W. Beletic, 432–441

Labatie, A., Starck, J.-L., Lachièze-Rey, M., & Arnalte-Mur, P. 2010, ArXiv e-prints

Labbé, I., Franx, M., Rudnick, G., et al. 2003, AJ, 125, 1107

Landy, S. D. & Szalay, A. S. 1993, ApJ, 412, 64

Lanzetta, K. M., Yahil, A., & Fernández-Soto, A. 1996, Nat, 381, 759

Lawrence, A., Warren, S. J., Almaini, O., et al. 2007, MNRAS, 379, 1599

Leavitt, H. S. 1908, Annals of Harvard College Observatory, 60, 87

Lemaître, G. 1927, Annales de la Société Scientifique de Bruxelles, 47, 49

Lemaître, G. 1931, MNRAS, 91, 483

Lilly, S. J., Le Fevre, O., Hammer, F., & Crampton, D. 1996, ApJL, 460, L1

Lilly, S. J. & Longair, M. S. 1984, MNRAS, 211, 833

Lin, C. C. & Shu, F. H. 1964, ApJ, 140, 646

Lin, H., Yee, H. K. C., Carlberg, R. G., & Ellingson, E. 1997, ApJ, 475, 494

Longhetti, M. & Saracco, P. 2009, MNRAS, 394, 774

Lonsdale, C. J., Smith, H. E., Rowan-Robinson, M., et al. 2003, PASP, 115, 897

López-Sanjuan, C., Cenarro, A. J., Varela, J., et al. 2015, A&A, 576, A53

López-Sanjuan, C., Tempel, E., Benítez, N., et al. 2017, A&A, 599, A62

Loveday, J., Norberg, P., Baldry, I. K., et al. 2012, MNRAS, 420, 1239

Madau, P. & Dickinson, M. 2014, ARA&A, 52, 415

Madgwick, D. S., Hawkins, E., Lahav, O., et al. 2003, MNRAS, 344, 847

Madgwick, D. S., Lahav, O., Baldry, I. K., et al. 2002, MNRAS, 333, 133

Martínez, V. J. & Saar, E. 2002, Statistics of the Galaxy Distribution (Chapman)

Matute, I., Márquez, I., Masegosa, J., et al. 2012, A&A, 542, A20

Matute, I., Masegosa, J., Márquez, I., et al. 2013, A&A, 557, A78

McCracken, H. J., Milvang-Jensen, B., Dunlop, J., et al. 2012, A&A, 544, A156

Meneux, B., Guzzo, L., de la Torre, S., et al. 2009, A&A, 505, 463

Minkowski, R. & Abell, G. O. 1963, PASP, 75, 488

Moles, M., Benítez, N., Aguerri, J. A. L., et al. 2008, AJ, 136, 1325

Molino, A., Benítez, N., Moles, M., et al. 2014, MNRAS, 441, 2891

Mortlock, A., McLure, R. J., Bowler, R. A. A., et al. 2017, MNRAS, 465, 672

Murdin, P. 2001, Encyclopedia of astronomy and astrophysics

Muzzin, A., Marchesini, D., Stefanon, M., et al. 2013, ApJS, 206, 8

Nieves-Seoane, L., Fernandez-Soto, A., Arnalte-Mur, P., et al. 2017, MNRAS, 464, 4331

Norberg, P., Baugh, C. M., Gaztañaga, E., & Croton, D. J. 2009, MNRAS, 396, 19

Oke, J. B. & Gunn, J. E. 1983, ApJ, 266, 713

Oke, J. B. & Sandage, A. 1968, ApJ, 154, 21

Peacock, J. A., Cole, S., Norberg, P., et al. 2001, Nat, 410, 169

Peebles, P. J. E. 1980, The large-scale structure of the universe

Penzias, A. A. & Wilson, R. W. 1965, ApJ, 142, 419

Perlmutter, S., Aldering, G., Goldhaber, G., et al. 1999, ApJ, 517, 565

Ph.D., H. R. 1928, The London, Edinburgh, and Dublin Philosophical Magazine and Journal of Science, 5, 835

Planck Collaboration, Ade, P. A. R., Aghanim, N., et al. 2016, A&A, 594, A13

Pons-Bordería, M.-J., Martínez, V. J., Stoyan, D., Stoyan, H., & Saar, E. 1999, ApJ, 523, 480

Pović, M., Huertas-Company, M., Aguerri, J. A. L., et al. 2013, MNRAS, 435, 3444

Reid, I. N., Brewer, C., Brucato, R. J., et al. 1991, PASP, 103, 661

Riess, A. G., Filippenko, A. V., Challis, P., et al. 1998, AJ, 116, 1009

Robertson, B. E. 2010, ApJL, 716, L229

Robertson, H. P. 1933, Reviews of Modern Physics, 5, 62

Roche, N., Eales, S. A., Hippelein, H., & Willott, C. J. 1999, MNRAS, 306, 538

Rowan-Robinson, M., Lari, C., Perez-Fournon, I., et al. 2004, MNRAS, 351, 1290

Rowan-Robinson, M., Oliver, S., Efstathiou, A., et al. 1999, in ESA Special Publication, Vol. 427, The Universe as Seen by ISO, ed. P. Cox & M. Kessler, 1011

Sanders, D. B., Salvato, M., Aussel, H., et al. 2007, ApJS, 172, 86

Saracco, P., Fiano, A., Chincarini, G., et al. 2006, MNRAS, 367, 349

Sargent, W. L. W. & Turner, E. L. 1977, ApJL, 212, L3

Schechter, P. 1976, ApJ, 203, 297

Scoville, N., Abraham, R. G., Aussel, H., et al. 2007, ApJS, 172, 38

Sheth, R. K. & Rossi, G. 2010, MNRAS, 403, 2137

Simard, L., Willmer, C. N. A., Vogt, N. P., et al. 2002, ApJS, 142, 1

Slipher, V. M. 1917, The Observatory, 40, 304

Smith, R. E. 2012, MNRAS, 426, 531

Smoot, G. F., Bennett, C. L., Kogut, A., et al. 1992, ApJL, 396, L1

Stanford, S. A., Eisenhardt, P. R. M., & Dickinson, M. 1995, ApJ, 450, 512

Strasburger, D., Gorjian, V., Burke, T., et al. 2015, in American Astronomical Society Meeting Abstracts, Vol. 225, American Astronomical Society Meeting Abstracts, 336.26

Strateva, I., Ivezić, Ž., Knapp, G. R., et al. 2001, AJ, 122, 1861

Swanson, M. E. C., Tegmark, M., Hamilton, A. J. S., & Hill, J. C. 2008, MNRAS, 387, 1391, survey masks

Taylor, M. B. 2005, in Astronomical Society of the Pacific Conference Series, Vol. 347, Astronomical Data Analysis Software and Systems XIV, ed. P. Shopbell, M. Britton, & R. Ebert, 29

Troncoso Iribarren, P., Infante, L., Padilla, N., et al. 2016, A&A, 588, A132

Viironen, K., Marín-Franch, A., López-Sanjuan, C., et al. 2015, A&A, 576, A25

Whitaker, K. E., Labbé, I., van Dokkum, P. G., et al. 2011, ApJ, 735, 86

Williams, R. E., Blacker, B., Dickinson, M., et al. 1996, AJ, 112, 1335

Willman, B. & Strader, J. 2012, The Astronomical Journal, 144, 76

Wolf, C., Meisenheimer, K., Rix, H.-W., et al. 2003, A&A, 401, 73

Wright, E. L., Eisenhardt, P. R. M., Mainzer, A. K., et al. 2010, AJ, 140, 1868

Yang, G., Xue, Y. Q., Luo, B., et al. 2014, ApJS, 215, 27

York, D. G., Adelman, J., Anderson, Jr., J. E., et al. 2000, AJ, 120, 1579

Appendix A

The K_S-band catalogue structure

We list in this appendix (Table A.1) the items contained in our catalogue for each of the detected objects. We include more complete details on some of the items in the following paragraphs.

(a) The first column provides a unique ID for each source, built according to the following rule:

$$\underbrace{220}_{\mathrm{K_s-band}} + \underbrace{1}_{\mathrm{Field}} + \underbrace{1}_{\mathrm{Pointing}} + \underbrace{1}_{\mathrm{CCD}} + \underbrace{00001}_{\mathrm{SExtractor\ ID}}$$

(b) All fluxes and magnitudes have been measured using the isophotal method in SExtractor. In those cases where the measured flux is less than its associated uncertainty, the magnitude value has been set to 99.0 and the magnitude error corresponds to the 1σ limit.

(c) Colour-based stellarity as defined in Section 2.5.

(d) Indicates whether the object lies in the clean area after the mask described in Section 2.3 is applied.

(e) BPZ outputs the result of a pure maximum likelihood calculation of the photometric redshift, not including the type-luminosity-redshift Bayesian priors. We list in these columns such maximum likelihood-based best-fitting values, and the associated χ^2 value.

COLUMNS	CONTENT	TYPE
1	ID Number[a]	Integer
2,3	(X,Y) pixel coordinates	Real
4,5	RA, Dec (J2000)	Real
6	Area (pixels)	Integer
7,8	F365W flux, error[b]	Real
9,10	F365W magnitude, error[b]	Real
...	...	...
95,96	K_s flux, error[b]	Real
97,98	K_s magnitude, error[b]	Real
99,100	Synth F814W flux, error[b]	Real
101,102	Synth F814W magnitude, error[b]	Real
103	SExtractor `FLAG`	Integer
104	SExtractor `CLASS_STAR`	Real
105	`COLOUR_CLASS_STAR`[c]	Real
106	`MASK_SELECTION`[d]	Boolean
107	BPZ photometric redshift	Real
108,109	BPZ photo-z 95% interval	Real
110	BPZ SED type	Real
111	BPZ *Odds*	Real
112	BPZ stellar mass ($\log_{10}$, $M_\odot$)	Real
113	BPZ absolute $B_{\rm Johnson}$	Real
114	BPZ ML photo-z[e]	Real
115	BPZ ML SED type[e]	Real
116	BPZ fitting χ^2 [e]	Real
117	Absolute K_s	Real

Table A.1: Content and type of the columns in the catalogue files.

Appendix B

AK_S+IR catalogue structure

We list in this Appendix (Table B.1) the items contained in our catalogue for each of the detected objects. We include more complete details on some of the items in the following paragraphs.

(a) The first column provides a unique ID for each source, built according to the following rule:

$$\underbrace{220}_{\mathrm{K_s-band}} + \underbrace{1}_{\mathrm{Field}} + \underbrace{1}_{\mathrm{Pointing}} + \underbrace{1}_{\mathrm{CCD}} + \underbrace{00001}_{\mathrm{SExtractor\ ID}}$$

(b) All fluxes and magnitudes have been measured using the isophotal method in SExtractor. In those cases where the measured flux is less than its associated uncertainty, the magnitude value has been set to 99.0 and the magnitude error corresponds to the 1σ limit.

(c) Colour-based stellarity as defined in Section 2.5.

(d) Indicates whether the object lies in the clean area after the mask described in Section 2.3 is applied.

(e) BPZ outputs the result of a pure maximum likelihood calculation of the photometric redshift, not including the type-luminosity-redshift Bayesian priors. We list in these columns such maximum likelihood-based best-fitting values, and the associated χ^2 value.

(f) The fluxes and magnitudes for the IRAC bands, selected from the public IRAC channels data available in the areas overlapping ALHAMBRA.

COLUMNS	CONTENT	TYPE
1	ID Number[a]	Integer
2,3	(X,Y) pixel coordinates	Real
4,5	RA, Dec (J2000)	Real
6	Area (pixels)	Integer
7,8	F365W flux, error[b]	Real
9,10	F365W magnitude, error[b]	Real
...	...	...
95,96	K_s flux, error[b]	Real
97,98	K_s magnitude, error[b]	Real
99,100	Synth F814W flux, error[b]	Real
101,102	Synth F814W magnitude, error[b]	Real
103	SExtractor `FLAG`	Integer
104	SExtractor `CLASS_STAR`	Real
105	`COLOUR_CLASS_STAR`[c]	Real
106	`MASK_SELECTION`[d]	Boolean
107,108	IRAC channel 1 flux,error[f]	Real
109,110	IRAC channel 1 magnitude,error[f]	Real
...	...	...l
115,116	IRAC channel 3 flux,error[f]	Real
117,118	IRAC channel 3 magnitude,error[f]	Real
107	BPZ photometric redshift	Real
108,109	BPZ photo-z 95% interval	Real
110	BPZ SED type	Real
111	BPZ *Odds*	Real
112	BPZ stellar mass ($\log_{10}$, $M_\odot$)	Real
113	BPZ absolute $B_{\rm Johnson}$	Real
114	BPZ ML photo-z[e]	Real
115	BPZ ML SED type[e]	Real
116	BPZ fitting χ^2 [e]	Real

Table B.1: Content and type of the columns in the catalogue files.

Appendix C

The ALHAMBRA+IRAC luminosity functions

We present in this Appendix (Tables C.1 and C.2) the values of the ALHAMBRA K_s+IRAC luminosity functions. The data was performing using a Δz= 0.2 and ΔM_{K_s}= 0.3, for blue-type galaxies table C.1 and for red-type galaxies table C.2.

$0.25 \leq z < 0.75$		$0.75 \leq z < 1.25$		$1.25 \leq z < 1.75$		$1.75 \leq z < 2.25$	
$\langle M_{K_s} \rangle$	$\log_{10}\Phi$	$\langle M_{K_s} \rangle$	$\log_{10}\Phi$	$\langle M_{K_s} \rangle$	$\log_{10}\Phi$	$\langle M_{K_s} \rangle$	$\log_{10}\Phi$
-24.48	-5.55±0.57	-24.80	-5.33±0.23	-25.09	-5.63±0.26	-25.10	-5.00±0.09
-24.19	-4.98 ±0.24	-24.52	-4.78±0.10	-24.82	-4.85 ± 0.10	-24.84	-4.55 ±0.05
-23.63	-4.45 ±0.11	-24.23	-4.31±0.06	-24.53	-4.52 ± 0.06	-24.53	-4.27 ± 0.05
-23.34	-3.96 ± 0.06	-23.93	-3.95 ± 0.05	-24.24	-4.15 ± 0.04	-24.24	-3.95 ± 0.03
-23.92	-3.58 ± 0.04	-23.64	-3.66 ± 0.04	-23.94	-3.90 ± 0.03	-23.96	-3.77 ± 0.03
-23.04	-3.36 ± 0.04	-23.33	-3.48 ± 0.03	-23.64	-3.72 ± 0.03	-23.72	-3.75 ± 0.04
-22.74	-3.26 ± 0.03	-23.04	-3.34 ± 0.02	-23.36	-3.64 ± 0.03	···	···
-22.45	-3.19 ± 0.03	-22.75	-3.22 ± 0.02	-23.06	-3.54 ± 0.03	···	···
-22.15	-3.07 ± 0.03	-22.45	-3.18 ± 0.01	-22.77	-3.29 ± 0.03	···	···
-21.84	-2.98 ± 0.02	-22.16	-3.14 ± 0.02	-22.57	-3.25 ± 0.04	···	···
-21.55	-2.94 ± 0.02	-21.86	-3.11 ± 0.02	···	···	···	···
-21.25	-2.90 ± 0.02	-21.57	-3.05 ± 0.04	···	···	···	···
-20.96	-2.85 ± 0.02	-21.32	-3.02 ± 0.03	···	···	···	···
-20.65	-2.77 ± 0.02	···	···	···	···	···	···
-20.36	-2.69 ± 0.02	···	···	···	···	···	···
-20.06	-2.70 ± 0.03	···	···	···	···	···	···
-19.75	-2.66 ± 0.03	···	···	···	···	···	···
-19.46	-2.59 ± 0.03	···	···	···	···	···	···
-19.17	-2.61 ± 0.05	···	···	···	···	···	···
-18.87	-2.59 ± 0.06	···	···	···	···	···	···
-18.65	-2.35 ± 0.09	···	···	···	···	···	···

Table C.1: ALHAMBRA K_s+IRAC luminosity function for blue-type Sample $\Phi(z, M_{K_s}|BT)$

$0.25 \leq z < 0.75$		$0.75 \leq z < 1.25$		$1.25 \leq z < 1.75$		$1.75 \leq z < 2.25$	
-24.80	-5.56 ± 1.21	-25.06	-6.66 ± 0.92	-25.35	-9.92 ± 0.82	-25.36	-6.93 ± 0.29
-24.48	-4.79 ± 0.16	-24.80	-5.14 ± 0.16	-25.09	-6.24 ± 0.31	-25.10	-5.37 ± 0.11
-24.19	-4.18 ± 0.08	-24.52	-4.65 ± 0.09	-24.82	-5.04 ± 0.10	-24.84	-4.76 ± 0.07
-23.92	-3.83 ± 0.05	-24.23	-4.19 ± 0.06	-24.53	-4.51 ± 0.05	-24.53	-4.50 ± 0.06
-23.63	-3.57 ± 0.04	-23.93	-3.78 ± 0.04	-24.24	-4.23 ± 0.05	-24.24	-4.17 ± 0.04
-23.34	-3.37 ± 0.03	-23.64	-3.62 ± 0.04	-23.94	-3.89 ± 0.03	-23.96	-3.97 ± 0.04
-23.04	-3.24 ± 0.04	-23.33	-3.50 ± 0.03	-23.64	-3.76 ± 0.03	-23.72	-3.84 ± 0.04
-22.74	-3.19 ± 0.03	-23.04	-3.40 ± 0.02	-23.36	-3.67 ± 0.03	···	···
-22.45	-3.14 ± 0.03	-22.75	-3.38 ± 0.02	-23.06	-3.59 ± 0.03	···	···
-22.15	-3.20 ± 0.03	-22.45	-3.40 ± 0.02	-22.77	-3.60 ± 0.04	···	···
-21.84	-3.22 ± 0.03	-22.16	-3.37 ± 0.03	-22.57	-3.55 ± 0.05	···	···
-21.55	-3.27 ± 0.03	-21.86	-3.36 ± 0.03	···	···	···	···
-21.25	-3.34 ± 0.03	-21.57	-3.47 ± 0.05	···	···	···	···
-20.96	-3.34 ± 0.04	-21.32	-3.46 ± 0.07	···	···	···	···
-20.65	-3.40 ± 0.04		···	···	···	···	···
-20.36	-3.33 ± 0.05	···	···	···	···	···	···
-20.06	-3.38 ± 0.06	···	···	···	···	···	···
-19.75	-3.47 ± 0.08	···	···	···	···	···	···
-19.46	-3.31 ± 0.09	···	···	···	···	···	···
-19.17	-3.14 ± 0.10	···	···	···	···	···	···
-18.87	-3.11 ± 0.10	···	···	···	···	···	···
-18.65	-3.01 ± 0.09	···	···	···	···	···	···

Table C.2: ALHAMBRA K_s+IRAC luminosity function for blue-type Sample $\Phi(z, M_{K_s}|RT)$

Appendix D

Resumen en castellano: Catálogo en banda K_s de ALHAMBRA

D.1 Introducción

La formación y evolución de las galaxias en el Universo visible es uno de los principales temas de investigación en la astronomía actual. Parece lógico empezar esta introducción definiendo los objetos que estudiaremos en esta Tesis: las galaxias.

Una galaxia es una colección de estrellas cuyas propiedades no pueden ser explicadas por la combinación de bariones (o materia ordinaria) y las leyes de gravitación de Newton (Willman & Strader 2012). Cómo se formaron las galaxias en el Universo temprano, cómo han evolucionado, cómo se clasifican según su aspecto o sus propiedades físicas, y cómo podemos entender las estructuras que forman en el Universo, son preguntas fundamentales para el avance en la astronomía y cosmología más reciente.

La clasificación morfológica de las galaxias está basada en su aspecto exterior. Esta clasificación es muy sencilla, en tanto en cuanto se sigue utilizando la clasificación propuesta por Edwin Hubble en la década de los años 30. El diapasón de Hubble recoge en un sencillo esquema la morfología de la gran mayoría de las

galaxias en el universo local. Este esquema separa las galaxias en dos grandes grupos: galaxias elípticas y galaxias espirales. Hubble pensaba que esta clasificación en elípticas y espirales también guardaba un orden cronológico relacionado con su estado de evolución. Según este estado, los objetos más jóvenes en el universo y menos evolucionados eran elípticos, mientras que los objetos más tardíos en el universo y más evolucionados eran espirales. Esta idea errónea de Hubble, daría lugar al equívoco de llamar galaxias tempranas a las elípticas y galaxias tardías a las espirales, nombres que todavía se siguen utilizando hoy. Además de estos dos grandes grupos, Hubble añadió un tercer grupo que engloba a las galaxias irregulares. En este último grupo se añadieron todas aquellas galaxias que no se ajustaban a las descripciones de elípticas o espirales.

Las diferencias entre galaxias no sólo se encuentran en su forma, también es posible establecer una clasificación bimodal teniendo en cuenta algunas de sus propiedades físicas comunes, y que en serendipia, se superpone con los dos tipos morfológicos descritos en el diapasón de Hubble: elípticas y espirales.

- Galaxias elípticas: Se caracterizan por sus isofotas elipsoidales. No rotan de manera solidaria en un disco alrededor de un centro, sino que tienen una gran velocidad de dispersión directamente relacionada con la masa total de la galaxia. Apenas contienen gas o polvo, lo que implica una baja tasa de formación estelar. Las estrellas más abundantes en estas galaxias son viejas, con un espectro rojo y ricas en metales. La abundancia de este tipo de estrellas es lo que hace que su espectro sea más brillante en las bandas más rojas comparado con su brillo en las bandas azules (Madau & Dickinson 2014). Este tipo de galaxias son generalmente las más masivas y se encuentran más frecuentemente en las zonas más densas del universo, particularmente en los centros de los cúmulos de galaxias.

- Galaxias espirales: Tienen una morfología más compleja que las elípticas. Estas galaxias se formaron por la rotación sostenida en un disco, en el cual se incluyen los brazos espirales. La región central la ocupa un núcleo, cuyo perfil ajusta a un tipo elíptico. A menudo nos encontramos en las galaxias que observamos que en el núcleo se distingue una barra. En las regiones centrales la población de estrellas está más envejecida. Estas galaxias son ricas en gas y polvo lo que propicia, junto a la dinámica de los brazos

espirales (Lin & Shu 1964), la formación de nuevas estrellas. La presencia de estrellas de corta vida, muy masivas y muy luminosas, hace que los brazos de las espirales sean estructuras visibles dentro de los discos. Al contrario de lo que ocurría con las galaxias elípticas, las galaxias espirales poseen una población de estrellas más joven. Esto conlleva que la luz emitida por estas fuentes esté dominada por una población estelar más azul. Estas galaxias se observan en regiones del universo poco densas, y su numero decrece significativamente conforme nos acercamos a las zonas centrales de los grandes cúmulos de galaxias.

Teniendo en cuenta la banda en la que cada tipo de galaxia es más brillante, usualmente se denominan galaxias rojas a las galaxias elípticas y galaxias azules a las galaxias espirales. Este brillo en diferentes bandas es debido al tipo de población estelar más abundante en la galaxia. Este comportamiento bimodal se puede apreciar claramente en los diagramas color-color. En estos diagramas se distinguen dos regiones bien diferenciadas: la nube de galaxias azules y la nube de galaxias rojas. El mismo efecto puede observarse en los diagramas color-magnitud, donde una tira estrecha está ocupada por las galaxias rojas (o elípticas), denominada *secuencia roja*, y una región más ancha está ocupada por galaxias espirales (o azules), en la denominada *nube de las azules*.

Para entender mejor la formación y evolución de las galaxias es necesario evaluar los procesos físicos que tienen lugar en el Universo observable a diferentes edades. Gracias al límite impuesto por la velocidad de la luz los fotones procedentes de los objetos a diferentes distancias en el universo que nos llegan hoy nos dan información de cómo eran estos objetos en el momento en el que la luz fue emitida. De esta manera es posible obtener una imagen del universo a cada *redshift* y por tanto, a edades diferentes. Esta "línea del tiempo" nos permite estudiar cómo las propiedades de las galaxias han evolucionado hasta el presente. Este análisis requiere observaciones de grandes muestras de galaxias, que cubran un gran rango de *redshift* en un área significativa del cielo. Esto es, se requieren grandes *surveys* astronómicos.

D.2 *Surveys* astronómicos.

Los *surveys* astronómicos son uno de los elementos clave en el avance de nuestro conocimiento de los objetos celestes. Desde tiempos inmemoriales los astrónomos han buscado estrellas en el cielo, estudiando sus propiedades básicas, posicionándolas en la bóveda celeste y midiendo su brillo aparente. La observación directa de los objetos astronómicos sólo proporciona información sobre su posición proyectada en el cielo en dos dimensiones. Para describir cómo los objetos astronómicos se distribuyen en el universo tridimensional, los astrónomos han tenido que hacer mapas de estos objetos añadiendo una tercera coordenada, que permite medir la distancia a estos objetos con precisión. En el caso particular de la cosmología, se utiliza el *redshift* espectral como estimador de la distancia.

La tarea de posicionar en tres dimensiones los objetos en el Universo se incrementó de manera exponencial en el último siglo. Este incremento es debido a las sucesivas renovaciones de telescopios, con estructuras cada vez más grandes y óptica más sofisticada, con la llegada de las placas fotográficas y, sobre todo, con la llegada de los detectores electrónicos. En las últimas décadas, la complejidad de estos dispositivos creció enormemente, debido fundamentalmente a la introducción en la astronomía del uso de computadoras con gran capacidad de procesado y almacenamiento de datos, y también a la introducción de detectores digitales capaces de manejar grandes cantidades de datos.

Estos avances en la tecnología permitieron que el procesado de enormes cantidades de datos astronómicos se redujera a un tiempo razonable. Comenzó la era de los *surveys* astronómicos masivos.

Los *surveys* astronómicos permitieron indagar en un gran rango de objetivos científicos, entre los que destacan i) posicionar un gran número de objetos para medir la estructura y apariencia del universo observable, y ii) obtener muestras lo suficientemente grandes como para poder hacer análisis estadísticos a diferentes *redshifts*, y así poder caracterizar los procesos astrofísicos y describir la estructura a gran escala de la materia bariónica y la manera en la que evoluciona.

En nuestro tiempo algunos de los *surveys* astronómicos más relevantes han tenido como principal objetivo cubrir fracciones del cielo cada vez más grandes, y con más profundidad en la fotometría e información del espectro. Hasta el momento (y todo parece apuntar que en el futuro más inmediato), ningún proyecto ha

conseguido cubrir satisfactoriamente estas dos dimensiones de manera simultánea. Por ejemplo, el Sloan Digital Sky Survey (SDSS, York et al. 2000) o el Two Degree Field Galaxy Redshift Survey (2dFGRS, Colless et al. 2001) han obtenido información espectral para $\sim 10^5$–10^6 objetos cada uno, observando grandes áreas (aproximadamente 1/4 de todo el cielo), hasta un límite relativamente profundo, con magnitudes aparentes $AB \approx 19$. Su contrapartida fotométrica cubre áreas similares en el cielo, pero pueden detectar fuentes hasta 10 veces menos luminosas, típicamente con magnitudes aparentes $AB \approx 21$–22.

Por otra parte podemos hablar de los *surveys* cuyas imágenes han sido tomadas desde el espacio. Estos *surveys* pueden ser muy profundos, como por ejemplo los Hubble Deep Fields (Ferguson et al. 2000). Este tipo de análisis cubre pequeñas áreas en el cielo (del orden de 10^{-3} grados cuadrados, o incluso menos), pero incluye espectroscopía de magnitudes$AB \approx 25$–26 y fotometría multibanda de magnitudes $AB \approx 28$ o incluso más.

Otro aspecto que define a los *surveys* cosmológicos es su completitud espectral. En el comienzo de esta nueva forma de procesar la información astronómica, *surveys* como el del Palomar Observatory Sky Survey (POSS, Minkowski & Abell 1963; Reid et al. 1991), incluían información únicamente en dos bandas diferentes, o lo que es lo mismo, obtenían un color para cada objeto. Por otra parte, los *surveys* espectroscópicos incluían un espectro completo en cada observación, lo que implicaba obtener información de la formación estelar del objeto, su la masa, su metalicidad, etc. Desde la llegada de los Hubble Deep Fields (Ferguson et al. 2000) y otros *surveys* a finales del pasado siglo, se ha convertido en una práctica común obtener imágenes en multitud de filtros tanto en el rango óptico como en el rango infrarrojo. Con estas medidas se conseguía medir algunas de las propiedades espectrales, las cuales permitían tener una estimación básica de algunas de las cantidades físicas para las que, de otro modo, sería necesario obtener un análisis espectral. El uso de las técnicas fotométricas ha crecido hasta convertirse en un estándar, gracias a sus buenos resultados (Fernández-Soto et al. 1999; Benítez 2000; Bolzonella et al. 2000).

A lo largo de lo últimos años, algunos *surveys* han sido diseñados explícitamente para optimizar el análisis fotométrico multibanda. Ejemplos de estos trabajos son COMBO-17 (Wolf et al. 2003), ALHAMBRA (Moles et al. 2008) o el recientemente puesto en funcionamiento J-PAS (Benitez et al. 2014).

Survey	ÁREA	Magnitud AB (límite 5σ)
MUSYC	0.015 deg^2	$K_s \approx 22.5$
NMBS	0.44 deg^2	$K \approx 24.2$
UKIDSS-UDS	0.77 deg^2	$K \approx 24.6$
WIRCDS	2.03 deg^2	$K_s \approx 24.0$
UVISTA	1.50 deg^2	$K_s \approx 23.8$
ALHAMBRA K_s-band	2.47 deg^2	$K_s \approx 21.5$

Table D.1: Comparación entre *surveys* fotométricos que utilizan la banda K como imagen de referencia para realizar la fotometría utilizando varias bandas.

D.3 Motivación de esta Tesis

Las galaxias tempranas dominan el extremo brillante de la función de luminosidad a *redshift* bajo y moderado (Lin et al. 1997). En particular en estos *redshifts* se encuentran las galaxias más masivas que habitan el Universo, en las regiones de mayor densidad. Estas galaxias representan los objetos más evolucionados y masivos en la segunda mitad de la edad del Universo, y su estudio es fundamental para entender cómo sucedió la formación estelar y su relación con otros procesos cósmicos, como son: la formación y evolución de los agujeros negros, cúmulos de galaxias y la formación de estructuras a gran escala, las interacciones galácticas, la fusión entre galaxias y los fenómenos relacionados con los núcleos activos de galaxias (AGNs). Debido a sus colores rojos intrínsecos, las galaxias tempranas están infrarrepresentadas por causa del límite en magnitud de los *surveys* que principalmente detectan en el rango óptico. Precisamente en estos rangos de *redshift* el salto de Balmer y su absorción asociada, característico a $\lambda \sim 4000$, está desplazado hacia el rojo fuera de la banda de detección haciendo que las galaxias dejen de observarse en las bandas ópticas. En los últimos años, el desarrollo de varios *surveys* que detectan objetos en bandas cercanas al infrarrojo cercano (NIR), ha ayudado significativamente en el análisis de la evolución de galaxias de tipo temprano a *redshift* moderado y alto, por ejemplo: Newfirm Medium Band Survey (NMBS, Whitaker et al. 2011), UKIDSS-Ultra Deep Survey (Lawrence et al. 2007), WIRCam Deep Survey (WIRCDS, Bielby et al. 2012), y Ultra VISTA (McCracken et al. 2012; Muzzin et al. 2013).

En el caso particular del *survey* ALHAMBRA, la detección se realiza sobre una imagen sintética que emula el filtro F814W del Telescopio Espacial Hubble. Este efecto de selección crea un sesgo en contra las galaxias rojas que comienza a notarse en $z \approx 0,8$, y es dominante en $z \geq 1.1$, como ya se ha observado en el trabajo de Arnalte-Mur et al. (2014). Una distribución de energía espectral (SED) típica de tipo temprano a $z \approx 0.8$ tiene un color $(I - K_s) \approx 1.8$, mientras que la misma galaxia en $z \approx 1.4$ muestra un color $(I-K_s) \approx 3.1$, y alcanza $(I-K_s) \geq 4.5$ a *redshift* $z = 2$. Esto significa que, incluso si la imagen de detección óptica es (como en el caso de ALHAMBRA) más profunda que la correspondiente banda K_s, al menos parte de la incompletitud producida por los efectos de selección puede ser evitada usando la banda K_s como imagen de detección.

En esta Tesis presentamos el catálogo de galaxias seleccionado en la banda K_s del *survey* ALHAMBRA. Este catálogo se ha compilado con el fin de superar parcialmente el sesgo de selección descrito anteriormente. Con él, podremos ampliar algunas de las tareas que ya se han realizado con los datos de ALHAMBRA a *redshifts* $z > 1$.

La organización de la Tesis es la siguiente:

- En el Capítulo 2 presentamos el *survey* ALHAMBRA y describimos en detalle la construcción del catálogo en la banda K_s .

- En el Capítulo 3 presentamos el catálogo y sus propiedades. También incluimos una breve discusión de algunas aplicaciones inmediatas del catálogo, con particular atención a cómo su uso será importante para completar (ya sea en *redshift* o en términos de tipos de galaxias) algunos de los análisis que ya han sido publicados, basados en el catálogo óptico de ALHAMBRA. Describimos en este capítulo el método seguido en Arnalte-Mur et al. (2014) para recuperar la función de correlación del espacio real y aplicarla a nuestra muestra. También mostramos y discutimos los resultados obtenidos para el catálogo ALHAMBRA K_s -band.

- En el Capítulo 4 presentamos los resultados obtenidos del análisis del cruce de datos entre el catálogo de K_s band y los datos de Spitzer / IRAC, en aquellos campos que tengan área que solape con alguno de los campos de ALHAMBRA. Presentamos la función de luminosidad en la banda K_s para

el área superpuesta y discutimos los resultados comparándolos con otros trabajos similares.

- Terminamos en el Capítulo 5 con las conclusiones de nuestra Tesis y una breve descripción del trabajo futuro.

D.4 Conclusiones de la Tesis y trabajo futuro

En esta Tesis hemos presentado el catálogo fotométrico de las fuentes detectadas en las imágenes en banda K_s del *survey* ALHAMBRA. El catálogo incluye la fotometría en 20 bandas en el rango óptico, 3 bandas JHK_s en el rango infrarrojo y la fotometría de la banda sintética $F814$ de un total de 94.182 fuentes distribuidas en siete campos, cubriendo un área total de 2.47 deg ^{2}.

Este catálogo es diferente del catálogo óptico de ALHAMBRA presentado en Molino et al. (2014), ya que aquella muestra fue seleccionada en base a la imagen sintética F814W, similar a una selección en la banda I. Esta selección está sesgada en contra de las galaxias intrínsecamente rojas a *redshift* $z \gtrsim 1$, un efecto que se hizo notorio en varios de los trabajos recientes basados en el *survey* ALHAMBRA. Este problema despertó nuestro interés en producir un nuevo catálogo con el que se evitaría este sesgo seleccionando en la banda más roja disponible, es decir, la banda K_s.

La detección de las fuentes y la fotometría se realizó utilizando el *software* SExtractor en modo dual. Estimamos los errores fotométricos utilizando el método presentado por Labbé et al. (2003), utilizamos una versión adaptada de las máscaras creadas en el trabajo de Arnalte-Mur et al. (2014), y definimos nuestra propia área de detección. La separación galaxia-estrella se realizó usando un diagrama color-color, y se añadieron al estudio los SEDs de la biblioteca estelar Next Generation Spectral Library NGSL (HST/STIS NGSL, Gregg et al. 2004). Calculamos las funciones de completitud detalladas para cada apuntado utilizando el catálogo UltraVISTA como referencia, ya que su límite en magnitud es más profundo. Comparamos las fuentes detectadas en UltraVISTA con las fuentes en el área de solapamiento con ALHAMBRA, esto es, con el campo ALHAMBRA-4 / COSMOS. Aplicamos estas funciones de completitud para extender nuestro límite de magnitud y el número cuentas a magnitud $K_s \approx 21.9$. Para verificar la exacti-

tud fotométrica de nuestro catálogo se realizaron dos evaluaciones independientes: una prueba interna comparando la fotometría de los objetos comunes a nuestro catálogo y el catálogo original ALHAMBRA presentado en M14, y una prueba externa utilizando los objetos comunes a nuestro catálogo y UltraVISTA. En ambos casos se ha demostrado que la precisión del catálogo cruzado es compatible con la esperada en las respectivas incertidumbres, y sin ningún sesgo significativo.

Completamos nuestro catálogo ejecutando el código BPZ2.0 sobre nuestra muestra, incluyendo la opción de re-calibración fotométrica del punto cero, que utiliza una muestra con *redshifts* espectroscópicos para refinar, al mismo tiempo, tanto la fotometría como la precisión del *redshift* fotométrico. Usando una muestra de *redshifts* espectroscópicos con 3736 galaxias, y la desviación absoluta mediana normalizada (NMAD en sus siglas en inglés) como estimador de la precisión de nuestros resultados, obtenemos $\sigma_{\rm NMAD} = 0.011$ y una tasa de errores catastróficos (*catastrophic errors*) $\eta_1 \sim 1.3\%$, ambos comparables a los obtenidos por Molino et al. (2014). Se realizó una segunda comparación, en este caso con los *redshifts* fotométricos en el catálogo seleccionado de ALHAMBRA F814W. En esta comparación obtuvimos una $\sigma_{\rm NMAD} = 0.009$ con una tasa de errores catastróficos $\eta_1 \sim 0.58\%$. Como se esperaba, debido a la motivación de nuestro trabajo, la distribución del *redshift* fotométrico segregada por tipo de galaxia muestra que muchas de las nuevas fuentes K_s seleccionadas llenan la escasez de galaxias de tipo temprano en la muestra seleccionada en la banda F814W y para un *redshift* $z \gtrsim 1$.

Hemos estudiado las propiedades de agrupamiento de galaxias de tipo rojo en el rango de *redshift* $0.75 < z < 1.45$, extendiendo el trabajo realizado en Hurtado-Gil et al. (2016). Hemos utilizado el mismo método descrito por (Arnalte-Mur et al. 2014) para estimar la función de correlación proyectada $w_p(r_p)$. En primer lugar, hemos seleccionado las galaxias con los valores de los parámetros proporcionados por BPZ2.0: el parámetro tipo de galaxia $T_b < 5.5$ y el parámetro de estimación de la precisión $Odds > 0.5$. Además hemos establecido un límite en la magnitud $K_s < 21.0$, con el fin de obtener una muestra homogénea en términos de profundidad en magnitud aparente. Bajo estas restricciones hemos obtenido una muestra con 13 702 galaxias cubriendo un área $A_{eff} = 2.46$ deg ^{2}.

Para estudiar la evolución y la dependencia de la luminosidad del agrupamiento de las galaxias de tipo rojo hemos dividido en rangos, tanto en red-

shift z como en magnitud absoluta M_B, la muestra obtenida. Hemos definido las submuestras de galaxias en tres rangos de desplazamiento al rojo, y en cada uno de ellos hemos definido submuestras limitadas por diferentes umbrales de luminosidad en la banda B.

Hemos modelado la función de correlación usando una ley de potencias y hemos aplicando esta relación a la función de correlación proyectada $w_p(r_p)$ en función de los parámetros r_0 y *gamma*, añadiendo el término de *bias* obtenido a partir de la *integral constrain*. Hemos estudiado la función de correlación proyectada de cada una de las submuestras en el rango de distancias $r_p \sim 0.1\,h^{-1}$ Mpc a $r_p \sim 12\,h^{-1}$ Mpc . La función de correlación para las submuestras ha sido también ajustada por una ley de potencias. En los resultados obtenidos se han observado los efectos de la evolución en función del *redshift*. Especialmente cuando se comparan los *redshifts* extremos, la muestra de galaxias a alto *redshift* está más agrupada que la de bajo *redshift*. Los resultados también muestran la evolución de la luminosidad en la muestra a *redshift* más alto. Además, hemos estudiado el comportamiento de los parámetros de mejor ajuste r_0 y γ. Llegamos a la conclusión de que la pendiente γ es casi constante en los rangos de *redshift* considerados y hay una evolución en el *redshift* para el parámetro r_0. Añadimos los puntos calculados en el trabajo de Hurtado-Gil et al. (2016), y confirmamos la tendencia obtenida en nuestros datos para luminosidades más bajas. Presentaremos un análisis detallado de la función de correlación para las galaxias de tipo rojo en un próximo manuscrito.

Con el fin de extender la fotometría en el rango infrarrojo hemos cruzado nuestro catálogo con los datos públicos de la cámara de infrarrojos del Telescopio Espacial Spitzer (IRAC, Fazio et al. 2004). Las imágenes tomadas con este instrumento suponen añadir nuevos datos fotométricos en cuatro bandas centradas en 3.6, 4.5, 5.8 y 8.0μm. Hemos encontrado contrapartidas de IRAC para las fuentes incluidas en el catálogo en banda K_s en los campos: ALHAMBRA-2 con Spitzer Enhanced Imaging Products (SEIP) (Strasburger et al. 2015), ALHAMBRA-4 con COSMOS Spitzer (S-COSMOS) *survey*(Sanders et al. 2007), ALHAMBRA-6 con el Extended Groth Strip (EGS) (Barmby et al. 2008) y ALHAMBRA-7 con el campo ELAIS-N1 (Lonsdale et al. 2003).

Hemos realizado un test de la fotometría comparando los resultados obtenidos en Barro et al. (2011) y hemos comparado los datos observados con las *templates*

de ALHAMBRA con diferentes desplazamientos al rojo en los diagramas color-color. En ambas pruebas se confirma la consistencia de la fotometría del catálogo. Antes de obtener el catálogo fotométrico final hemos realizado una prueba previa con BPZ2.0. Los resultados obtenidos demostraron que mejoramos los resultados de BPZ2.0 para las estimaciones fotométricas del desplazamiento al rojo, evitando la fotometría de canal de $8.0\,\mu m$ IRAC. Finalmente tenemos el catálogo ALHAMBRA K_s + IRAC (A K_s -IR) que incluye la fotometría de 20+3 filtros ALHAMBRA-K_s, la banda sintética $F814W$ y las bandas de IRAC 3.6, 4.5 y 5.8 μm. El catálogo contiene todas las fuentes detectadas en el catálogo en banda K_s en el área superpuesta, obteniendo 36 024 fuentes en un área total de 0.93 deg^2.

Como ya habíamos realizado con el catálogo Ks seleccionado, completamos el catálogo fotométrico A K_s -IR ejecutando el código BPZ2.0 sobre nuestra muestra, incluida la opción de recalibración fotométrica, la cual se usa una muestra espectroscópica de redshift para mejorar la precisión de los *redshift* fotométricos . Utilizando una muestra de galaxias con contrapartida en el catálogo espectroscópico, tenemos un sample con 2860 galaxias y hemos obtenido $\sigma_{\rm NMAD} = 0.018$ y una tasa de errores catastróficos $\eta_1 \sim 4,96\%$. A pesar de que hemos aumentado la información en el rango espectral, los resultados obtenidos son ligeramente peores. Hemos realizado una prueba para evaluar el comportamiento de los *templates* de BPZ2.0 en el rango IR. Los resultados mostraron que había una discrepancia entre los datos observados y los *templates* de las galaxias de tipo azul a bajo *redshift* en el IR. Hemos llegado a la conclusión de que es precisamente en las bandas IRAC a bajo *redshift* cuando los efectos de polvo en las galaxias con formación estelar comienzan a ser más significativos. Otra cuestión es que en ese rango espectral los templates de BPZ2.0 no han sido optimizados. Esperamos que estos efectos se tengan en cuenta en versiones posteriores de BPZ.

Finalmente hemos calculado la función de luminosidad en la banda K_s utilizando los datos incluidos en el catálogo AK_s -IR. Hemos calculado los datos utilizando el método propuesto por López-Sanjuan et al. (2017). El método consiste en medir la función de luminosidad en la banda K_s para ambos tipos de galaxias rojas y azules, usando la función de distribución de probabilidad (PDF) en un espacio 2D, definido por el *redshift* z y el tipo espectral T para cada fuente, obtenida del análisis BPZ2.0. Con las PDF (z, T) se pasa a un nuevo espacio PDF (z, M_{K_s}), lo que nos permite obtener el valor de la función de luminosidad

en la banda K_s para cada tipo de galaxia.

Modelamos la función de luminosidad en banda K_s usando: i) una sola función de Schechter (Schechter 1976) para la muestra de galaxias de tipo azul y ii) una doble función de Schechter para la muestra de tipo rojo. Hemos comparado los valores obtenidos para diferentes rangos de *redshift* con los resultados incluidos en Arnouts et al. (2005a) y en Cirasuolo et al. (2010). Los resultados del modelado están de acuerdo con los datos obtenidos en Cirasuolo et al. (2010) para ambas muestras de tipo galaxia. Un tercer análisis se realizó utilizando la muestra completa, con el fin de comparar los resultados con otros trabajos recientes encontrados en la literatura como Mortlock et al. (2017) y Cirasuolo et al. (2010). En todos los rangos de *redshift* nuestros datos estaban de acuerdo con los datos de estos dos trabajos.

Como última parte de este trabajo, hemos presentado la evolución del los parámetros que describen el ajuste de función de Schechter tanto para la muestra de tipo azul como de tipo rojo, en función del *redshift*. Estudiamos la evolución de la muestra de galaxias de tipo azul y en tipo rojo para $M^{\star}_{K_s}$ y para $\phi^{\star}_{K_s}$. Observamos que la evolución para el parámetro $M^{\star}_{K_s}$ presenta una evolución de alrededor de una magnitud para las galaxias de tipo azul. Sin embargo, para galaxias rojas, no parece que haya evolución. Atendiendo a estos resultados, podríamos decir que la formación estelar que tuvo lugar en el pasado ha ido desapareciendo de manera progresiva en las galaxias azules. El comportamiento para las galaxias rojas indica que las galaxias más masivas en el universo ya estaban presentes en en tiempos cósmicos tempranos, y que han evolucionado muy poco en el tiempo.

En el caso del parámetro $\phi^{\star}_{K_s}$, observamos que hay un indicio de evolución para galaxias azules, y una evolución más evidente para galaxias de tipo rojo desde el universo temprano hasta el presente. Bajo el paradigma de la formación y evolución de galaxias, estos resultados sugieren que la población de estrellas rojas se ido incrementando, sobretodo a través de los procesos seculares de las galaxias, ya que la cantidad de gas necesaria para la formación de nuevas estrellas se va agotando continuamente.

También hemos incluido los resultados de la densidad de luminosidad en la banda K_s, que se obtiene integrando sobre todas las luminosidades una ver obtenido el modelo de la función de luminosidad. Hemos hallado que la densidad

de la luminosidad para galaxias de tipo azul seleccionadas en la banda K_s, decrece en aproximadamente un factor 2 desde *redshift*=2.5 hasta *redshift*=0.0, mientras que la luminosidad para galaxias rojas se incrementa en un factor 4 en ese mismo rango de *redshift*. Estos resultados reflejan un descenso en la tasa de formación estelar del Universo (obtenido a partir de la muestra de galaxias azules), y revelan el paso de un tipo de galaxias a otro al evolucionar las poblaciones en su interior.

Este trabajo esta listo para ser publicado, y será enviado junto con un análisis más exhaustivo de las implicaciones de los resultados obtenidos para los diferentes escenarios de la evolución de galaxias.